RADAR CROSS SECTION SIMULATIONS OF ARBITRARY SHAPES

by

Oya İstemi

B.S., Electronics and Communication Engineering, Istanbul Technical University, 2004

Submitted to the Institute for Graduate Studies in
Science and Engineering in partial fulfillment of
the requirements for the degree of
Master of Science

Graduate Program in Electrical and Electronics Engineering
Boğaziçi University

2008

ACKNOWLEDGEMENTS

I would like to thank my thesis supervisor, Prof. Dr. Selim Şeker for his guidance and motivation throughout my study.

I would also like to thank the other members of the thesis committee for their constructive help. Especially, I am grateful to Assoc Prof. A. Arif Ergin for his support, help and motivation throughout completing my thesis.

And, I would like to thank my friend Oya Çeliktutan for her help and support throughout my study.

Finally, I would like to thank my family for their support and motivation through my education. I am specially grateful to Burak Çatalyürek for his endless help and support.

ABSTRACT

RADAR CROSS SECTION SIMULATIONS OF ARBITRARY SHAPES

This thesis is about the Radar Cross Section measurements of arbitrary shapes. The progress in radar cross section measurements is strongly related to the progress in Radar technology. Arbitrary shapes, such as aircrafts, vegetation, play important role in the application of Radar technologies. Furthermore, the electromagnetic scattering from dielectric objects has received increasing attention. Different disciplines are interested in different properties of the dielectric objects, and many published papers about this topic are found in literature. Firstly, RCS of simple shapes, such as flat plate, cylinder was measured and compared with the result given in the literature. Measurements were done in İstanbul Technical University in Electromagnetic Diagnostic and Measurement Laboratory for Vertical Polarization. On the other hand, Ansoft HFSS simulation program was used to complete RCS Measurements both simple and arbitrary shapes. RCS of arbitrary shapes that were obtained from hollow cylinder was calculated by using Ansoft HFSS to verify Discretization Solution. Lastly, RCS of complex shapes was computed. To compare with theoretical result, MATLAB programming is used. The good agreement were found for both Horizontal and Vertical polarizations for single layer models.

ÖZET

RASGELE ŞEKİLLERİN RADAR KESİT ALANLARININ SİMULASYONLA ELDE EDİLMESİ

Bu tezde rasgele şekillerin radar kesit alanlarının ölçülmesi üzerine çalışılmıştır. Radar kesit alanlarının hesaplanması ile ilgili ölçümlerdeki gelişim doğrudan Radar teknolojilerindeki ilerleme ile ilişkilidir. Uçak, füze, bitki örtüsü gibi rasgele şekiller Radar teknolojileri ile ilgili uygulamalarda önemli bir yere sahiptir. Ayrıca, son zamanlarda dielektrik malzemelerdeki elektromagnetik saçılma ile ilgili araştırmalar büyük önem taşımaktadır. Farklı bilim dalları, dielektrik malzemelerdeki elektromagnetik saçılmanın farklı özellikleri ile ilgili araştırmalar yapmaktadır. Literatürde bu konu ile ilgili birçok akademik çalışma bulunmaktadır. Başlangıç olarak plaka ve silindir gibi basit şekillerin ölçümleri yapılmış ve sonuçlar diğer akademik çalışmaların sonuçları ile karşılaştırılmıştır. Ölçümler İstanbul Teknik Üniversitesi, Elektromagnetik Tanı ve Öçüm Labaratuarında, dikey polarizasyon için yapılmıştır. Öte yandan, diğer modellerin Radar Kesit Alanı'nı hesaplamak için Ansoft HFSS simulator programı kullanılmıştır. Silindirden elde edilen rasgele şekiller ve bazı kompleks şekillerin Radar Kesit Alanı Ard Arda Ekleme Çözümünü doğrulamak için simulasyon programı ile elde edilmiştir. Teorik sonuçlar ile kıyaslamalar için MATLAB programı kullanılmıştır. Bazı tek tabakali modellerde teorik ve deney sonuçları için uyumlu sonuçlar gözlenmiştir.

TABLE OF CONTENTS

LIST OF FIGURES

LIST OF TABLES

LIST OF SYMBOLS / ABBREVIATIONS

c	The velocity of light
$\hat{e}_i$	A unit vector in the direction of its polarization
E^{inc}	The field incident at the target
E^{scat}	The scattered electric field
G_r	Gain of the receiving antenna in the direction of the target
G_t	Gain of the transmitting antenna in the direction of the target
$\hat{i}$	A unit vector in the direction of wave propagation
k	Wave number
l	The distance from source to scatterer
L_{mt}, L_{mr}	Numerical factors which allow the propagation medium to have loss
L_p	Numerical factor to account for polarization losses
L_t	Numerical factor to account for losses in the transmitting system
R	The distance between the transmitter and the scatterer
r	Range between the target and receiving antenna
r_t	Range between the transmitting antenna and the target
P_t	Transmitter power in Watts
w_1	The distance from the scatterer to a maximum in the total field
w_2	The distance from the scatterer to a null in the total field
λ	A wavelength in the medium
λ_0	Radar wavelength
ρ	The measured voltage standing-wave-ratio
σ	Radar cross section
RCS	Radar Cross Section

1. INTRODUCTION

Technological development in signal processing area caused seriously improvements in radar performances in last decades. Increasing of radar range by developing of sensitivity has been made the builders of aircraft and other military systems to try to reduce the radar cross section (RCS) of equipment. Because of the great significance for aircraft, the radar is the main equipment that is used to discover and to track them [1]. The RCS information is used for numerous purposes, ranging from the design of novel stealth vehicles with reduced radar signatures to the decision of electronic counter measures (ECM) to engage against a certain threat [2].

Radar cross section is a description of how an object reflects an incident electromagnetic wave. For an arbitrary object, the RCS is highly dependent on the radar wavelength and incident direction of the radar wave [3]. The definition of RCS is a measure of power that is scattered in a given direction when a target is illuminated by an incident wave. RCS does not depend on the distance between the target and the illumination source because it is normalized to the power density of the incident wave at the target. This situation provides that the effects of the transmitter power level and distance to target are removed when the illuminating wave's intensity decreases because of inverse square spherical spreading. RCS is also normalized so that inverse square fall-off of scattered intensity due to spherical spreading is not a factor so that it is not necessary to know the position of the receiver. RCS is defined to describe the target properties without the effects of transmitter power, receiver sensitivity, and the position of transmitter or receiver distance [3].

The RCS of target may be seen as a comparison of the strength of the reflected signal from a target to the reflected signal from a perfectly smooth sphere of cross sectional area of $1\,m^2$. RCS of target is visualized as the product of three factors. These factors are projected cross section, reflectivity and directivity [1].

To conduct RCS measurements, there are five reasons that have different influences when the measurements are carried out. These reasons are obtain understanding of basic scattering phenomena, obtain diagnostic data, verify system performance, build database, and satisfy a contractual requirement [3].

The aim of radar cross section measurement range is to collect radar target scattering data. The range user usually-but not always- needs far-field data, corresponding to the case where the target is located far enough from the instrumentation radar that the incident phase fronts are adequately flat. Generally, this necessity can be satisfied only on an outdoor range. On the other hand, lots of research and improvement programs can be conducted indoors in anechoic chambers [3].

RCS measurements which are done whether indoors or outdoors must have some features, such as, an instrumentation radar capable of launching and receiving a microwave signal of sufficient intensity, recording instruments, either analog or digital or both, for saving the information, a controllable target rotator or turntable, a low background signal environment, containing invisible target support structures, in order to minimize contagion of the wanted signals, and a test target appropriate for the measurements [3].

These five fundamental features can be adorned and added by another equipment and instrumentation. The instrumentation that is used indoors can differ from that used for outdoor measurements [3].

In this thesis, Chapter 2 begins with definition of the Radar Cross Section. After that, the fundamental scattering and absorption mechanisms are explained. Finally, objects whose radar cross section is known in literature are determined.

Chapter 3 begins with RCS measurements methods. Firstly, some terms are determined, after that the basis of the various measurement methods are discussed.

Chapter 4 firstly introduces the measurement environment, Electromagnetic Diagnostic and Measurement Laboratory in İstanbul Technical University and measurement system’s architecture and its components are explained. RCS measurements

will be given for conducting rectangular flat plate, conducting cylinder and dielectric cylinder. Secondly, RCS simulations will be obtained by using High Frequency Structure Simulator program for conducting flat plate, cylinder, dielectric disk and cylinder for vertical and horizontal polarizations.

Chapter 5 is about RCS simulations of arbitrary shapes. The results obtained by HFSS will be given for arbitrary shapes that are obtained from single layer and multilayer cylinders to compare with the results of Discretization Solution. The results will be obtained for vertical and horizontal polarizations at high and low frequencies.

In chapter 6, RCS of extended arbitrary shapes will be computed by using HFSS. This study will consider the properties of corn leaves of vegetation. Quarter circle and semi circle surfaces and toroid will be studied at low and high frequencies.

2. RADAR CROSS SECTION OF OBJECTS

2.1 The Definition of Radar Cross Section

When the electromagnetic waves, with any designated polarization, incident on a target, they are normally diffracted or scattered in all directions. These scattered waves are broken into two parts. The first part of waves which have the same polarizations as the receiving antenna (called like polarization); the others will have different polarization which is called cross polarization. The two polarizations are orthogonal and called to as the Principal Polarization (PP) and Orthogonal Polarization (OP), respectively. The intensity of the backscattered energy that has the same polarization as the radar's receiving antenna is used to determine the target Radar Cross Section. When a target is illuminated by RF energy, it behaves like an antenna, and will have near and far fields. In general, waves reflected and measured in the near field are spherical. Alternatively, in the far field the wavefronts are scattered into a linear combination of plane waves [4].

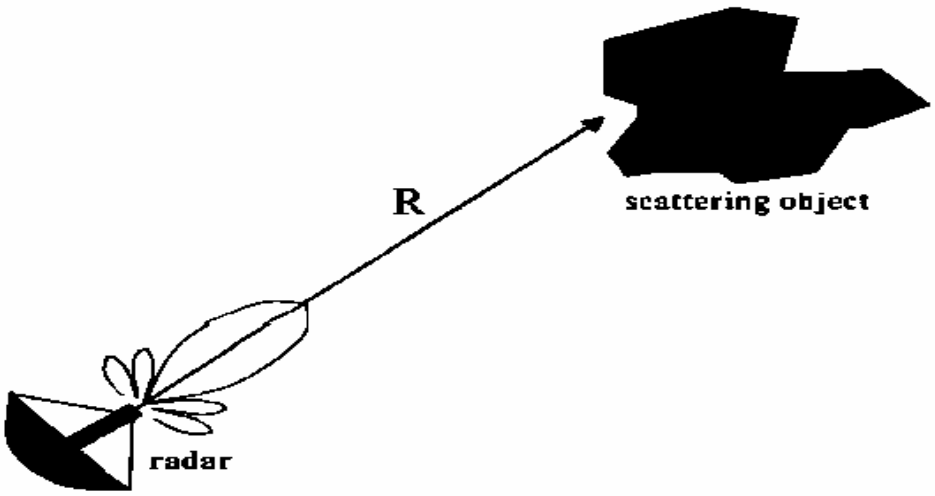

Figure 2.1. Scattering object located at range R

Assume that the radar is located a finite distance R from the target, as illustrated in Figure 2.1. The intrinsic impedance, Z_0, and the intrinsic admittance of the medium, Y_0, can be defined as;

$$Z_0 = \frac{E^{inc}}{H^{inc}} \text{ (ohm)} \ , \ Y_0 = \frac{H^{inc}}{E^{inc}} \text{ (mho)} \tag{2.1}$$

where E ad H are the strengths of the electric and magnetic fields, Z_0 is intrinsic impedance and Y_0 is the admittance of free space [5].

Power density P_{di} can be calculated as

$$P_{di} = \frac{E^{inc}.H^{inc}}{2} \tag{2.2}$$

The power density of spherical wave at the target can be determined by using the (2.1) and (2.2) as [5],

$$P_{di} = \frac{\left|E^{inc}\right|^2.Y_0}{2} \tag{2.3}$$

In order to calculate the power "captured" by the target, the power density is multiplied by the target's fictitious area, σ,

$$P = \sigma.P_{di} = \frac{\sigma.\left|E^{inc}\right|^2.Y_0}{2} \tag{2.4}$$

The symbol σ denotes the Radar Cross Section. If the target radiates this captured power isotropically without loss, at a distance R from the target, the power density P_{ds} of spherical wave will be;

$$P_{ds} = \frac{P}{4\pi R^2} = \frac{\sigma Y_0 \left|E^{inc}\right|^2}{8\pi R^2} \tag{2.5}$$

This power density can be expressed in terms of *scattered field* strength E^{scat} :

$$P_{ds} = \frac{\left|E^{scat}\right|^2 Y_0}{2} \tag{2.6}$$

If (2.5) and (2.6) are solved, σ can be found as,

$$\sigma = 4\pi R^2 \frac{|E^{scat}|^2}{|E^{inc}|^2}. \tag{2.7}$$

In order to ensure that the radar receiving antenna is in the far field, so scattered waves received by the antenna is planar, equation (2.7) is modified as;

$$\sigma = \lim_{R\to\infty} 4\pi R^2 \frac{|E^{scat}|^2}{|E^{inc}|^2} \tag{2.8}$$

Equation (2.8) is the formal definition of Radar Cross Section [5].

Even though, there are no known two-dimensional objects in the physical world, the scattering by such bodies is often analytically tractable when the scattering by truncated, three-dimensional versions of them is not. In the two-dimensional case the scattering cross section becomes a scattering width, in units of length, not area. The reduction to two dimensions from three results in a slightly different from for the radar cross section, this time per unit length [5]:

$$\sigma_{2D} = \lim_{\rho\to\infty} 2\pi\rho \frac{\left|E^{scat}\right|^2}{\left|E^{inc}\right|^2} \tag{2.9}$$

where ρ is the distance from the axis of the structure to the observation point.

The unit of RCS most commonly used is decibels relative to a square meter (dBsm) [6]:

$$\sigma, dBsm = 10\log(\sigma, m^2) \tag{2.10}$$

Typical values of RCS ranging from 40 dBsm ($10{,}000\,m^2$) for ships and large bombers to -30 dBsm ($0.001\,m^2$) for insects are indicated in Figure 2.2 [6].

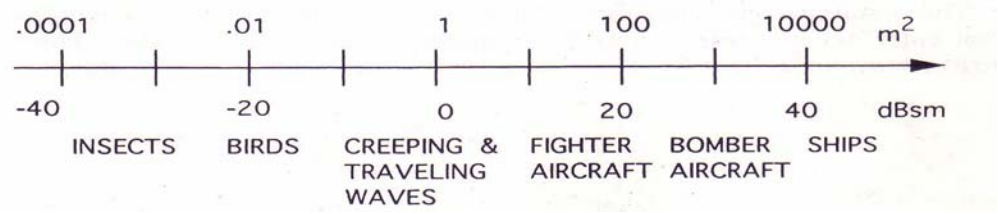

Figure 2.2. Typical values of RCS

Modern radars can detect the flocks of birds and even swarms of insects. The radar's computer will search all directions and can discard these targets on the basis of their velocity and trajectory. However, the fact that such low RCS targets are detectable implies that the RCS design engineering is a difficult job [6].

RCS is dependent on many factors such as, frequency, polarization of the incident wave and the target aspect. These factors should be taken into consideration when radar is designed to detect a specific target [6].

In [7], the received power at a radar, P_r, is determined by using the function of these parameters. It is beneficial to attempt to divide these parameters so that P_r may be explained as a function of the transmitter system, the propagation path from the transmitter system to the target, the propagation path from the target to the receiving system, and the receiving system. The functional relationship between these parameters and the received power can be summarized;

$$P_r = \underbrace{\frac{P_t.G_t}{L_t}}_{\text{Transmitting System}} \underbrace{\frac{1}{4\pi r_t^2 L_{mt}}}_{\text{Propagation medium}} \underbrace{\sigma}_{\text{Target}} \underbrace{\frac{1}{4\pi r^2 L_{mr}}}_{\text{Propagation medium}} \underbrace{\frac{G_T\,\lambda_0^2}{4\pi L_r}}_{\text{Receiving system}} \underbrace{\frac{1}{L_p}}_{\text{Polarization effects}} \qquad (2.11)$$

Polarization losses happen since the transmitting and receiving antennas are not properly polarized, because the propagation medium alters the original polarization, or because the target depolarizes the signal [7].

By analyzing the dimensions of the various terms in Equation (2.11) to equate radar cross section, σ, to the other parameters;

$$\sigma = \frac{P_r L_r (4\pi)}{G_r \lambda_0^2} \frac{L_t}{P_t G_t} L_{mr} L_{mt} (4\pi) r_t^2 r^2 L_p \tag{2.12}$$

It is known that if radar of very large power sounds the ionosphere, the ionospheric parameters will alter. Thus, the reflectivity will change. This effect is known as the Luxembourg effect. However, the constitutive effects for the radar targets are considered to be independent of the signal strength. Parameters of the receiver-transmitter system that effect the observed radar cross section are the radar or carrier frequency, the transmitted waveform, the character of the wavefront of the incident field if the target is near to the transmitting system, and the polarization of the radar signal. In spite of these parameters, the cross section is still a function of only the target body, because any wavefront can be decomposed into a linear combination of plane waves. Any waveform can be similarly decomposed into its frequency components, and the cross section is unique for a particular frequency and polarization. Therefore, the cross section may be defined by superposition from a linear combination of frequencies, polarizations, and plane wave responses [7].

If we look at the IEEE RCS definition, IEEE dictionary of electrical and electronic terms determines RCS as a measure of reflective strength of a target described as 4π times the proportion of the power per unit solid angle scattered in a specific direction to the power per unit area in a plane wave incident on the scatterer from a specified direction. More precisely, it is the limit of that proportion as the distance from the scatterer to the point where the scattered power is measured approaches infinity; this definition is formulated in (2.8) [4].

Calculation of RCS is actually a matter of finding the scattered electric field from a target. If the current, which is induced on the target by the incident plane wave, can be

defined, the same radiation integrals used in antenna analysis can be performed to calculate the scattered field. In the far zone of the target, the scattered field dependence on range will approach $1/R$. Consequently, σ will be range independent. However, defining the induced current is a difficult problem because Maxwell's equations have to be solved for complicated boundary conditions. In many cases, only a numerical solution is possible [6].

2.2 Basic Scattering Theory

When a wave illuminates a single particle, a portion of the incident power is scattered out and another portion is absorbed by the particle. The characteristic of these two phenomena, scattering and absorption, can be explained most conveniently by assuming an incident plane wave [8].

When we consider a linearly polarized electromagnetic plane wave propagating in a medium with dielectric constant ε_0 and permeability μ_0, with the electric field that is given by

$$\vec{E}_i(\vec{r}) = \hat{e}_i \exp(ik\hat{i}.\vec{r}) \tag{2.13}$$

The amplitude $|\vec{E}_i|$ is selected to be one (volt/meter), $k = \omega\sqrt{\mu_0\,\varepsilon_0} = 2\pi/\lambda$ is the wave number, λ is the wavelength in the medium, $\hat{i}$ is a unit vector in the direction of wave propagation, and $\hat{e}_i$ is a unit vector in the direction of its polarization [8].

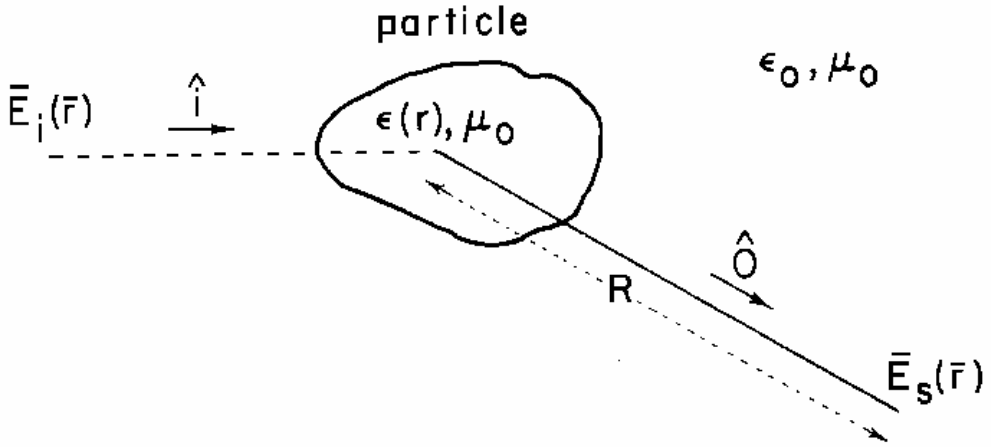

Figure 2.3. A plane wave $\vec{E}_i(\vec{r})$ is incident upon a dielectric scatterer and the scattered field $\vec{E}_s(\vec{r})$ is observed in the direction $\hat{0}$ at a distance R.

The wave is incident upon a particle, illustrated in Figure 2.3, whose relative dielectric constant is explained by

$$\varepsilon_r(\vec{r}) = \frac{\varepsilon(\vec{r})}{\varepsilon_0} = \varepsilon_r'(\vec{r}) + i\varepsilon_r''(\vec{r}) \tag{2.14}$$

$\varepsilon_r(\vec{r})$ is in general complex and a function of position, as the particle may be lossy and inhomogeneous. The field at a distance R from a reference point in the particle, in the direction of a unit vector $\hat{0}$ consists of the incident field E_i and the field E_s scattered by the particle. Within a distance $R < D^2/\lambda$, where D is a typical dimension of the particle such as its diameter, the field E_s has complicated amplitude and phase variations due to interference between contributions from different portions of the particle and the observation point r is said to be in the *near field* of the particle. When $R > D^2/\lambda$, however, the scattered field E_s acts like a spherical wave and is given by

$$\vec{E}_s(\vec{r}) = \vec{f}(\hat{0},\hat{i})(e^{ikR}/R) \qquad \text{for } R > D^2/\lambda \tag{2.15}$$

$\vec{f}(\hat{0},\hat{i})$ denotes the amplitude, phase, and polarization of the scattered wave in the *far field* in the direction $\hat{0}$ when particle is illuminated by a plane wave that propagates in the direction $\hat{i}$ with unit amplitude, and is named the scattering amplitude. It should be pointed out that though the incident wave is linearly polarized, the scattered wave is in general elliptically polarized.

Suppose the scattered power flux density S_s at a distance R from the particle in the direction $\hat{0}$, caused by an incident power flux density S_i. The differential scattering cross section is determined,

$$\sigma_d(\hat{0},\hat{i}) = \lim_{R\to\infty}\left[(R^2 S_s)/S_i\right] = \left|f(\hat{0},\hat{i})\right|^2 = (\sigma_t/4\pi)p(\hat{0},\hat{i}) \tag{2.16}$$

The magnitudes of the incident, S_i, and the scattering power flux density, S_s, vectors can be defined as follow;

$$\vec{S}_i = \frac{1}{2}\left(\vec{E}_i \times \vec{H}_i^*\right) = \frac{|E_i|^2}{2\eta_0}\hat{i}\,, \qquad \vec{S}_s = \frac{1}{2}\left(\vec{E}_s \times H_s^*\right) = \frac{|E_s|^2}{2\eta_0}\hat{0} \tag{2.17}$$

and, $\eta_0 = \left(\mu_0/\varepsilon_0\right)^{1/2}$ the characteristic impedance of the medium.

In radar applications, the bistatic radar cross section σ_{bi} and the backscattering cross section σ_b are often used. They are connected to σ_d through

$$\sigma_{bi}(\hat{0},\hat{i}) = 4\pi\sigma_d(\hat{0},\hat{i})\,, \qquad \sigma_b = 4\pi\sigma_d(-\hat{i},\hat{i}) \tag{2.18}$$

σ_b is also named the radar cross section.

Mathematical definitions of scattering amplitude and cross sections can be made in one of two ways. If the shape of particle is a simple, such as a sphere or an infinite

cylinder, it is probable to get whole expressions for cross sections and scattering amplitude. However, the shape of a particle is not simple in many practical situations. So, a method of determining approximate cross sections for particles with complex shapes is needed. It can be obtained through general integral representations of scattering amplitude. Furthermore, the method is beneficial for particles with simple shapes since the calculations can be made easily [8].

It is also noted that in the far-field,

$$\nabla(e^{ikR}/R) \cong (e^{ikR}/R)(ik\nabla R) = (ik\hat{0})(e^{ikR})(e^{ikR}/R) \tag{2.19}$$

and, consequently, ∇ is equivalent to $ik\hat{0}$. Scattering field is obtained as

$$E_s(r) = f(\hat{o},\hat{i})\frac{e^{ikR}}{R} \tag{2.20}$$

where

$$f(\hat{o},\hat{i}) = \frac{{k_0}^2(\varepsilon_r - 1)}{4\pi}\int (I - oo)\cdot E_{\text{int}}(x,q)\cdot e^{-ik_0 ox}dx, \qquad q \in \{h,v\} \tag{2.21}$$

Equation (2.20) is the accurate expression for the scattering amplitude $f(\hat{o},\hat{i})$ in terms of the total electric field $E(r')$ inside the particle. This field $E(r')$ is not known in general, so (2.20) is not full description of the scattering amplitude in terms of known quantities. For many practical situations, nevertheless, it is possible to approach $E(r')$ by some known function and it is obtained a useful approximate expression for $f(\hat{o},\hat{i})$.

Radar Cross Section in terms of complex $f(\hat{o},\hat{i})$ is;

$$\sigma = 4\pi\left|f(\hat{o},\hat{i})\right|^2 = 4\pi\left[f(\hat{o},\hat{i})\,conj(f(\hat{o},\hat{i}))\right] \tag{2.22}$$

2.3 Scattering Mechanisms

The RCS of objects that is encountered by most radar is more complex than spheres or plates. There are a few exceptional examples such as weather balloons and buoys. However, simple shapes such as plates, spheres, cylinders and wires are useful in studying the phenomenology of RCS. Moreover, complex objects can be decomposed into primitives. Figure 2.4 shows an aircraft that can be decomposed into cylinders, plates, cones and hemispheres. A collection of basic shapes will give an acceptable RCS estimation, which can be used during the initial design stages of a platform. The positions and levels of the largest RCS lobes are of most concern at this stage of the design process. The accuracy of the RCS calculation at other angles will be dependent on how the interactions between the various shapes are handled. These interactions are more difficult to contain, even when they are included, the agreement with measured RCS is not especially good. For a low-observable object, more sophisticated numerical techniques must be used [6].

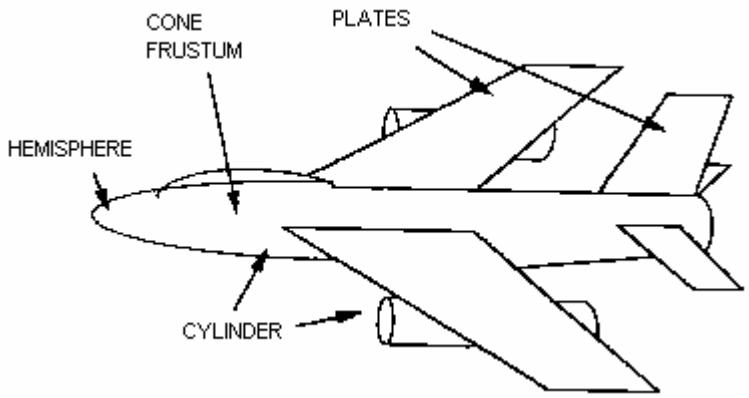

Figure 2.4. Aircraft represented by geometrical components

Many scattering mechanisms are commonly encountered. Their level relative to the peak RCS can be quite small but away from the peaks, scattering because of these mechanisms can dominate. They are illustrated in Figure 2.5 and are shortly determined as follows [6].

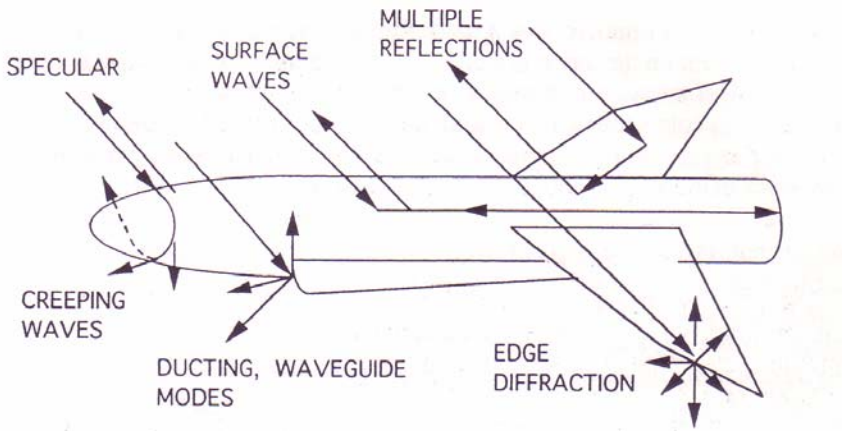

Figure 2.5. Illustration of scattering mechanism

Reflections: This mechanism gives the highest RCS peaks, but these peaks are limited in number since Snell's law must be satisfied. When multiple surfaces are present, multiple reflections can take place. For example, the incident plane wave could probably reflect off the fuselage, hit a fin, and then come back to the radar [6].

Diffractions: All of Diffracted fields are scattered from discontinuities such as edges and tips. The waves that are diffracted from these shapes are less intense than reflected waves, but they can emerge over a wide range of angles. In regions of low RCS, diffracted waves can be significant [6].

Surface Waves: The term surface wave refers to the current traveling along a body and contains many types of waves. Generally, the target behaves as a transmission line, leading the wave along its surface. If the surface is smooth closed shape such as a sphere, the wave will circulate around the body many times. On curved bodies, the surface wave will continuously radiate. These are named creeping waves since they appear to creep around the back of a curved body. Radiating surface waves on flat bodies are generally named leaky waves. Traveling waves appear on slender bodies and along edges and suffer little attenuation as they propagate. If the surface is terminated with a discontinuity such as an edge, the traveling wave will be reflected back toward its origin. It will be seen that traveling wave RCS lobes can reach surprisingly large levels [6].

Ducting: Ducting is also named waveguide mode; it takes place when a wave is trapped in a partially closed structure. An air inlet cavity on a jet can be given as example. Once the

wave enters the cavity, many bounces can take place before a ray emerges. The ray can take many paths, and therefore, rays will emerge at most all angles. The result is a large, broad RCS lobe. An optical analogy of this is the glowing of a cat's eye when illuminated by a light [6].

These mechanisms occasionally interact with each other. For instance, a wave reflected from a flat surface can subsequently be diffracted from an edge or enter a cavity. For a complex target, the interactions are not always obvious [6].

2.4 Frequency Regions

The scattering characteristics of a target strongly depend on the frequency of the incident wave. There are three frequency regions in which the RCS of a target is distinctly different. These frequencies are 1) low-frequency, 2) resonance, 3) high-frequency regimes. If the target is smooth which is illustrated in Figure 2.6, and its length is L, the three frequency regimes can be determined depending on the ratio of wavelength λ to body size L, λ/L or inversely, kL. These regions can be defined as follows [6].

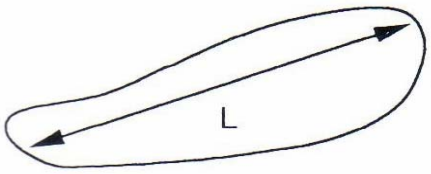

Figure 2.6. Arbitrary body with a characteristic length L

Low-frequency region ($kL <<< 1$, $\lambda >>> L$): At these frequencies, the phase variation of the incident plane wave across the extent of the target is small. Consequently, the induced current on the body is nearly constant in amplitude and phase. The particular shape of the body is not important. For instance, both small sphere and small cube pose essentially isotropic scattering patterns. Generally, λ vs kL is smooth and varies as $1/\lambda^4$. This region is also named as *Rayleigh Region* [6].

Resonance region ($kL \approx 1$, $\lambda \approx L$): For these frequencies, the phase variation the current across the body is significant, and all parts contribute to the scattering pattern; λ vs kL will oscillate. This region is also called the *Mie Region* [6].

High-frequency Region ($kL >>> 1, \lambda <<< L$): There are many cycles in the phase variation of the current across the body and eventually, the scattered field will be very angle dependent. The peak scattering levels are due primarily to isolated points. For instance, the peak scattering from large flat plates originates from specular points on the surface. In this region, λ vs kL is smooth and may be independent of λ. This is also referred as *Optic region* [6].

The RCS of sphere over these three regions is illustrated in Figure 2.7. For $ka < 0.5$, where a is radius, the curve is almost linear but above 0.5, it begins to oscillate. This region is resonance region. The oscillations die out at higher values and above $ka = 10$, the curve is accurately a constant equal to πa^2 [6].

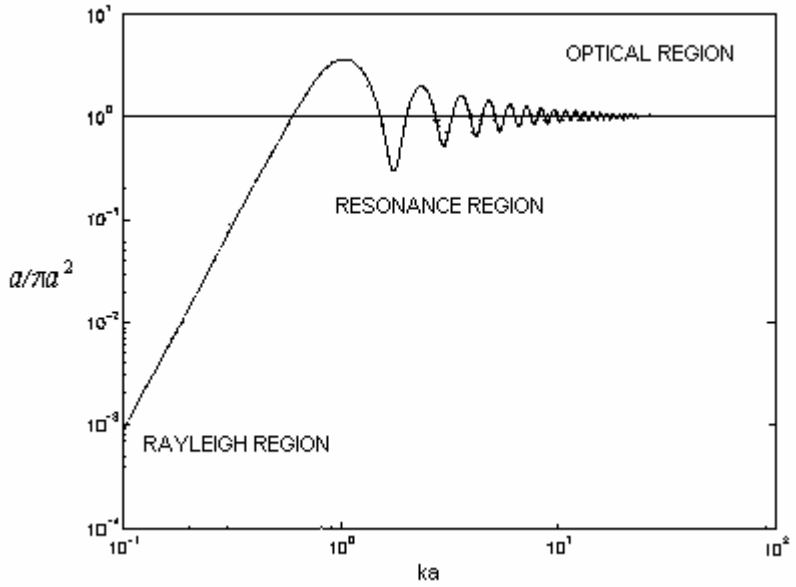

Figure 2.7. Radar cross section of a sphere

The scattering characteristics of the target are only one of several considerations that enter into the selection of the operating frequency of radar. Others are size constraints,

antenna gain, beamwidth, transmitter power, ambient noise, Doppler shift and atmospheric attenuation.

The frequency spectrum is divided into bands as shown in Table 2.1.

Table 2.1. Radar frequency band [6]

Band Designation	Frequency Range
HF	3-30 MHz
VHF	30-300 MHz
UHF	300-1000 MHz
L	1-2 Ghz
S	2-4 GHz
C	4-8 GHz
X	8-12 GHz
Ku	12-18 GHz
K	18-27 GHz
Ka	27-40 GHz
MM	40-300 GHz

2.5 Determination of Radar Cross Section

For simple target objects, such as flat plates, sphere, cylinder, RCS can be computed using Maxwell's equations with certain boundary conditions [9]. In literature, there are many published papers about the RCS calculation, in this section, these papers will be used to determine the RCS of both conducting or dielectric flat plate and cylinder.

2.5.1 RCS of Conducting Rectangular Flat Plate

Ross computed RCS by using the geometrical diffraction theory. The utility of the application of the geometrical theory to the present problem is defined by comparison with calculations using physical optics and with results of cross section measurements [10].

Keller introduced an extension of geometric optics that accounts for diffraction. It is called the geometrical theory of diffraction. An important advantage of the using this theory is its ability to account for polarizations. The accuracy of the calculated cross section increases as the wavelength becomes much smaller than the targets, but it is often quite accurate for wavelengths comparable to target size [10].

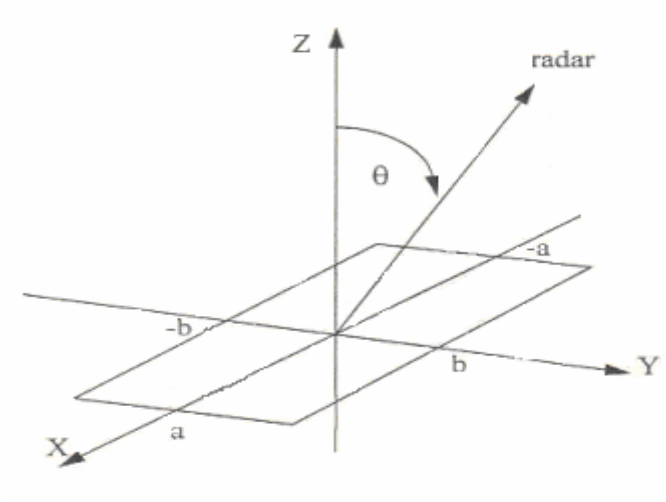

Figure 2.8. Rectangular flat plate

Consider a perfectly conducting rectangular flat plate in the x-y plane as illustrated in Figure 2.8. The two sides of the plate are denoted by 2a and 2b and the plate is assumed to be thin compared to wavelength [10].

Geometrical diffraction theory ensures localization of the scattering at points determined by stationary phase arguments or by abrupt geometric discontinuities. It assumes that the current distribution in the neighborhood of a scattering center is obtainable from that of a known case of similar local geometry. A coefficient of diffraction is assigned to each center based on the similar and weighted by a phasor proportional to the distance along a ray drawn from the radar to the scattering center [10].

Ross's results for scattering from the edge of an infinite half plane are given as;

$$\sigma_{total_V} = +\frac{Ae^{ikr+i(\pi/4)}}{2\sqrt{2}(kr)^{1/2}}\left\{\left[1+\frac{1}{\sin\theta}\right]e^{-i2ka\sin\theta}+\left[1-\frac{1}{\sin\theta}\right]e^{+i2ka\sin\theta}\right\}$$
$$+\left\{\frac{Ae^{ik(r+2a)}}{2\pi(kr)^{1/2}(2ka)^{3/2}\cos\theta}\right.$$
$$\left.+\frac{Ae^{ik(r+4a)-(\pi/4)}}{8\pi\sqrt{2\pi}(kr)^{1/2}(2ka)^3}\left[\frac{(1+\sin\theta)}{(1-\sin\theta)^2}e^{-i2ka\sin\theta}+\frac{(1-\sin\theta)}{(1+\sin\theta)^2}e^{i2ka\sin\theta}\right]\right\} \qquad (2.23)$$
$$\times\left\{\frac{1}{1-\frac{e^{i4ka-i(\pi/2)}}{8\pi(2ka)^3}}\right\}$$

$$\sigma_{total_H} = -\frac{Ae^{ikr+i(\pi/4)}}{2\sqrt{2}(kr)^{1/2}}\left\{\left[1-\frac{1}{\sin\theta}\right]e^{-i2ka\sin\theta}+\left[1+\frac{1}{\sin\theta}\right]e^{+i2ka\sin\theta}\right\}$$
$$-\left\{\frac{2Ae^{ik(r+2a)+i(\pi/4)}}{\pi(kr)^{1/2}(2ka)^{1/2}\cos\theta}-\frac{2Ae^{ik(r+4a)-(3\pi/4)}}{2\pi\sqrt{2\pi}(kr)^{1/2}(2ka)}\left[\frac{e^{-i2ka\sin\theta}}{1-\sin\theta}+\frac{e^{i2ka\sin\theta}}{1+\sin\theta}\right]\right\} \qquad (2.24)$$
$$\times\left\{\frac{1}{1-\frac{e^{i4ka+i(\pi/2)}}{2\pi(2ka)}}\right\}$$

The statement was applied to both edges of a perfectly conducting infinitely thin, infinite strip of width $2a$ and height $2b \to \infty$ [10].

A represents the amplitude of the incident field and r denotes distance from the center of the strip to the radar. The radar cross section per unit length is determined to be

$$\sigma = \lim_{r\to\infty} 2\pi r\left|\frac{E_s}{E_i}\right|^2 \equiv \lim_{r\to\infty} 2\pi r\left|\frac{\sigma_{total}}{A}\right|^2 \qquad (2.25)$$

By introducing the formula that is related to area and length cross sections,

$$\sigma(area)=\frac{8b^2}{\lambda^2}\sigma(length) \tag{2.26}$$

For linearly polarized incident wave in the x-z plane, the horizontal and vertical backscattered RCS of flat plates based upon the geometrical diffraction theory become:

$$\begin{aligned}\sigma_V &= \frac{4b^2}{\pi}\left|\left[\cos 2ka\sin\theta-\frac{i\sin 2ka\sin\theta}{\sin\theta}\right]-\frac{e^{i2ka-i(\pi/4)}}{\sqrt{2\pi}(2ka)^{3/2}}\right.\\ &\times\left[\frac{1}{\cos\theta}+\frac{e^{i2ka-i(\pi/4)}}{4\sqrt{2\pi}(2ka)^{3/2}}\left(\frac{(1+\sin\theta)e^{-i2ka\sin\theta}}{(1-\sin\theta)^2}+\frac{(1-\sin\theta)e^{+i2ka\sin\theta}}{(1+\sin\theta)^2}\right)\right]\\ &\left.\times\left[1-\frac{e^{i4ka-i(\pi/2)}}{8\pi(2ka)^3}\right]^{-1}\right|^2\end{aligned} \tag{2.27}$$

$$\begin{aligned}\sigma_H &= \frac{4b^2}{\pi}\left|\left[\cos 2ka\sin\theta+\frac{i\sin 2ka\sin\theta}{\sin\theta}\right]-\frac{4e^{i2ka+i(\pi/4)}}{\sqrt{2\pi}(2ka)^{1/2}}\right.\\ &\left.\times\left[\frac{1}{\cos\theta}-\frac{e^{i2ka+i(\pi/4)}}{2\sqrt{2\pi}(2ka)^{1/2}}\left(\frac{e^{-i2kas\sin\theta}}{1-\sin\theta}+\frac{e^{+i2ka\sin\theta}}{1+\sin\theta}\right)\right]\times\left[1-\frac{e^{i4ka+i(\pi/2)}}{2\pi(2ka)}\right]^{-1}\right|^2\end{aligned} \tag{2.28}$$

The terms included in the first brackets of (2.27) and (2.28) represent the contribution because of single diffraction at vertical edges of the plate combined with a geometrical optics term. The imaginary component in the first bracket has $\sin x/x$ dependence that suggests the physical optics formula. The second bracket in each of the two formulas is composed of terms arising from double and triple diffraction at vertical edges of the plate. There are an infinite number of diffraction terms involved and their presence is accounted for by the term multiplying the second bracket that is raised to the minus one power. It is seen that for double diffraction, the first term in the second bracket becomes infinite at grazing incidence ($\theta=90^\circ$). In similar way, the component of triple diffraction that originates from near edge of the plate also goes to infinite at grazing incidence. Even though, infinite cross sections are physically impossible, (2.27) and (2.28) are used to

compute flat plate cross sections for comparison with measured data at angles for which finite results are obtained [10].

Ross illustrated that the utility of the application of the geometrical theory to the utility of the application of the geometrical theory to the present problem is defined by comparison with calculations using physical optics and with the results of cross sections measurements.

Physical optics proves to be accurate when plate aspect angles are limited to the region near normal incidence. Since, physical optics fails to account for polarization, little agreement between theory and measurement is observed at larger rotation angles [10].

The Figure given in [10] represents that geometrical diffraction theory shows the good agreement between the analytical and measured data out to about 80 degrees rotation of the square flat plate. For $\phi > 80^{\circ}$ degrees, certain singularities in the analytical expressions dominate. At $\phi = 90^{\circ}$, the cross sections that were calculated on the basis of geometrical diffraction theory are infinite [10].

By using the equations (2.27) and (2.28), the theoretic vertical and horizontal RCS of rectangular thin flat plate whose dimensions are 10.16x10.16 cm are shown in Figure 2.9 and 2.10, respectively. These results are obtained at 9 GHz and they are similar with the results given in [10].

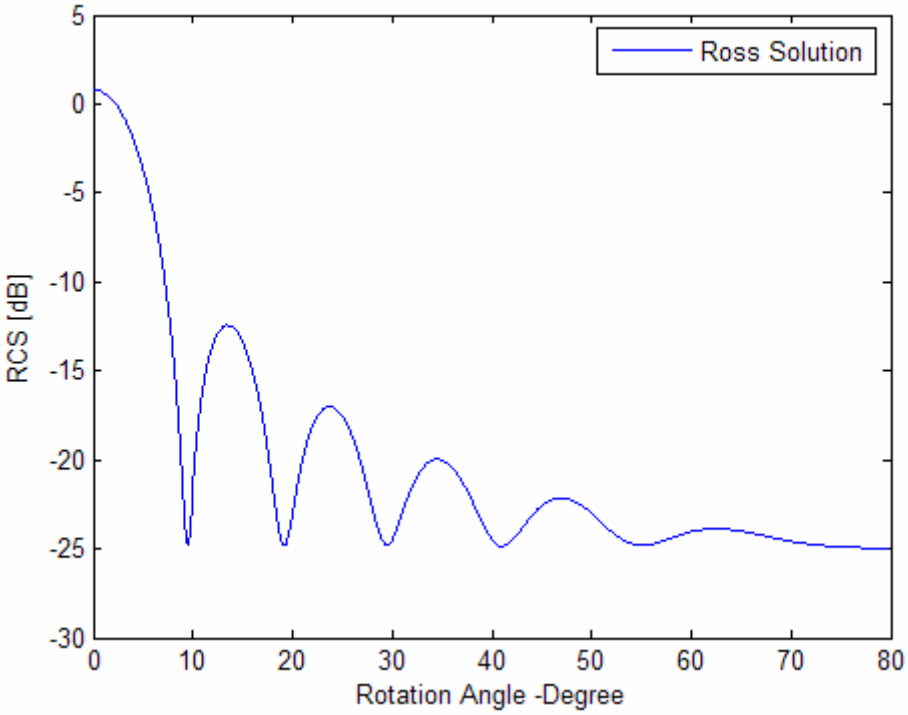

Figure 2.9. RCS of rectangular thin flat plate for vertical polarization

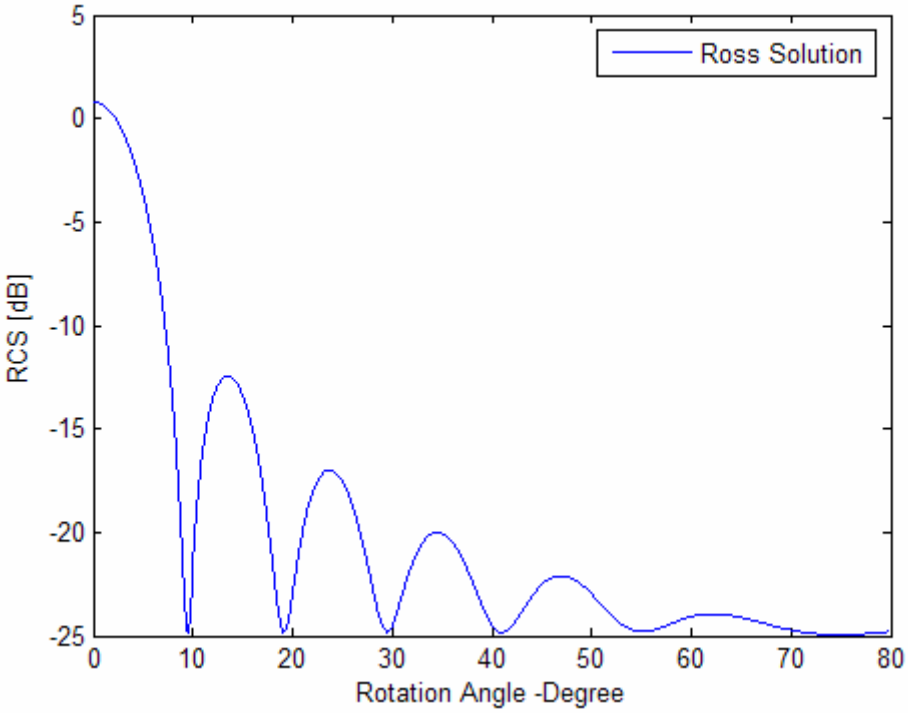

Figure 2.10. RCS of rectangular thin flat plate for horizontal polarization

2.5.2 RCS of Conducting Cylinder

Cylinders present one of the most important classes of geometrical surfaces. The surface of many practical scatterers, such as the fuselage of airplanes, missiles, can often be presented by cylindrical structures. The circular cylinder, due to the its simplicity and its solution is represented in terms of well known and tabulated functions, such as Bessel and Hankel functions, is probably one of the geometries most widely used to present practical scatterers. It is considered in [9], scattering of both plane and cylindrical waves by circular conducting cylinders of infinite length at normal and oblique incidences. The solutions will be obtained using modal techniques [9].

One of the most important parameters in scattering is the scattering width that is obtained by knowing the scattered field in the far zone. The proportion of the far-zone scattered electric field to the incident field for TM mode can be written as [11];

$$\frac{\left|E_z^s\right|}{\left|E_z^i\right|} \overset{\beta_\rho \to l \arg e}{\approx} \frac{\left| -E_0 \sqrt{\frac{2j}{\pi\beta}} \frac{e^{-j\beta\rho}}{\sqrt{\rho}} \sum_{n=-\infty}^{\infty} \frac{J_n(\beta a)}{H_n^{(2)}(\beta a)} e^{jn\phi} \right|}{\left|E_0\, e^{-j\beta x}\right|} = \sqrt{\frac{2}{\pi\beta\rho}} \left| \sum_{n=-\infty}^{\infty} \frac{J_n(\beta a)}{H_n^{(2)}(\beta a)} e^{jn\phi} \right| \tag{2.29}$$

The scattering width can be expressed by using the (2.9),

$$\sigma_{2D} = \frac{4}{\beta} \left| \sum_{n=-\infty}^{\infty} \varepsilon_n \frac{J_n(\beta a)}{H_n^{(2)}(\beta a)} e^{jn\phi} \right|^2 = \frac{2\lambda}{\pi} \left| \sum_{n=-\infty}^{\infty} \frac{J_n(\beta a)}{H_n^{(2)}(\beta a)} \cos(n\phi) \right|^2 \tag{2.30}$$

where

$$\varepsilon_n = \begin{cases} 1 & n = 0 \\ 2 & n \neq 0 \end{cases} \tag{2.31}$$

Plot of the bistatic σ_{2D} / λ that are computed using (2.30) is shown in Figure 2.12 for the cylinder radii, $a = 6\ cm$. This result is same as the result that was given in [11].

For small radii ($a << \lambda$) the first term (n = 0) in (2.29) is the dominant term, and it is sufficient to present the scattered field. Thus for small radii the proportion of the Bessel to the Hankel function for n = 0 can be approximated by;

$$\frac{J_0(\beta a)}{H_0^{(2)}(\beta a)} \cong \frac{1}{-j\frac{2}{\pi}\ln(0.89\beta a)} = j\frac{\pi}{2}\frac{1}{\ln(0.89\beta a)} \tag{2.32}$$

and (2.30) can be reduced to

$$\sigma_{2D} = \frac{2\lambda}{\pi}\left(\frac{\pi^2}{4}\right)\left|\frac{1}{\ln(0.89\beta a)}\right|^2 \qquad for\ a << \lambda \tag{2.33}$$

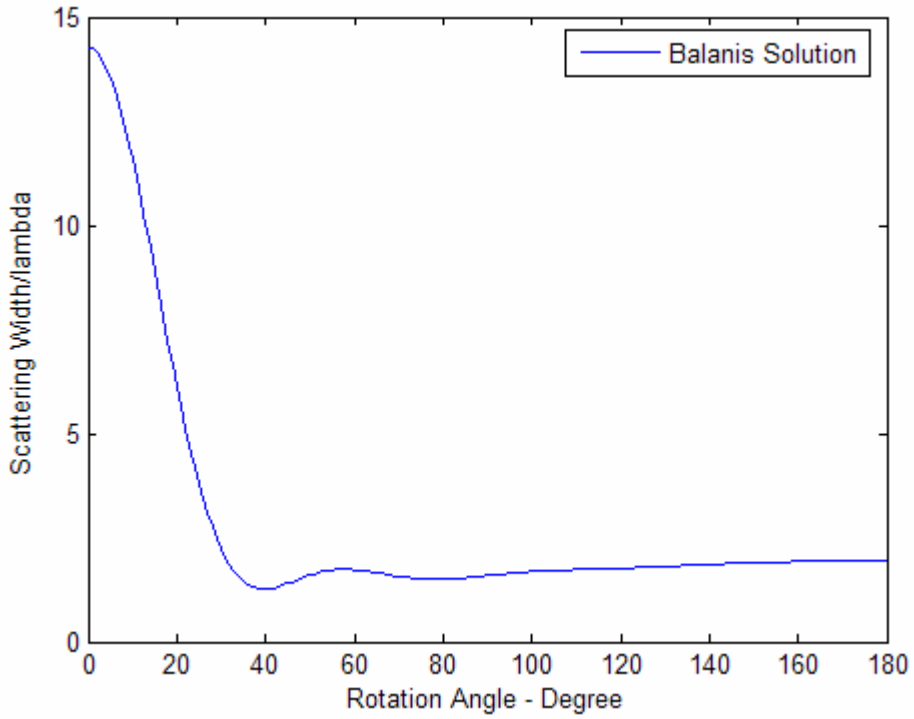

Figure 2.11. Two-dimensional bistatic scattering width of a circular conducting cylinder for vertical polarization

For a cylinder of finite length l the three-dimensional radar cross section for normal incidence is related to two-dimensional scattering width. Thus using the (2.29) and (2.33), three-dimensional RCS can be expressed as [11];

$$\sigma_{3D} = \frac{4l^2}{\pi} \left| \sum_{n=-\infty}^{\infty} \frac{J_n(\beta a)}{H_n^{(2)}(\beta a)} e^{jn\phi} \right|^2 \tag{2.34}$$

$$\sigma_{3D} = \pi l^2 \left| \frac{1}{\ln(0.89\,\beta a)} \right|^2 \quad for \quad (a << \lambda) \tag{2.35}$$

Similarly, the scattering width can be expressed for TE mode as follows [11];

$$\sigma_{2D} = \frac{2\lambda}{\pi} \left| \sum_{n=-\infty}^{\infty} \varepsilon_n \frac{J_n'(\beta a)}{H_n^{(2)\prime}(\beta a)} \cos(n\phi) \right|^2 \tag{2.36}$$

where

$$\varepsilon_n = \begin{cases} 1 & n = 0 \\ 2 & n \neq 0 \end{cases} \tag{2.37}$$

Two dimensional TE bistatic scattering (SW) of a circular conducting cylinder is illustrated in Figure 2.12. This result is compatible with the result that was given in [11].

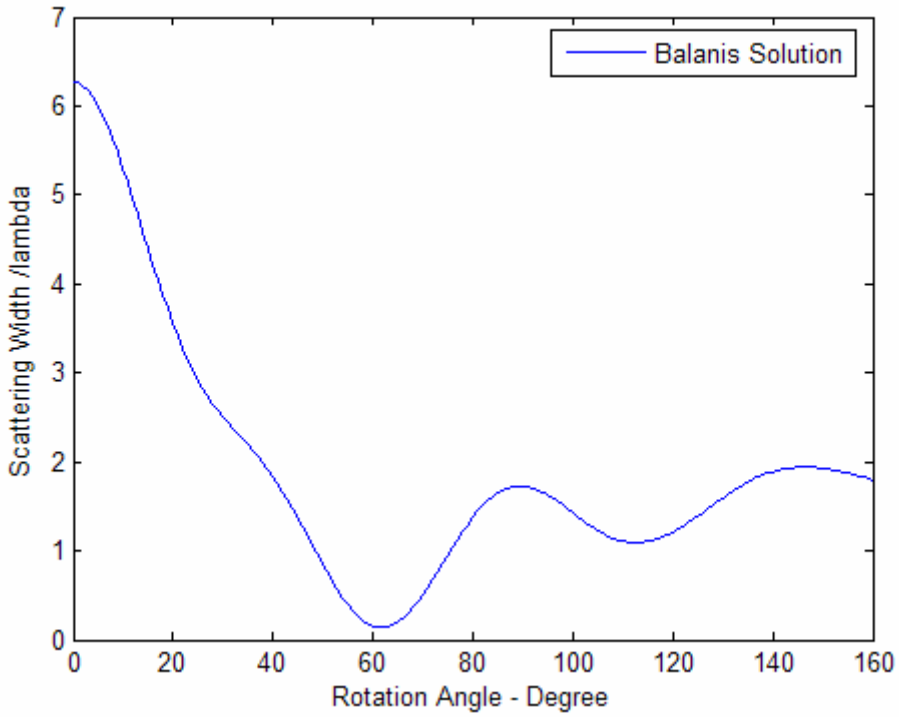

Figure 2.12. Two-dimensional bistatic scattering width of a circular conducting cylinder for horizontal polarization

2.5.3 RCS of Dielectric Rectangular Disk

Dielectric disks are important as models for objects encountered in nature such as the leaves of vegetation and ice crystals formed in clouds at high altitude. Unlike the case of perfectly conducting disk, an exact solution for scattering from dielectric disk has not yet been found [12].

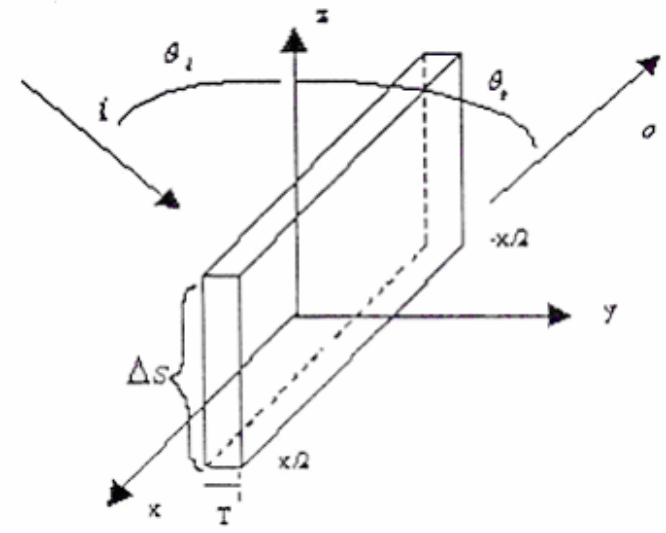

Figure 2.13. EM scattering from a dielectric disk

Sarabandi modeled a leaf as a multilayered planar object in [13]. His model provides an important path for modeling plane multilayered objects. The electromagnetic scattering from a single dielectric disk is shown in Figure 2.13, and the concept for scattering from a multilayered slab is shown in Figure 2.14 [13].

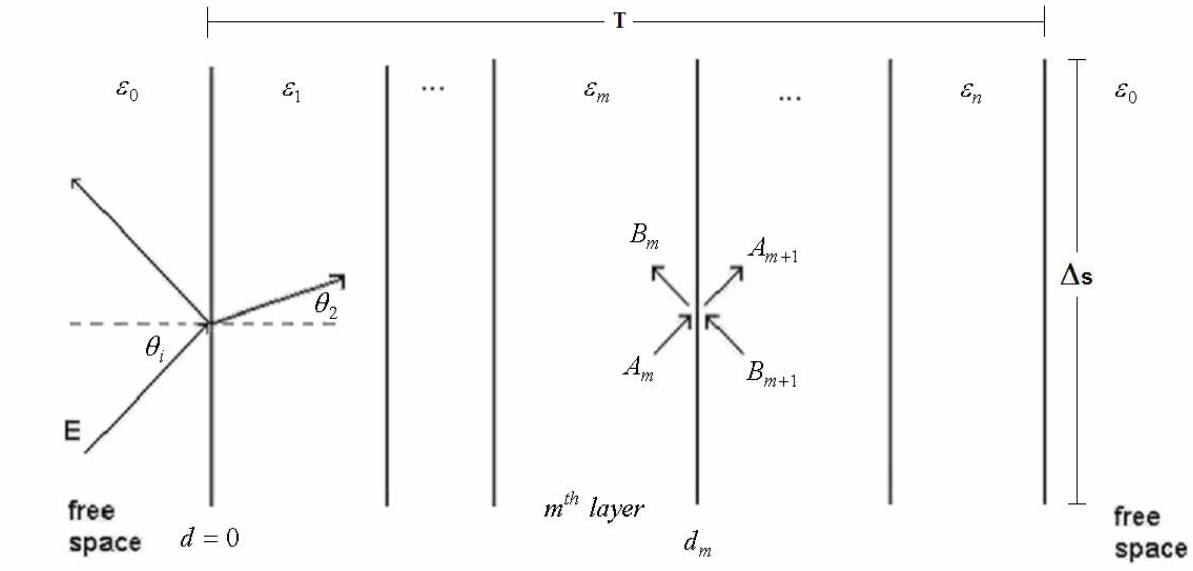

Figure 2.14. The electric fields of multilayered plates

The diagram above outlines the concept for scattering from multilayer slab. Scalar quantities are determined as follows:

A_m : Tangential E at the left interface of m^{th} layer, traveling left to right

B_m : Tangential E at the left interface of m^{th} layer, traveling right to left

C_m : Tangential H at the left interface of m^{th} layer, traveling left to right

D_m : Tangential H at the left interface of m^{th} layer, traveling right to left [15].

The horizontal and vertical electric fields inside each layer can be determined as

$$\begin{aligned} E_m^h &= A_m\, e^{-\gamma_m \cdot r} + B_i e^{\gamma_m \cdot r} \\ E_m^v &= F_m\, e^{-\gamma_m \cdot r} + G_m e^{\gamma_m \cdot r} \end{aligned} \tag{2.28}$$

where γ_m is the propagation constant in the mth layer.

An electromagnetic wave of any kind of polarization can be decomposed into its orthogonal linearly polarized components. The electric fields parallel to the interface are horizontally polarized and the fields perpendicular to the interface are vertically polarized [13].

Using boundary conditions, the coefficients for the horizontal and vertical polarized wave, having an incident angle of each layer θ_m and layer position d_m upon a multilayer dielectric slab of a relative permittivity ε_m, and the loss tangent $\tan\delta_m$, are

$$\begin{bmatrix} \frac{A_m}{B_m} \end{bmatrix} = \frac{1}{2}\begin{bmatrix} (1+Y_{m+1})e^{(\gamma_{m+1}-\gamma_m)d_m} & (1-Y_{m+1})e^{-(\gamma_{m+1}+\gamma_m)d_m} \\ (1-Y_{m+1})e^{(\gamma_{m+1}+\gamma_m)d_m} & (1+Y_{m+1})e^{(\gamma_{m+1}-\gamma_m)d_m} \end{bmatrix}\begin{bmatrix} A_{m+1} \\ B_{m+1} \end{bmatrix} \tag{2.39}$$

$$\begin{bmatrix} \frac{F_m}{G_m} \end{bmatrix} = \frac{1}{2}\begin{bmatrix} (1+W_{m+1})e^{(\gamma_{m+1}-\gamma_m)d_m} & (1-W_{m+1})e^{-(\gamma_{m+1}+\gamma_m)d_m} \\ (1-W_{m+1})e^{(\gamma_{m+1}+\gamma_m)d_m} & (1+W_{m+1})e^{(\gamma_{m+1}-\gamma_m)d_m} \end{bmatrix}\begin{bmatrix} F_{m+1} \\ G_{m+1} \end{bmatrix} \tag{2.40}$$

where $Y_{m+1} = \frac{\cos\theta_{m+1}}{\cos\theta_m}\sqrt{\frac{\varepsilon_{m+1}\left(1-i\tan\delta_{m+1}\right)}{\varepsilon_m\left(1-i\tan\delta_m\right)}}$ and $W_{m+1} = \frac{\cos\theta_{m+1}}{\cos\theta_m}\sqrt{\frac{\varepsilon_m\left(1-i\tan\delta_m\right)}{\varepsilon_{m+1}\left(1-i\tan\delta_{m+1}\right)}}$ [13].

Afterwards, substituting (2.44) into (2.27), and evaluating the integral gives the scattering amplitude for horizontal and vertical polarization as

$$f_{hh} = \sum_{m=1}^{n}\left[\frac{{k_0}^2(\varepsilon_m - 1)S_m}{4\pi}\left(A_m\frac{e^{d_m C_m} - e^{d_{m-1}C_m}}{C_m} + B_m\frac{e^{-d_{m-1}C_m} - e^{-d_m D_m}}{D_m}\right)\right] \tag{2.41}$$

$$f_{vv} = \frac{{k_0}^2}{4\pi}(K_1\cos\theta_s - K_2\sin\theta_s) \tag{2.42}$$

where $K_1 = \sum_{m=1}^{n}\left[\frac{k_{m-1}(\varepsilon_m - 1)S_m}{k_0\varepsilon_m}\left(F_m\frac{e^{d_{m-1}C_m} - e^{d_m C_m}}{C_m} + G_m\frac{e^{-d_{m-1}C_m} - e^{-d_m D_m}}{D_m}\right)\right]$,

$K_2 = \sin\theta_i\sum_{m=1}^{n}\left[\frac{(\varepsilon_m - 1)S_m}{\varepsilon_m}\left(F_m\frac{e^{d_m C_m} - e^{d_{m-1}C_m}}{C_m} + G_m\frac{e^{-d_{m-1}C_m} - e^{-d_m D_m}}{D_m}\right)\right]$,

$C_m = i(k_m + k_0\cos\theta_s)$, $D_m = i(k_m - k_0\cos\theta_s)$ and $k_m = k_0\sqrt{\varepsilon_m - \sin^2\theta_i}$.

The shape function S is very important for determination of radar cross section. The function depends on whether the shape of the slab is rectangular or circular. If the shape is rectangular, S is determined as

$$S = {X_0}^2\, Sinc(k_0 X_0\sin\theta_i) \tag{2.43}$$

So as to determine the internal electric field in a multilayered slab, i =2 is used since the internal field of interest is the layer of the dielectric slab that is second layer. It is considered first and third layer as free space.

$$f_{hh}=\frac{T{k_0}^2(\varepsilon_r-1)S}{4\pi}\left[A_2\frac{(1-e^{-z(\gamma_2\cos\theta_i+jk_0\cos\theta_s)}}{\gamma_2\cos\theta_i+jk_0\cos\theta_s}+B_2\frac{-1+e^{z(\gamma_2\cos\theta_i-jk_0\cos\theta_s)}}{\gamma_2\cos\theta_i-jk_0\cos\theta_s}\right] \tag{2.44}$$

observing that $\cos\theta_s=-\cos\theta_i$ because of the orientation of the angles

$$f_{hh}=\frac{T{k_0}^2(\varepsilon_r-1)S}{4\pi}\left[A_2\frac{(1-e^{-z(\gamma_2\cos\theta_i-jk_0\cos\theta_i)}}{\gamma_2\cos\theta_i-jk_0\cos\theta_i}+B_2\frac{-1+e^{z(\gamma_2\cos\theta_i-jk_0\cos\theta_i)}}{\gamma_2\cos\theta+jk_0\cos\theta_i}\right] \tag{2.45}$$

By using Taylor expansion for $e^x=1+x+\frac{x^2}{2!}+\frac{x^3}{3!}+\ldots$ and using the first three terms, vertical and horizontal scattering amplitude are defined as

$$f_{hh}=\frac{T{k_0}^2(\varepsilon_r-1)S}{4\pi}\left[\frac{A_2(1-z_2(\gamma_2\cos\theta_i-jk_0\cos\theta_i))+B_2(1+z_2(\gamma_2\cos\theta_i+jk_0\cos\theta_i))}{2}\right] \tag{2.46}$$

$$f_{vv}=\frac{T{k_0}^2(\varepsilon_r-1)S}{4\pi}\left[\frac{F_2(1-z_2(\gamma_2\cos\theta_i-jk_0\cos\theta_i))+G_2(1+z_2(\gamma_2\cos\theta_i+jk_0\cos\theta_i))}{2}\right] \tag{2.47}$$

Additionally, Le Vine gives the theoretical radar cross section for disks that are thin compared to wavelength ($kT<<1$) which are shown below [12]:

$$\begin{aligned}\sigma_{hh}&=\left[\frac{T{k_0}^2(\varepsilon_r-1)}{\sqrt{4\pi}}{X_0}^2\,\mathrm{sinc}(\mathrm{k}_0X_0\sin\theta)\right]^2\\ \sigma_{vv}&=\left[\frac{\sin^2\theta+\varepsilon_r\cos^2\theta}{\varepsilon_r}\right]^2\sigma_{hh}\end{aligned} \tag{2.48}$$

Radar cross section is obtained from Sarabandi's solutions by using equations (2.46) and (2.47) and results are shown in Figure 2.15, Figure 2.16, Figure 2.17, and Figure 2.18. RCS of rectangular disk's dimensions are 30.48 x 30.48 cm and its thickness is 0.0106 cm with relative dielectric constant 2.272. These results are similar with Le Vine's simulation and experimental results that are shown in Figure 2.20 and 2.21.

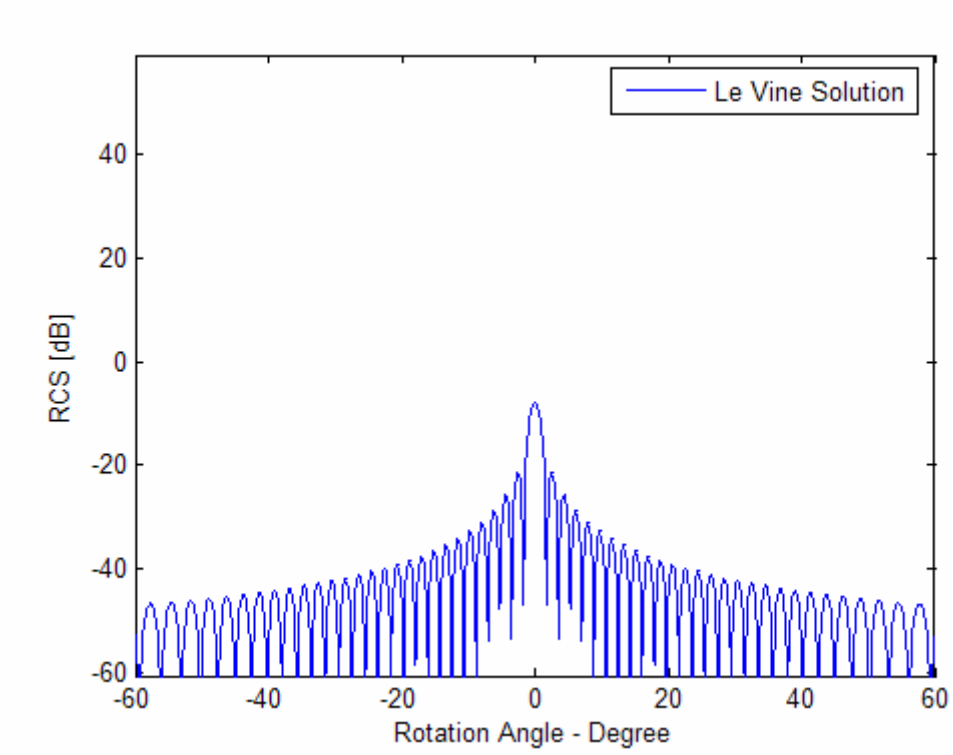

Figure 2.15. Vertical RCS of rectangular dielectric disk at 16 GHz

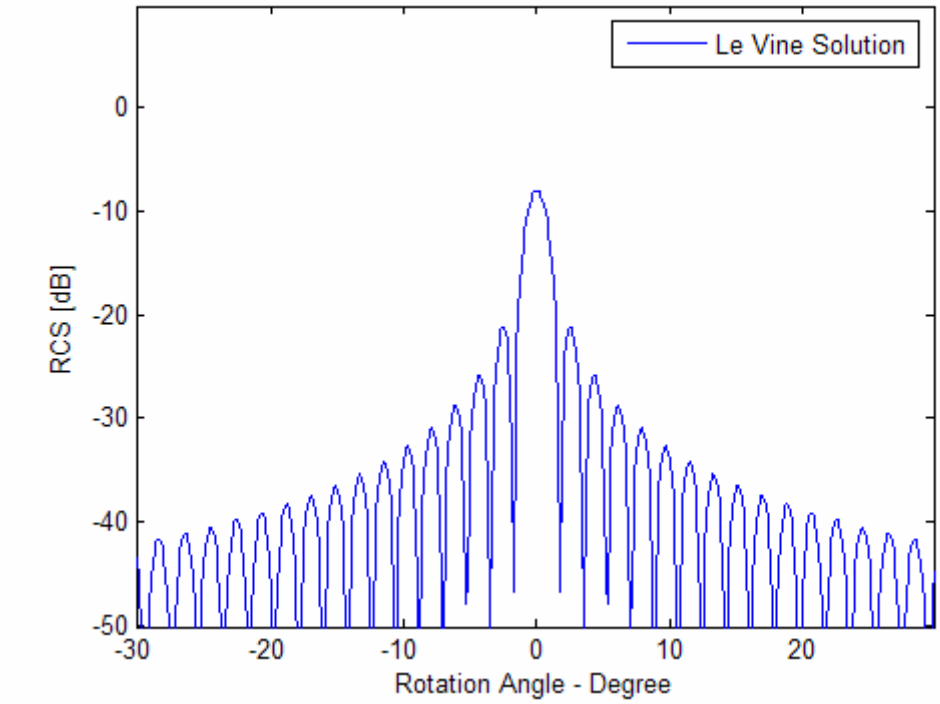

Figure 2.16. Horizontal RCS of rectangular dielectric disk at 16 GHz

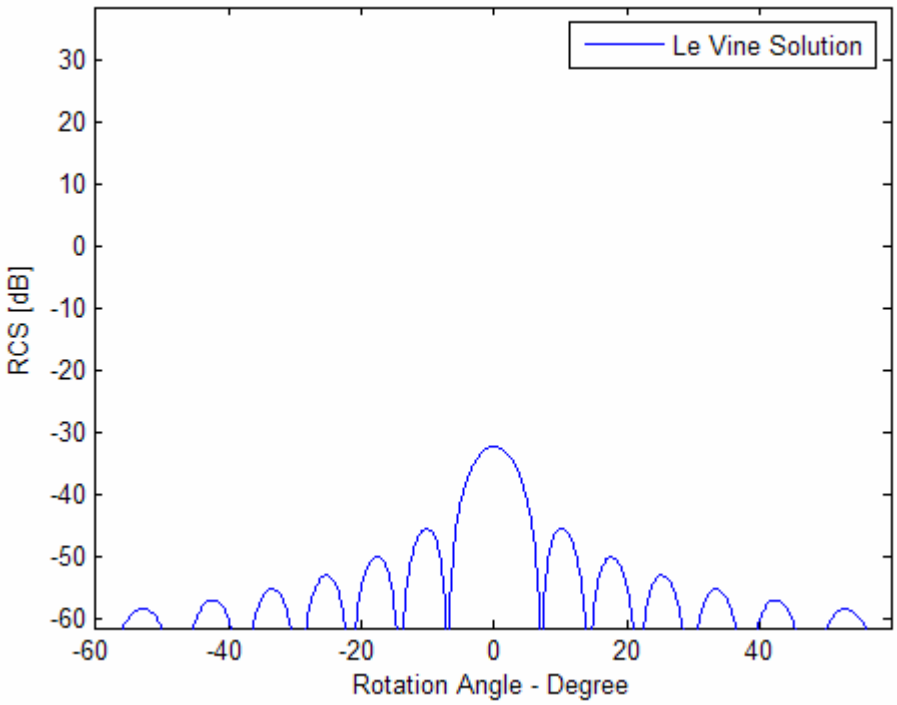

Figure 2.17. Vertical RCS of rectangular dielectric disk at 4 GHz

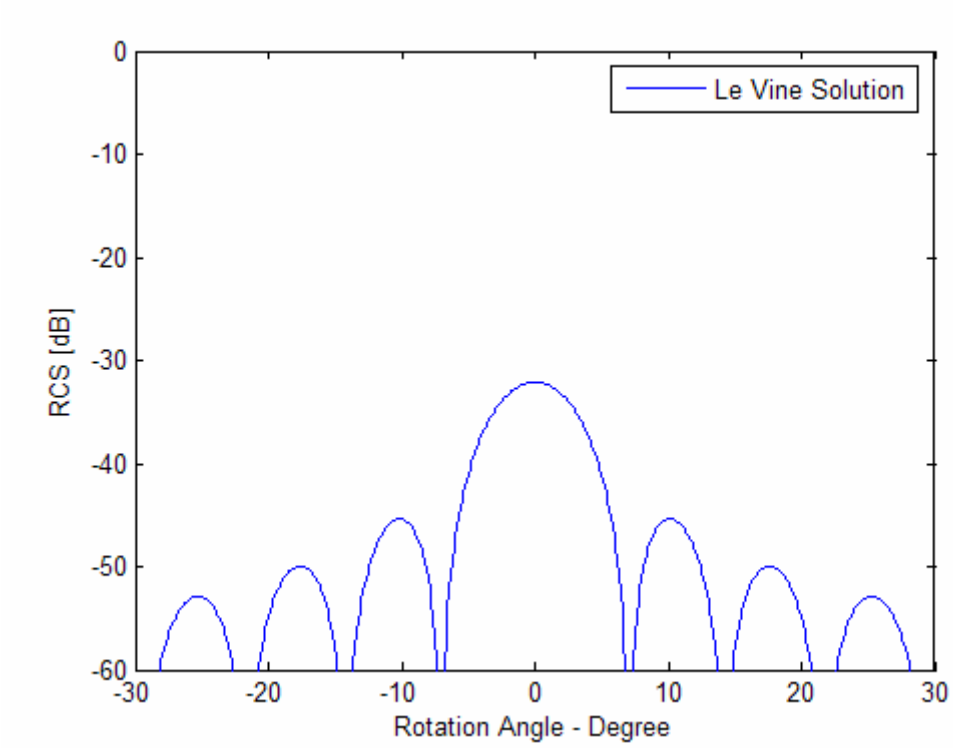

Figure 2.18. Horizontal RCS of rectangular dielectric disk at 4 GHz

Le Vine obtained same results either theoretically or experimentally that are illustrated in Figure 2.19 and Figure 2.20 [12].

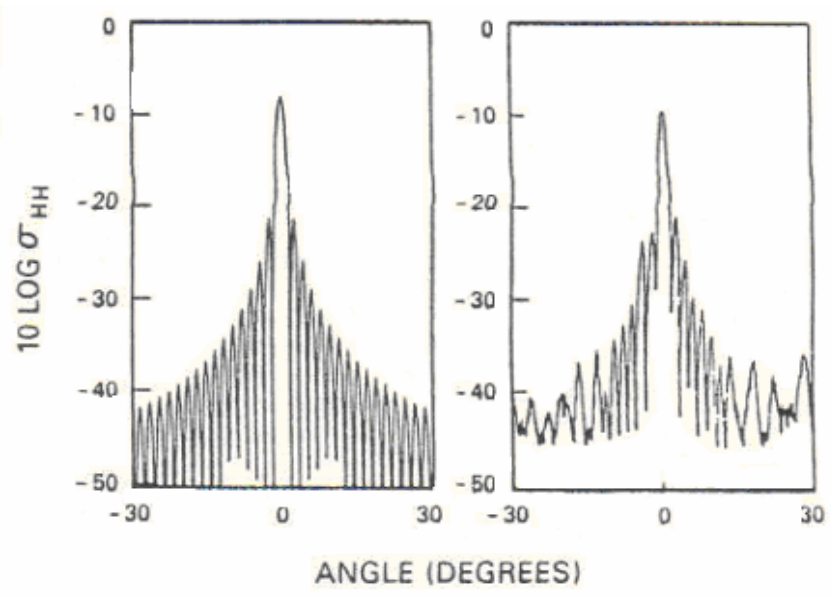

Figure 2.19. Horizontal RCS of thin rectangular disk at 16 GHz. Theory (left) and measurements (right)

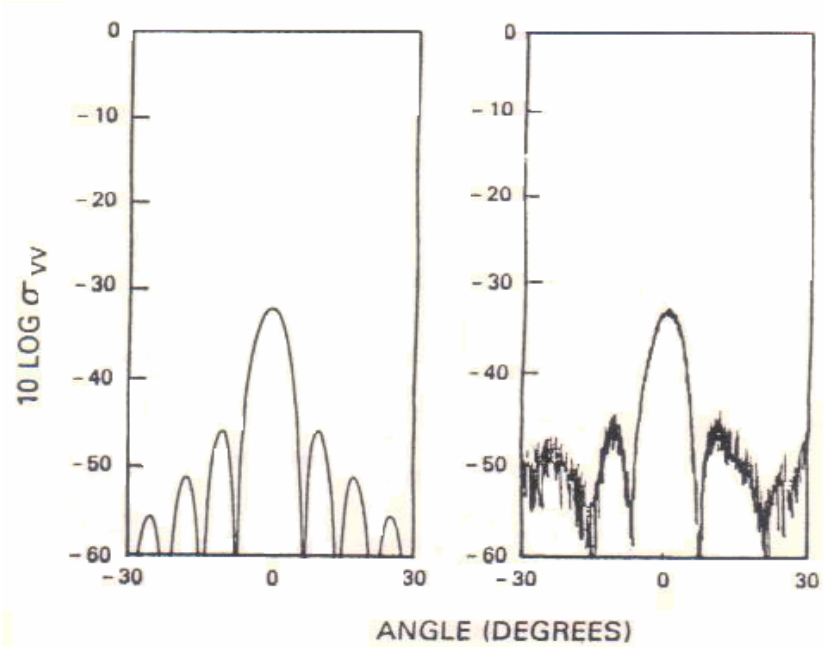

Figure 2.20. Vertical RCS of a thin rectangular disk at 4 GHz. Theory (left) and measurements (right)

2.5.4 RCS of Dielectric Cylinder

Richmond outlines the theoretical scattering solution for a plane wave incident normally on a lossy dielectric multilayer circular cylinder of infinite length in [16]. It is considered a plane wave incident normally on an arbitrary infinitely long multilayer circular cylinder. Every layer is homogenous, and the usual cylindrical coordinates are illustrated in Figure 2.21 are used.

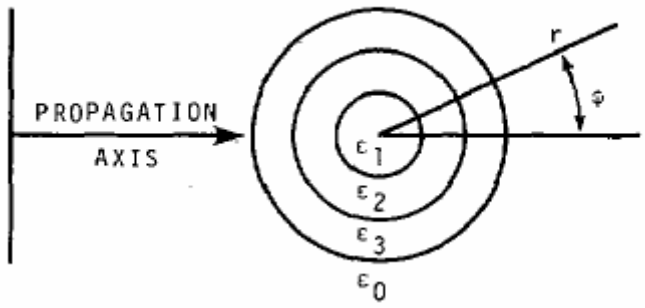

Figure 2.21. Plane wave incident on circular cylinder and circular cylindrical coordinate system

The total TM mode E-field outside of the cylinder is given by;

$$E_z = \sum_{n=0}^{\infty} \left[e_n j^{-n} J_n(k_0 r) + C_n H_n^{(2)}(k_0 r) \right] \cos n\phi \tag{2.49}$$

where k_0 is the wave number, $\omega(\mu_0 \varepsilon_0)^{1/2}$, in the outer space, J_n is a Bessel function of the first kind, $H_n^{(2)}$ is the Hankel function for outgoing waves, and later Y_n is a Bessel function of the second kind, all of order n; e_n=1, for n=0 and e_n=2 for n>0 ; j is $(-1)^{1/2}$.

In equation 2.49 the first term is the series expansion for the incident plane wave of unit amplitude. The second term represents the scattered field E^s [16].

The fields in the cylindrical space may also be represented in terms of the usual complete set. The successive layers of the cylinder are denoted by m=1,2,…,M and we take the outer space as the M+1 "layer" [16].

In layer m the internal field is;

$$E_{z,m} = \sum_{n=0}^{\infty} \left[A_{mn} J_n(k_m r) + B_{mn} Y_n(k_m r) \right] \cos n\phi \tag{2.50}$$

where $k_m = \omega(\mu_m \varepsilon_m)^{1/2}$, and μ_m and ε_m are the complex material parameters of layer m.

Without loss of generality, one may begin with the definite unnormalized amplitudes in the first layer

$$A_{1,n}' = 1 \qquad B_{1,n}' = 0 , \qquad \text{for all n.}$$

The amplitudes are stopped through the layer to the outer space, and then they are renormalized to the incident wave by equating the field $E_{z,M+1}$ of equation 2.50 to the

specified field E_z of equation 2.49. The stepping is accomplished by matching E_z and H_ϕ across such cylindrical boundary using also

$$H_\phi = (k_m / j\omega\mu_m)\sum_{n=0}^{\infty}\left[A_{mn}J_n'(k_m r) + B_{mn}Y_n'(k_m r)\right]\cos n\phi \tag{2.51}$$

where the prime indicates the derivative with respect to the argument. The A', B' (and also A, B) amplitudes are stepped but by the recursion equation [16];

$$\begin{pmatrix} A'_{m+1,n} \\ B'_{m+1,n} \end{pmatrix} = \begin{pmatrix} U_{mn}W_{mn} \\ V_{mn}X_{mn} \end{pmatrix}\begin{pmatrix} A'_{m,n} \\ B'_{m,n} \end{pmatrix} \tag{2.52}$$

where

$$\begin{aligned}
U_{mn} &= \mu_m k_{m+1} J_n(k_m r_m)Y'_n(k_{m+1}r_m) - \mu_{m+1}k_m J'_n(k_m r_m)Y_n(k_{m+1}r_m) \\
V_{mn} &= \mu_{m+1} k_m J_n(k_{m+1} r_m)J'_n(k_m r_m) - \mu_m k_{m+1} J'_n(k_{m+1} r_m)J_n(k_m r_m) \\
W_{mn} &= \mu_m k_{m+1} Y_n(k_m r_m)Y'_n(k_{m+1}r_m) - \mu_{m+1}k_m Y'_n(k_m r_m)Y_n(k_{m+1}r_m) \\
X_{mn} &= \mu_{m+1} k_m Y'_n(k_m r_m)J_n(k_{m+1} r_m) - \mu_m k_{m+1} Y_n(k_m r_m)J'_n(k_{m+1} r_m)
\end{aligned} \tag{2.53}$$

Equating coefficients of E_z of equation 2.49 and E_z of equation 2.50 in the outer space, it is found that

$$C_n = jB_{M+1,n} \tag{2.54}$$

$$A_{M+1,n} - jB_{M+1,n} = j^{-n}e_n \tag{2.55}$$

Normalization constant K_n is defined for the primed amplitudes:

$$A_{mn} = K_n A_{mn}^{'}, \quad B_{mn} = K_n B_{mn}^{'} \tag{2.56}$$

so that equation 2.56 becomes

$$K_n \left(A^{'}_{M+1,n} - jB^{'}_{M+1,n} \right) = j^{-n} e_n \tag{2.57}$$

which gives K_n since A' and B' are known from the successive recursions indicated in equation 2.52.

The final calculated scattering amplitudes, using equations thorough 2.54 to 2.57, are

$$C_n = -j^{-n} e_n \left[B^{'}_{M+1,n} / \left(B^{'}_{M+1,n} + jA^{'}_{M+1,n} \right) \right] \tag{2.58}$$

which completes the formal solution.

Using the asymptotic form of the Hankel function, the calculated scattered far-field is

$$E_s = \left(2j / \pi k_0 r \right)^{1/2} e^{-jk_0 r} \sum_{n=0}^{\infty} e_n D_n \cos n\phi \,, \quad E_s = f \frac{e^{-jk_0 r}}{\sqrt{r}} \tag{2.59}$$

where

$$D_n = j^n C_n / e_n = -B^{'}_{M+1,n} / \left(B^{'}_{M+1,n} + jA^{'}_{M+1,n} \right) \tag{2.60}$$

omitting the subscripts for brevity. The incident field at the cylinder origin is $e^{j\omega t}$.

In summary, the amplitudes $A^{'} = 1$ and $B^{'} = 0$ of the inner core are stepped by recursion in equation 2.52 to the outer space, and these are sufficient to specify the scattered field. The correct normalized amplitudes within the cylinders are obtained from equations 2.56 and 2.57 [16].

The total forward scattering amplitude coefficient is given by

$$T(0) = \sum_{n=0}^{\infty} e_n D_n \tag{2.61}$$

that is the sum in (2.59) with $\phi = 0$. A backscattering power cross section can be determined as [17],

$$P(\pi) = (4/k_0)|T(\pi)|^2 \tag{2.62}$$

where $T(\pi)$ is the sum in equation (2.59) with $\phi = \pi$.

When a plane wave is incident on a cylindrical structure of infinite length, the distant scattering pattern is conveniently described by the echo width that is defined as follows [18]:

$$W = \lim_{r \to \infty} 2\pi r \left| E_s / E_i \right|^2 \tag{2.63}$$

From equations (2.59) and (2.63) the bistatic echo width of the multilayer dielectric cylinder is given as follows:

$$W = 2\lambda / \pi \left| \sum_{n=0}^{\infty} e_n D_n \cos n\phi \right|^2 \tag{2.64}$$

where λ is the wave length in free space [18].

The TE mode solution is obtained from the preceding using duality by interchanging μ and ε, replacing *E* by *H*, and *H* by *–E*. The present recursive method avoids the necessity of inverting a 2*N* square matrix, where *N* is the number of layers.

In [18], Richmond gives the graph for the lossless dielectric cylinder whose parameters are given in table below:

Table 2.2. Parameters of the multilayer circular cylinder

Number of Layer	Radius (m)	$\varepsilon / \varepsilon_0$
1	0.1	6
2	0.2	5
3	0.3	4
4	0.4	3
5	0.5	2

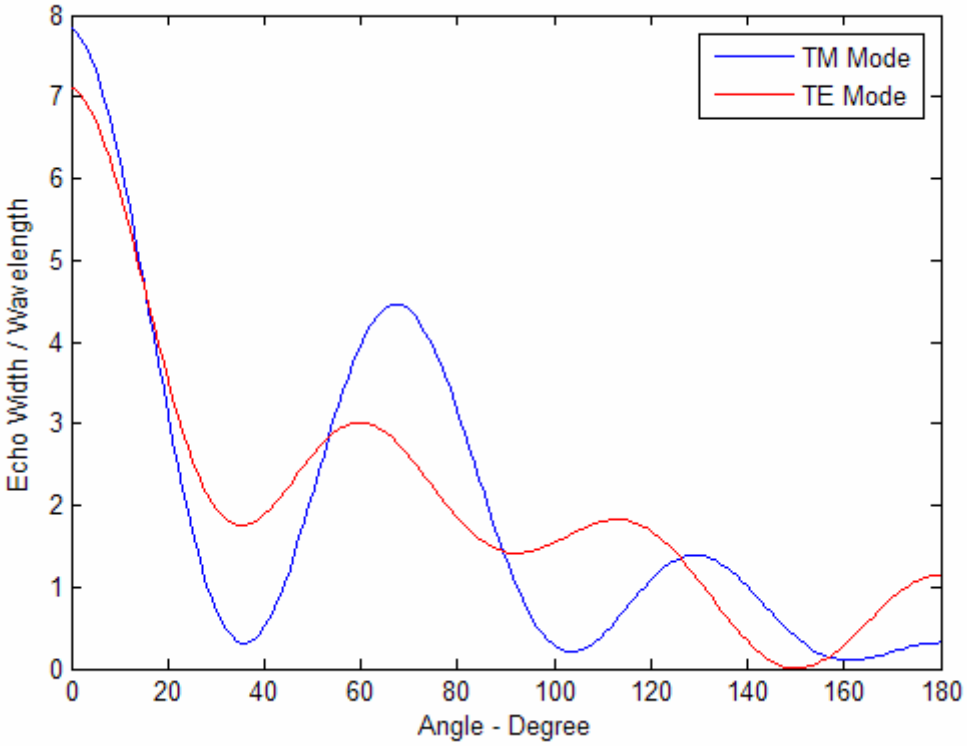

Figure 2.22. Echo width / wavelength of multilayered cylinder for TM and TE mode at 0.3 GHz

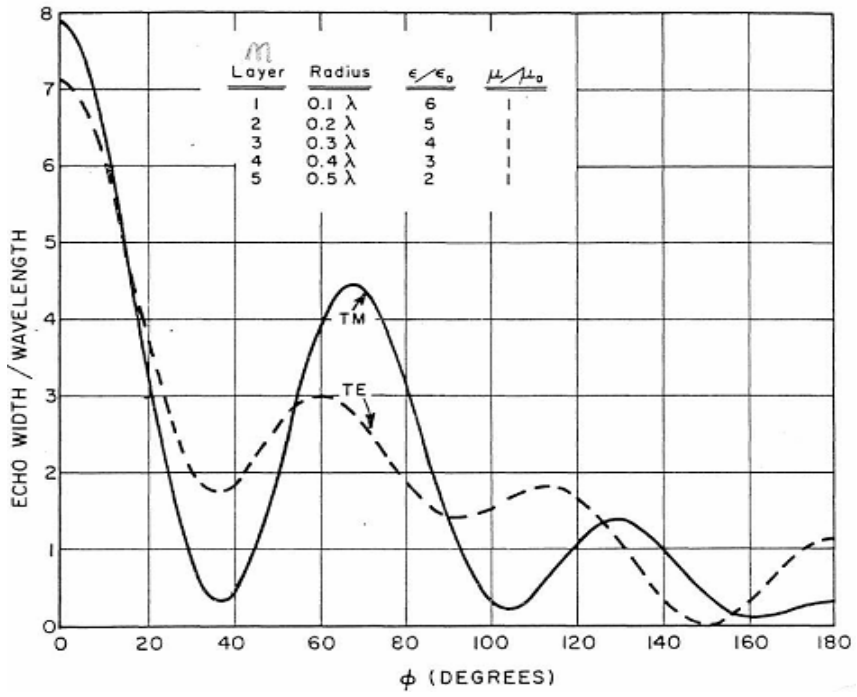

Figure 2.23. Echo width / wavelength of multilayered cylinder for TM and TE mode calculated by Richmond at 0.3 GHz

Figure 2.22 shows a perfect agreement with the Figure 2.23 that is calculated by Richmond in [18].

In this thesis, so as to obtain the internal electric field in a multilayered cylinder, second layer of multilayered cylinder is used, and first and second layer of multilayered cylinder will be thought as free space. According to this thought, the echo width / wavelength of dielectric hollow cylinder, whose parameters is given in Table 2.3, for TM and TE mode that is illustrated in Figure 2.24 is obtained by using the Richmond's solutions at 3 GHz.

Table 2.3. Parameters of the multilayer circular cylinder

Number of Layer	Radius (m)	$\varepsilon / \varepsilon_0$
1	0.053	1
2	0.05537	2.7
3	0.05537	1

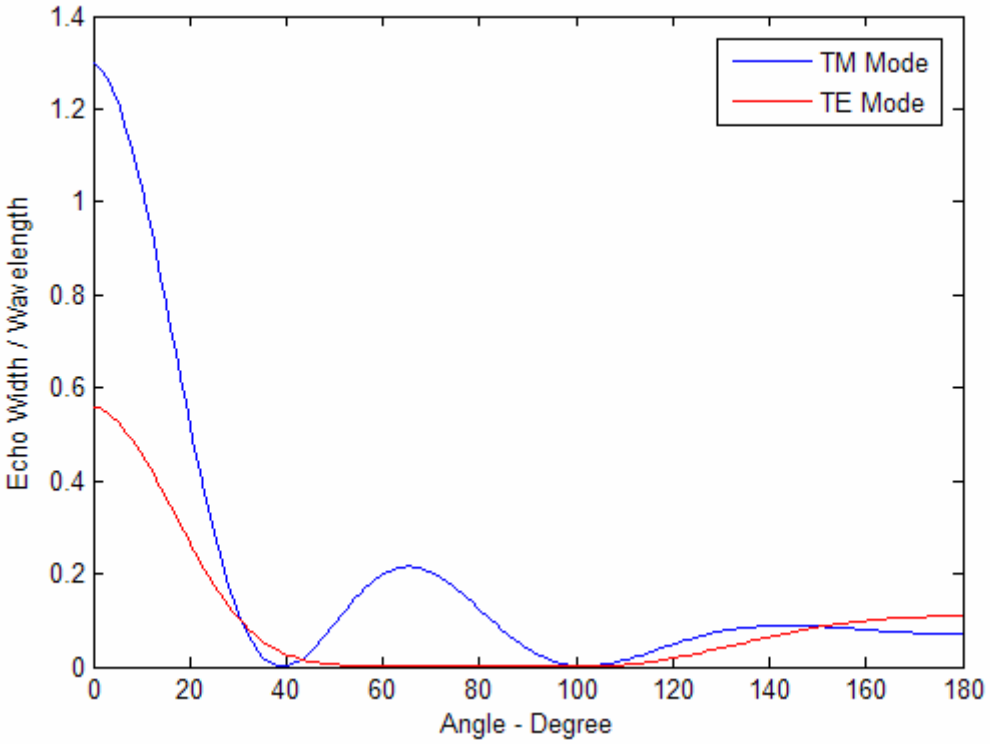

Figure 2.24. Echo width / wavelength of hollow cylinder for TM and TE modes

3. MEASUREMENT METHODS IN LITERATURE

There are three fundamental elements for measuring radar cross sections. These elements are a source or radiator of electromagnetic energy, an obstacle or scatterer of energy, and a receiving antenna or probe that measures the properties of an electromagnetic field resulting from source currents in the absence of the scatterer is termed incident field. The electromagnetic field resulting from the same source currents but with the scatterer present is termed the total field. The vector difference at each point between the total field and the incident field is termed the scattered field [7].

Measurement methods can be classified according to how the transmitted and received fields are separated. The incident field and scattered field may be separated by a difference in propagation direction (magic-T, two-antenna, SWR systems), by a frequency difference (Doppler and FM systems), or by a time delay (pulsed systems) [7].

3.1 Differences in Propagation Direction

3.1.1 Hybrid Junction Cancellation

A single antenna hybrid junction (Magic-T) system is necessary for the continuous wave (CW) cancellation method. A magic-T is a waveguide junction that can be represented as a four-terminal network. If the four terminals are ended in matched or balanced impedances, a signal entering any terminal will separate equally between the two adjacent terminals and be effectively isolated from the fourth. A typical arrangement is illustrated in Figure 3.1 [7].

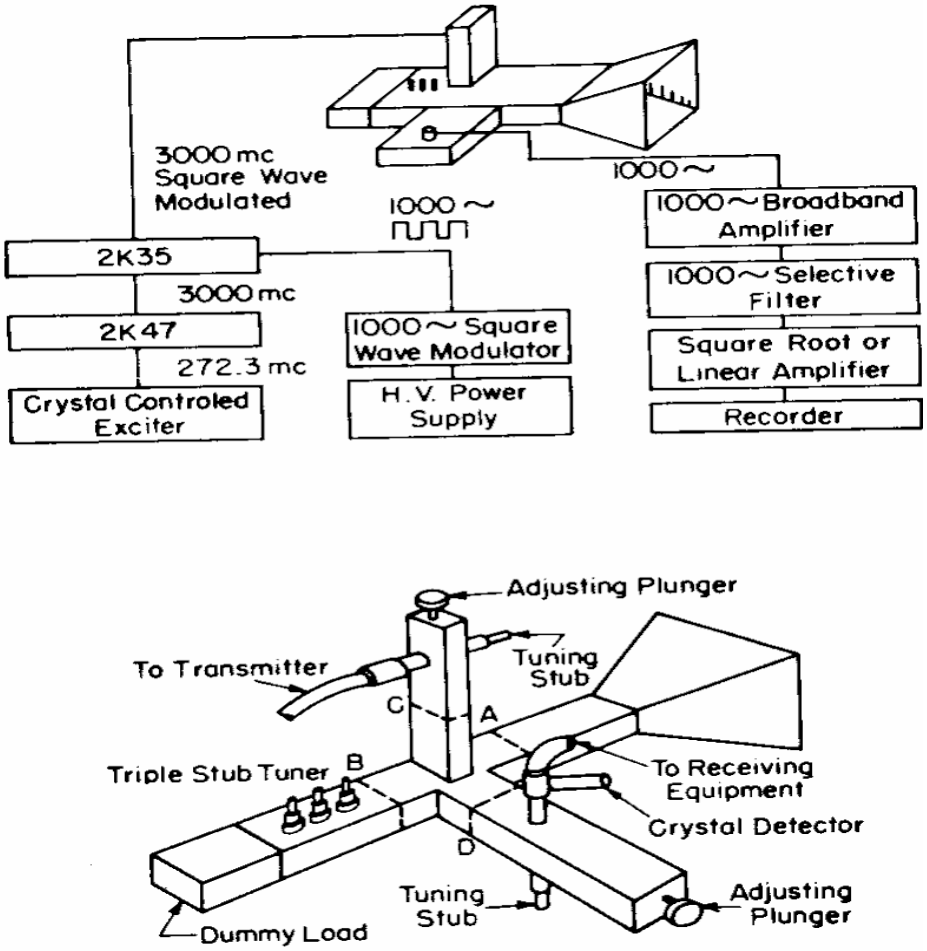

Figure 3.1. Magic-T method

A transmitter is joined to arm C, a matched load to arm B, a receiver to arm D, and an antenna to arm A. Under balanced conditions, a continuous wave originating at the transmitter will separate equally between the transmitting antenna and the matched load. A received signal (that will be much smaller in amplitude than the transmitted signal) appearing at the antenna will separate between the receiver and transmitter. Beneficial use of only half of the transmitted and received powers is not a problem, since target ranges are small compared to those a field radar. The matched load can be regulated to a small degree of mismatch, concluding reflection of a small amount of transmitter signal back into the receiver arm. This signal can be regulated in amplitude and phase to effectively cancel out any received signal. If this nulling is achieved in the absence of a scatterer, the background return is effectively removed at the receiver. Upon introduction of scatterer, the receiver output is then a measure of the target cross section. In order to accurate measurement,

frequency stability of the source must be accurately provided, and the introduction of the scatterer must not substantially alter the magnitude and phase of the background return. Isolation between transmitter and receiver must be the order of 100 db for accurate measurement of target nulls as illustrated in Figure 3.2 [7].

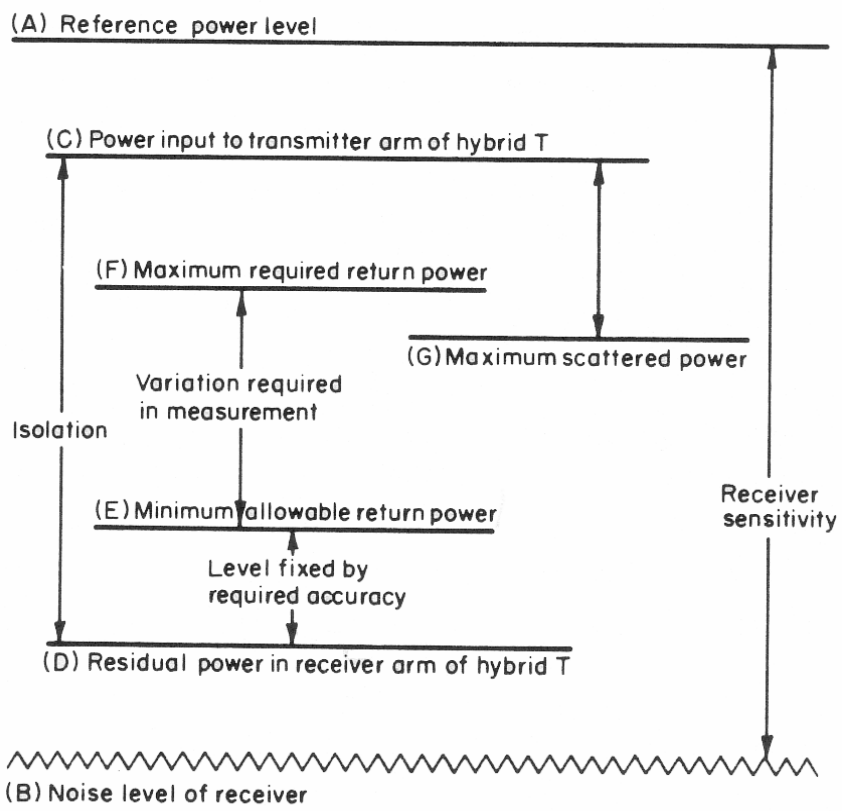

Figure 3.2. Cancellation requirements in a CW system

The needed isolation is the difference in power level between the power input to the transmitter arm of the magic-T and residual power in the receiver arm after the background is cancelled. This case is defined by the difference between transmitter power and maximum scattered power; by the difference between scattered power and minimum scattered power and minimum scattered power (at nulls of the scattering pattern); and by the difference between the minimum scattered power and residual uncancelled power. The last difference is a function of required measurement accuracy. Figure 3.3 illustrates the variation in isolation with altering transmitter frequency for the system of Figure 3.1. It is seen that the transmitter must be highly monochromatic and maintain frequency stability for the duration of the measurement [7].

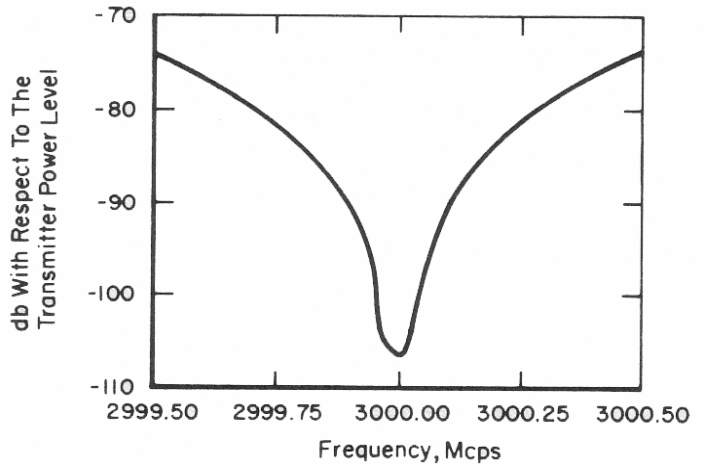

Figure 3.3. Variation in isolation with changing frequency

3.1.2 Two-Antenna Method

Using separate antennas for transmitting and receiving can eliminate the requirement for a magic-T waveguide junction; bistatic and quasimonostatic measurements can be made with a two-antenna system. Figure 3.4 illustrates the magnitude of the bistatic angle as a function of range when the bore sights of transmitting and receiving antennas are divided by one and by two antenna diameters. For quasimonostatic measurements, the bistatic angle should be kept smaller than the smallest increase in view angle that gives significant variation in cross section. In several conditions, this needs greater range separation between scatterer and antennas than is required to achieve approximate plane-wave illumination. An important thought with a two-antenna system is the isolation between the transmitting and receiving antenna channels, particularly when making cross-polarized measurements [7].

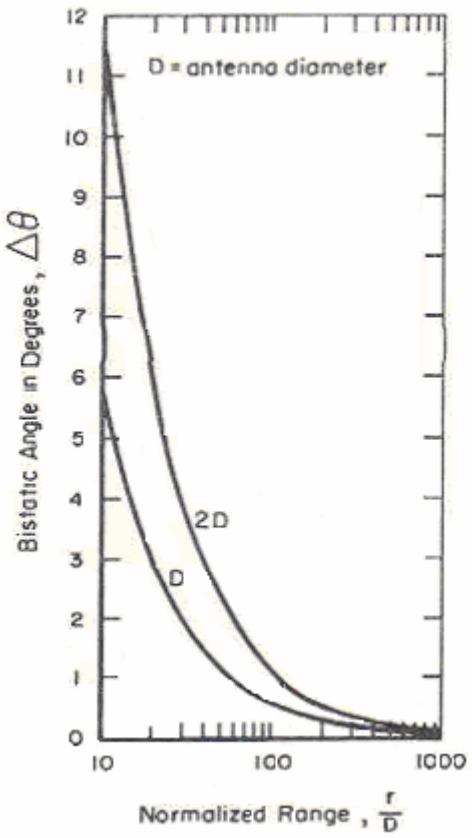

Figure 3.4. Bistatic angle as a function of range and antenna separation for separate transmitting and receiving antennas

3.1.3 SWR Method

By using field probes illustrated in Figure 3.5, direct measurements of the scattered and incident fields can be made, deviating the requirement for calibration targets. Small monopoles are generally used with an image plane that protects the probe transmission line and other required equipment from direct illumination and ignores the requirement for modal supports [7].

The monopole is moved through a line between the source and the target in order to measure the amplitudes of standing waves caused by interference between the incident field and scattered field. The reflection coefficient of the target is determined;

$$b = lw_2 \frac{[\rho/(l-w_2)] - [1/(l-w_{1)}]}{\rho + (w_2/w_1)} \tag{3.1}$$

where b is the constant, w_2 is the distance from the scatterer to a null in the total field; w_1 is the distance from the scatterer to a maximum in the total field; l is the distance from source to scatterer.

The measured voltage standing-wave-ratio, ρ, is defined by this equation $\rho = (E_i + E_s)/(E_i - E_s)$ [7].

The backscattering cross section is determined by

$$\sigma = 4\pi b^2 \tag{3.2}$$

Use of an image plane limits the types of targets to those with planar symmetry, and the field polarization to a linear polarization perpendicular to the image plane. A single image plane imitates a free-space geometry, including the geometry above the plane together with the mirror image of this geometry. Scattering from infinite cylindrical targets can be imitated for polarization parallel to the cylinder axis by using two parallel image planes [7].

SWR definitions assume that the probe is in the far field of both source and obstacle, so that energy propagates nearly as a plane wave. The incident field polarization and scattered field polarization are parallel so that interference will happen. The probe does not perturb the field in the vicinity of either the source or the obstacle [7].

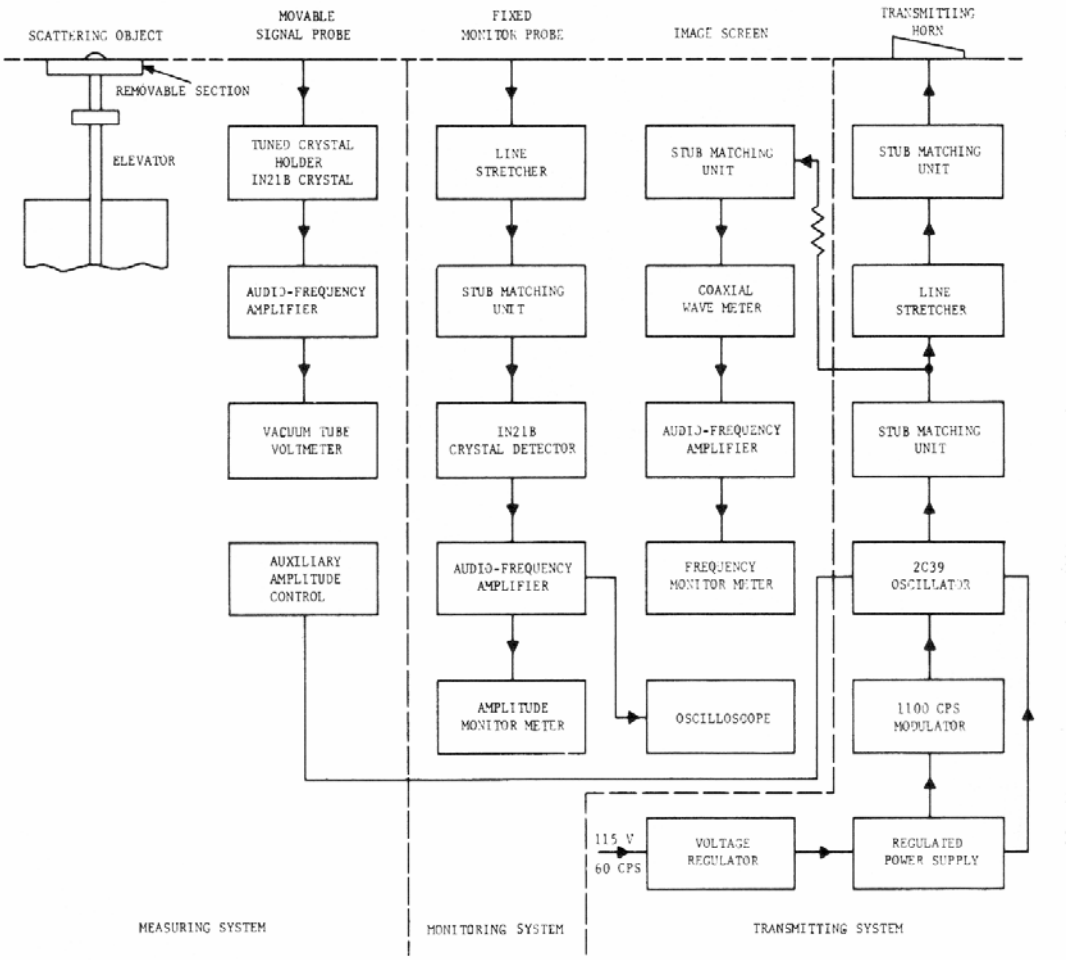

Figure 3.5. The SWR method

3.1.4 Fixed-Probe Cancellation Method

Figure 3.6 shows the fixed probe cancellation method that can be used in the same geometries as the SWR method. However, the probe is fixed, and cancellation techniques are used to null the probe output voltage when the obstacle is not present. When the obstacle is added, the probe voltage is balanced with the scattered field [7].

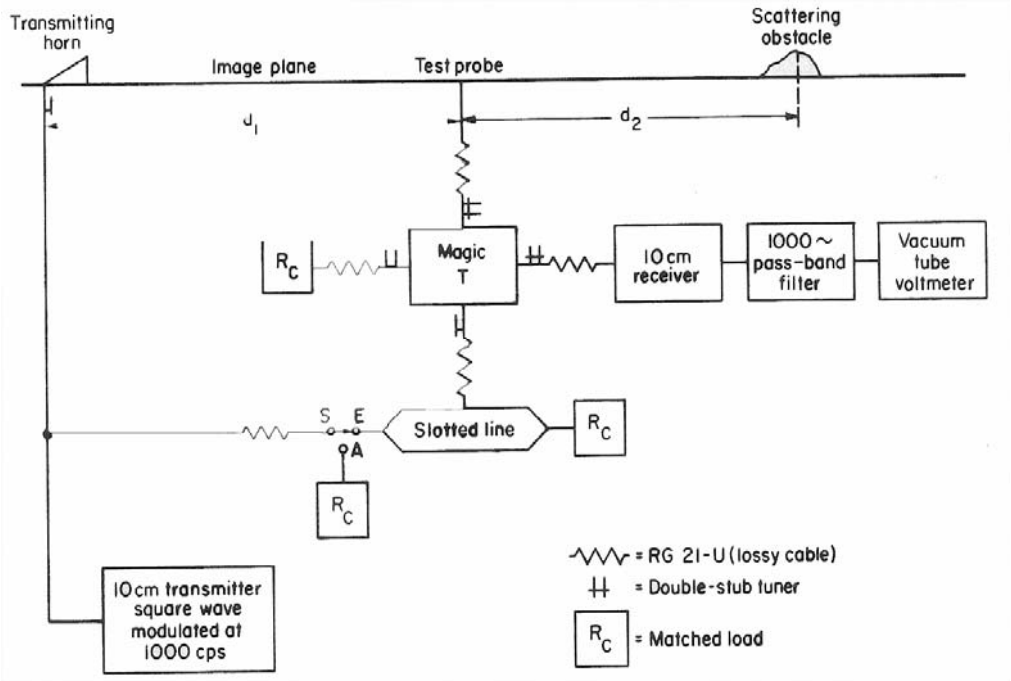

Figure 3.6. The fixed-probe cancellation method

3.2 Modulation Methods (Frequency Differences)

3.2.1 Doppler Method

Separation of scattered field and incident field can also be achieved by modulating either field at the transmitter or at the obstacle. If the obstacle is given component of velocity along the direction of illumination, the scattered field will be shifted in frequency and may be separated on this basis. Figure 3.7 illustrates a Doppler system that is used with a “free-space” range, and Figure 3.8 illustrates a similar technique applied to parallel-plane geometry. In both cases, the obstacle and calibrating object are mounted on a rotating disc [7].

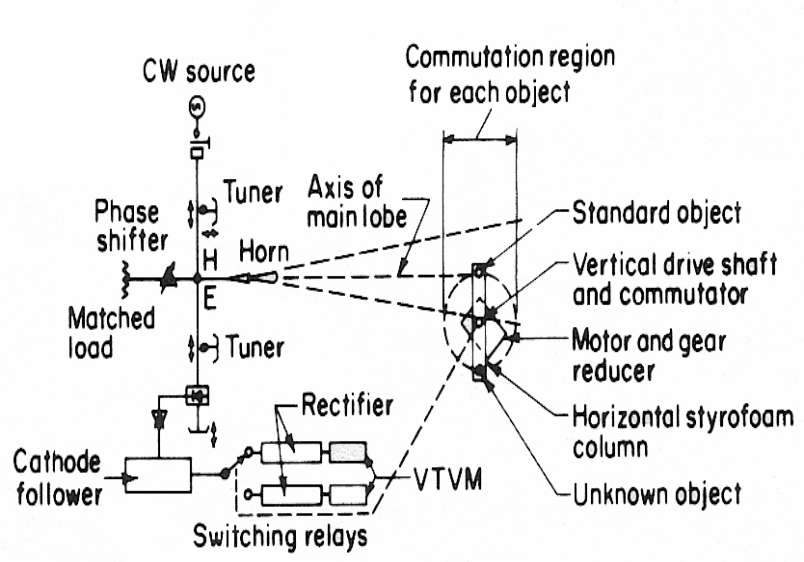

Figure 3.7. A free space doppler measurement system

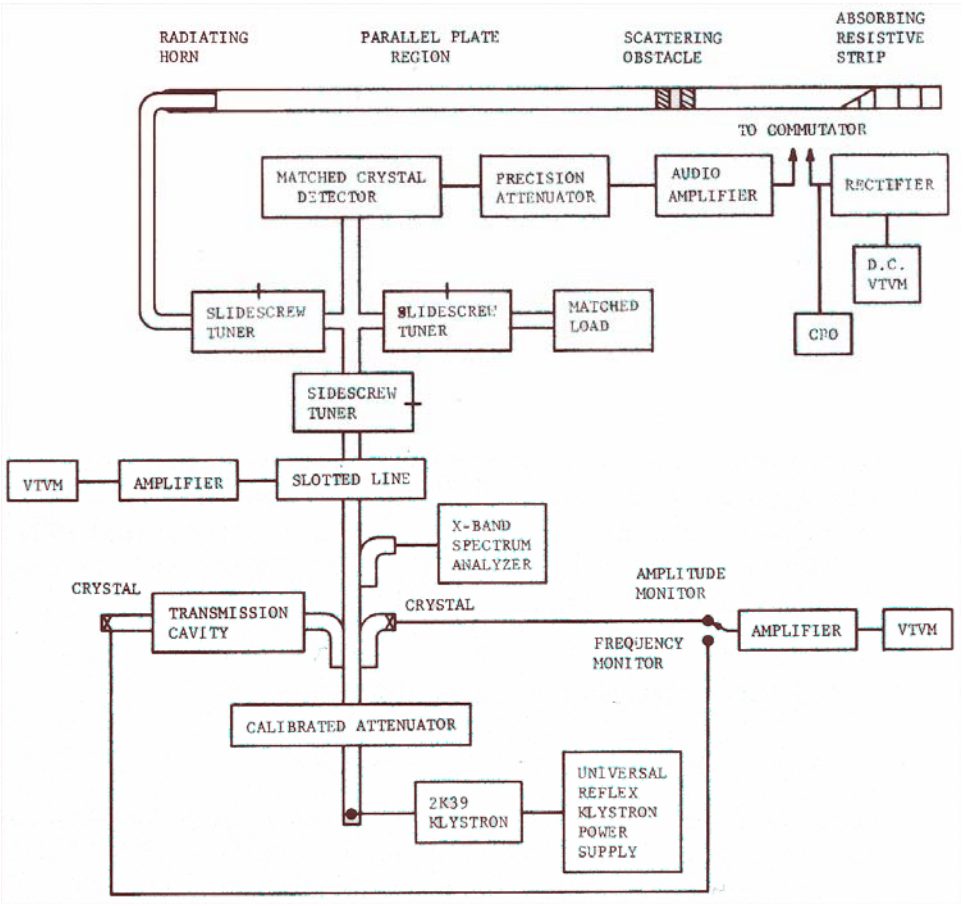

Figure 3.8. A parallel plane doppler measurement system

3.2.2 FM-CW Method

Separation of the scattered field from the incident and undesired background fields can also be achieved by frequency modulating the incident field. After reflection from scatterer, an incident field of frequency f_0 at the time t_0 will return to the receiver at time $t = t_0 + (2r/c)$, where r is the distance between the transmitter and the scatterer and c is the velocity of light. If the transmitted frequency is modulated at a ratio of df/dt, then the frequency of the received signal will be;

$$f = f_0 + (2r/c)df/dt \tag{3.1}$$

If this is mixed with a sample of the transmitted signal, then the difference frequency of $(2r/c)df/dt$ can be recovered, and the amplitude of this difference-frequency signal will be proportional to the cross section of the scatterer [7].

Discrimination against background echoes from sources at ranges other than that of the target can be achieved by filtering so that only the difference frequency corresponding to the target range is retained. This procedure is done easily if linear frequency modulation is used, thus giving a difference frequency that is constant with time. Linear, saw tooth frequency modulation is most often used. If the carrier frequency is swept linearly through a maximum deviation Δf in t' seconds, and repeats this $f_m = 1/t'$ times per second then the difference frequency from a target at range r will be

$$f_d = (2r/c) f_m \Delta f \tag{3.2}$$

Because the carrier frequency is not constant, measured cross section will not be a true CW (Continuous Wave) cross section but some type of average over a portion of the deviation frequency. So as to approximate the CW cross section as closely as possible, the modulation rate should be kept low in order that frequency change during time needed for the wave to pass over scatterer is small [7].

Unfortunately, a spectral analysis of the difference frequency generated by such a system illustrates that energy occurs not at a single frequency f_d, but at f_d and all harmonics of f_d, and possesses a finite spread around these points. As a result, complete rejection of unwanted background signals is not probable. Special difficulties can be encountered with large background sources near to the transmitter that can produce significant energy in the spectral region where the wanted scattered signal is located [7].

Identically, any amplitude modulation of the transmitted signal can produce energy in that portion of the spectrum where the wanted signal lies. Consequently, any residual amplitude modulation of the transmitted signal must be minimized [7].

3.3 Pulse Systems

The scattered fields can be separated from the incident and background fields on the basis of time differences. This is achieved by using a pulse system to measure the target cross section. A pulse measuring system is actually simplified radar adapted for measurements at short ranges. These systems generally use pulse widths ranging from 0.1 to 1 μsec, and repetition rates of 500-25,000 cps [7].

4. RADAR CROSS SECTION MEASUREMENTS AND SIMULATIONS

4.1. Measurement System Architecture

In previous sections, the theoretical RCS calculations and measurement systems were established. This section deals with the practical tasks of data acquisition system. Measurements were done in Electromagnetic Diagnostic and Measurement Laboratory in İstanbul Technical University. Figure 4.1 illustrates the experimental environment, Figure 4.2 shows the hardware components of the RCS measurement system, and Figure 4.3 shows the one example of antennas. The permittivity of Dielectric models was measured in TÜBİTAK–UEAKE in EMC laboratory. So as to measure permittivity, HP 4291A RF Impedance/Material Analyzer and 16453A Dielectric Material Test Fixture units were used to measure.

Figure 4.1. Electromagnetic diagnostic and measurement laboratory-İTÜ

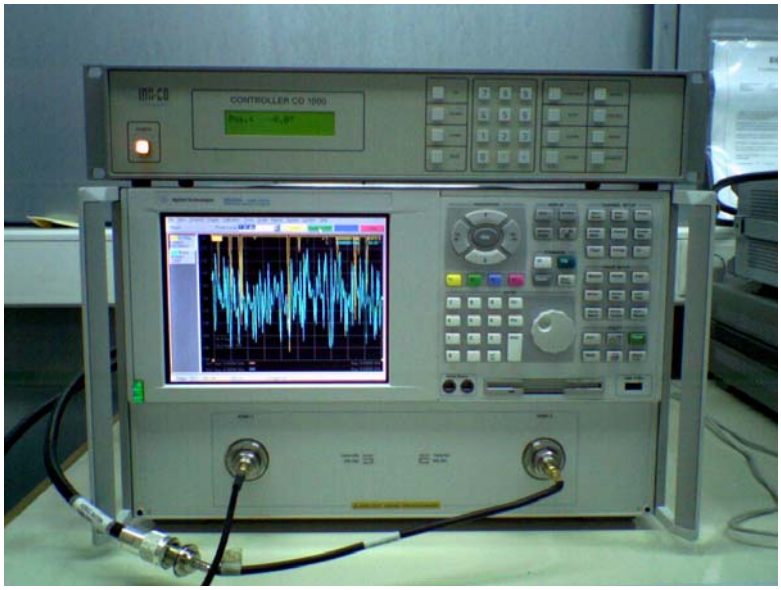

Figure 4.2. Hardware components of measurement system

Figure 4.2 shows the controller (CO 1000) and PNA series Network Analyzer (Agilent Technologies - N5230A). Network analyzer operates at frequency ranges from 10 MHz to 40 GHz. It measures S parameters.

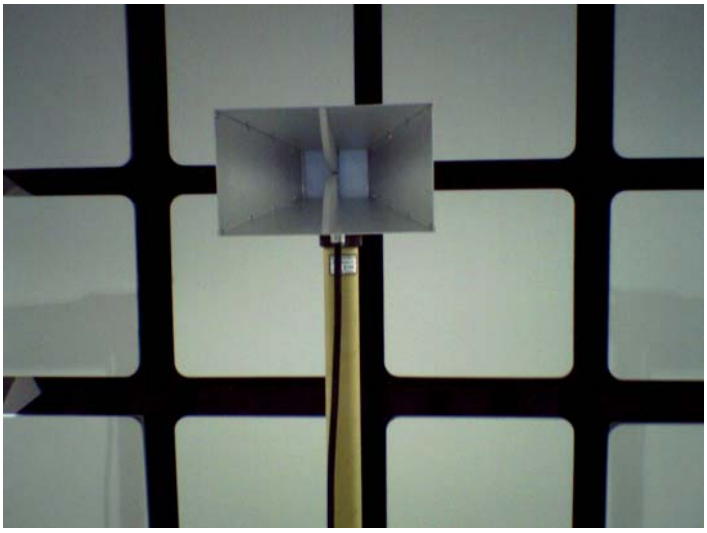

Figure 4.3. An example of antenna for vertical polarization

Two antennas are used for transmission and reception purposes that are connected to the ports of the network analyzer. Figure 4.3 shows one example of antenna that was used to measure for vertical polarization.

In order to calculate the RCS, S_{21} parameters were measured. When an object scatters an electromagnetic wave, the scattered field is determined as the difference between the total field in the presence of the target and the incident field that exists if the target was absent. So, firstly, when the target is not found in anechoic chamber, S_{21} values were measured for free space, called $S_{21}{}^{i}$. Afterwards, the target was located on the turntable and, S_{21} parameters were again measured. These values were the total field, $S_{21}{}^{t}$ and the scattering field can be evaluated as;

$$\left|S_{21}{}^{s}\right|^2 = \left|S_{21}{}^{t} - S_{21}{}^{i}\right|^2 \tag{4.1}$$

The difference between the total and incident field is related to scattering, and it is used to calculate RCS by using (2.6) and (2.7) for three and two-dimensional objects. This relation is given as shown below;

$$\frac{\left|E_z{}^{s}\right|^2}{\left|E_z{}^{i}\right|^2} = k.\left|S_{21}{}^{t} - S_{21}{}^{i}\right|^2 \tag{4.2}$$

where k is a calibration coefficient. This coefficient is used to get good agreement between theoretical and experimental results.

4.2. Radar Cross Section Measurement in Experimental Environment

The purpose of the following experimental measurements is to verify that the results of measurements are compatible with the results given in literature. The first group includes geometrically simple shapes such as cylinder, flat plate either conducting or dielectric materials to compare with the results obtained by Ross, Balanis, and Richmond in [10], [11], [18]. After simple shapes, RCS measurements would be done for arbitrary shapes obtained from hollow cylinder to compare with Discretization Method given in [14]. And then, RCS would be gained for arbitrary shape, such as leaf. Unfortunately, measurements were not completed due to laboratory troubles.

4.2.1. RCS of Conducting Rectangular Flat Plate

First measurement was done for flat plate and measurement result was compared with Ross's solution given in [10]. The frequency was chosen as 3 GHz because cable interference occurs when the frequency is high. Measurement was done for vertical polarization and increment in angle was selected as 5°. Aluminum plate's dimensions are 14x14 cm and Figure 4.4 illustrates the target placed on turntable. Figure 4.5 shows the result of comparison between experimental and theoretical RCS of aluminum flat plate for vertical polarization at 3 GHz.

Figure 4.4. Aluminum flat plate located at turntable in anechoic chamber

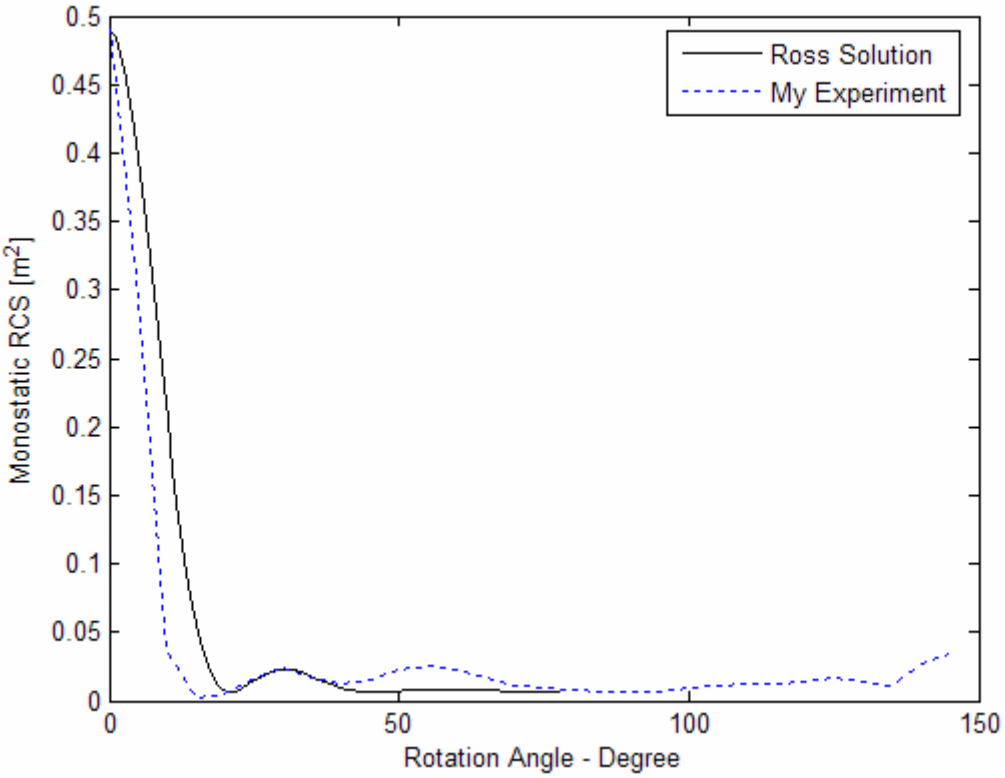

Figure 4.5. Vertical RCS of aluminum flat plate at 3 GHz

Comparing the pairs in Figure 4.5 indicates good agreement between Ross's solution and my measurement result. Edge effects are clearly evident in this data when the incidence angle is greater than about 50°.

4.2.2. RCS of Perfectly Conducting Cylinder

Cylinder is another simple geometry chosen to make the RCS measurement, and it is shown in Figure 4.6. Perfectly conducting cylinder's radius is 6 cm, its material is copper and measurement was done at 3 GHz with 6° angular steps to obtain Bistatic RCS for vertical polarization.

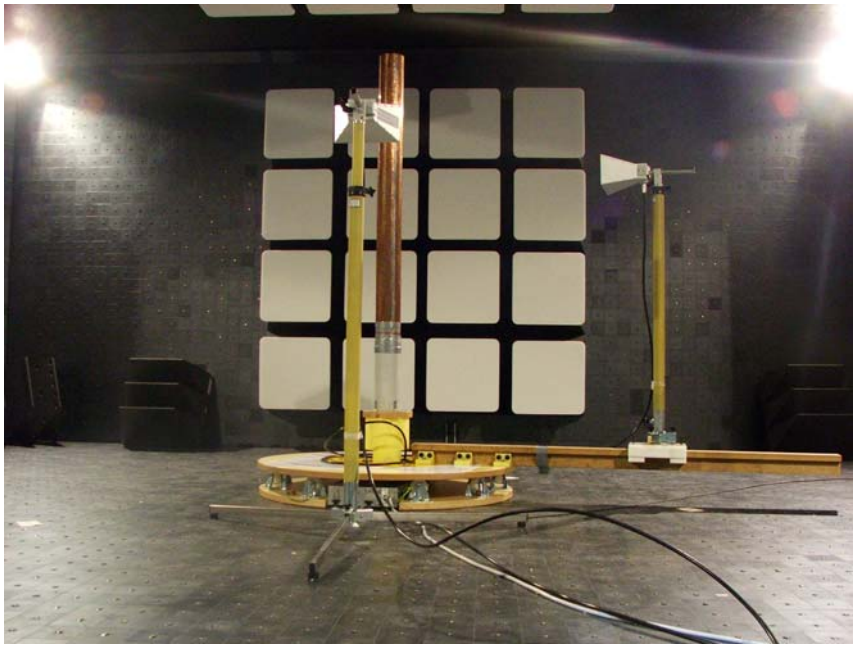

Figure 4.6. Perfectly conducting cylinder located at turntable in anechoic chamber

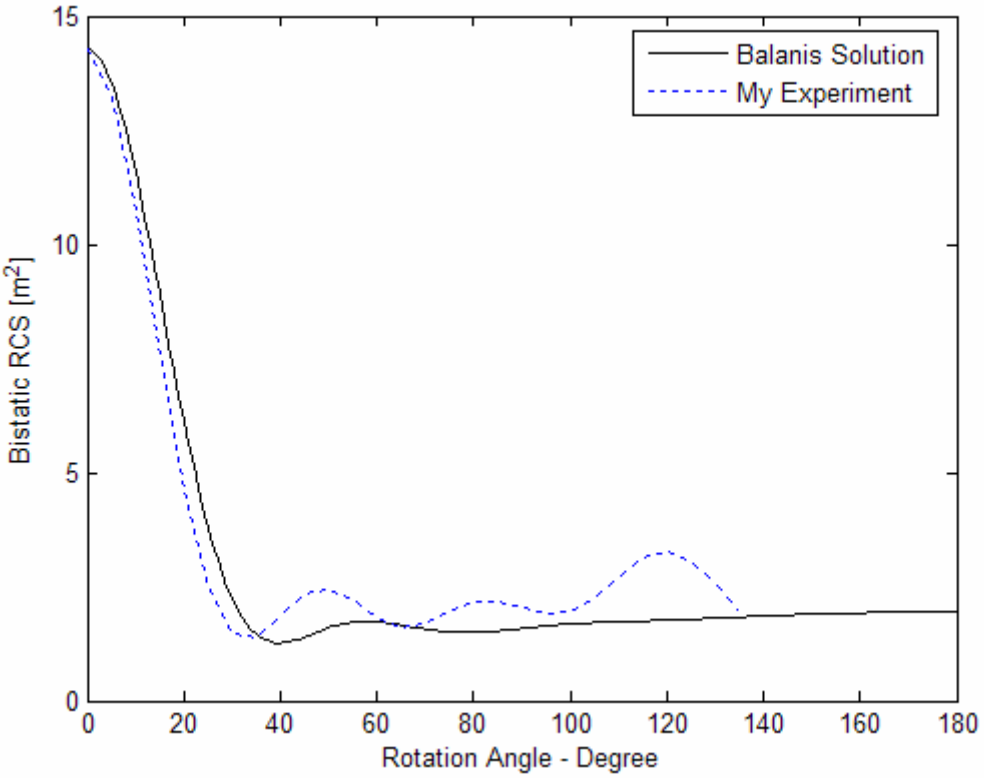

Figure 4.7. Vertical RCS of conducting cylinder at 3 GHz

The theoretical result for RCS of perfectly conducting cylinder is obtained by using Balanis's solution given in [11]. Figure 4.7 shows a comparison between theoretical and

experimental RCS result of perfectly conducting cylinder for vertical polarization at 3 GHz. At angles of nadir the location of the nulls predicted by theory are in good agreement between theory and measurement. The main differences between theory and measurement are asymmetries present in the data not in the theory. These asymmetries occur due to the measurement environment that is semi-anechoic chamber, and cable interferences.

4.2.3. Dielectric Cylinder

After the conducting models, dielectric models are used to calculate RCS. First model is chosen dielectric hollow cylinder. Measurement was done at 3 GHz for vertical polarization. The object's material is plastic, its radius is 5.3 cm, and thickness is 2.37 mm. Permittivity changing of plastic that was measured in Tübitak-UEAKE is given in Table 4.1.

Table 4.1. Permittivity of plastic at frequencies range from 100 MHz to 1.8 GHz

Frequency	Permittivity
1 MHZ	3.00+0.0140j
10 MHz	2.90+0.0038j
100 MHz	2.84+0.0093j
250 MHz	2.83+0.0232j
500 MHz	2.81+0.0167j
1 GHz	2.79+0.0048j
1.5 GHz	2.77+0.0231j
1.8 GHz	2.70+0.0196j

Figure 4.8 shows the comparison with Richmond solution and my experimental result. Experimental result does not show a good agreement with Richmond solution because plastic is lossy dielectric material. If the frequency rises up, loss rate will also increase in experimental environment. As a result of this, while good agreement was gained for conducting materials, a good result was not obtained for dielectric materials. Moreover, the permittivity of plastic was measured at 1.8 GHz but experimental result was

obtaine at 3 GHz. These are important reasons why my experimental result is incompatible with Richmond's solution.

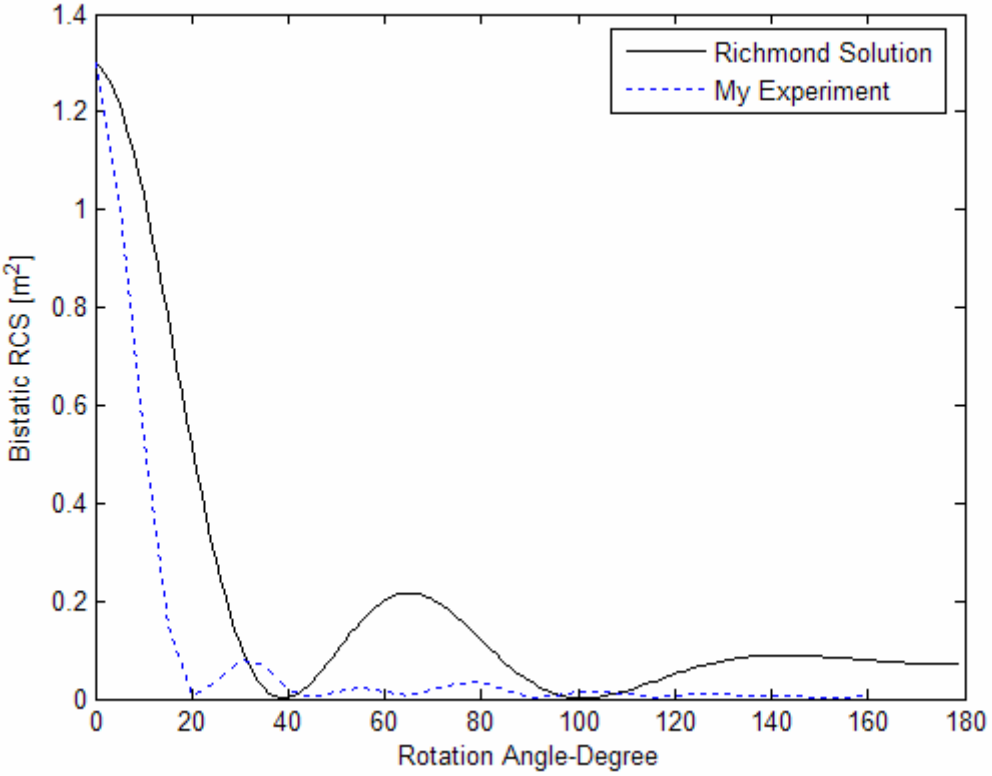

Figure 4.8. RCS of dielectric hollow cylinder for vertical polarization at 3 GHz

4.3. Radar Cross Section Simulation with Ansoft HFSS

Ansoft HFSS is an interactive software package for calculating the electromagnetic behavior of a structure. The software includes post-processing commands for analyzing this behavior in detail [19].

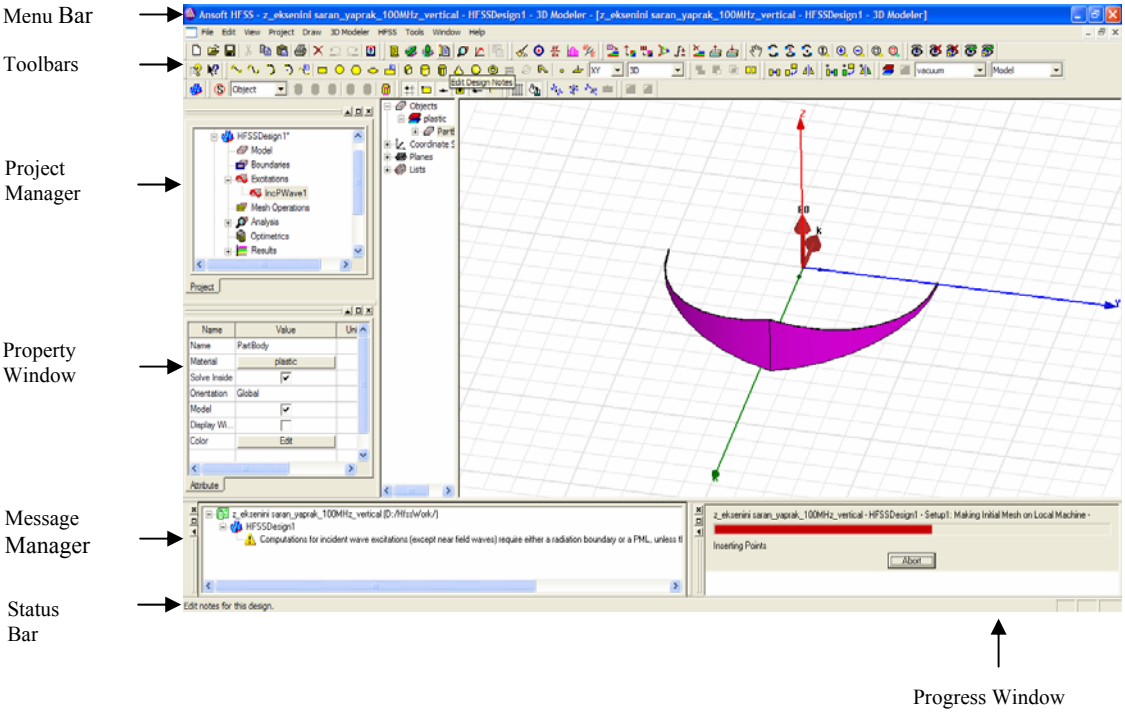

Figure 4.9. HFSS desktop consist of several windows

Ansoft HFSS employs the Finite Element Method (FEM), adaptive meshing, and brilliant graphics to give unparalleled performance and insight to all of 3D EM problems. Ansoft HFSS can be used to calculate parameters such as S-parameters, Resonant Frequency, and Fields. Typical uses include basic electromagnetic field quantities and for open boundary problems, radiated near and far fields; characteristic port impedances and propagation constants; generalized S-parameters and S-parameters renormalized to specific port impedances; the eigenmodes, or resonances of a structure. It is also used to compute Radar Cross Section (RCS) [19].

Basic mesh element of HFSS is a tetrahedron. This allows solving arbitrary 3D geometry, particularly those with complex curves and shapes, in a fraction of the time it would take using other techniques. The value of a vector field quantity (such as the H-field or E-field) at points inside each tetrahedron is interpolated from the vertices of the tetrahedron. At each vertex, HFSS stores the components of the field that are tangential to the three edges of the tetrahedron. In addition, HFSS can store the component of the vector field at the midpoint of selected edges that is tangential to a face and normal to the edge as shown Figure 4.10. The field inside each tetrahedron is interpolated from these nodal values [19].

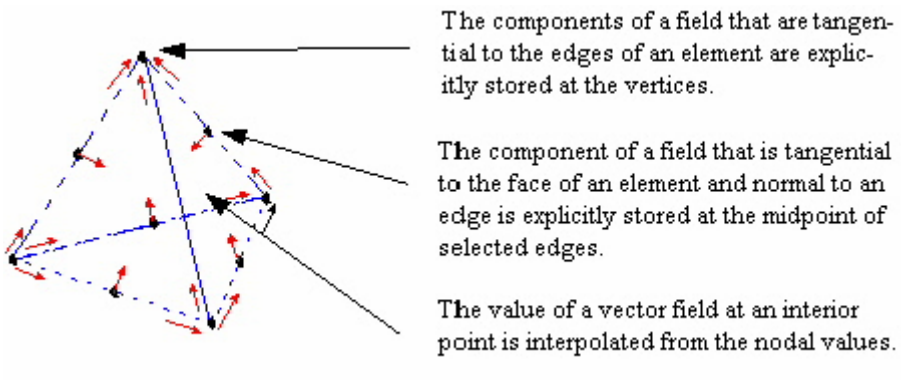

Figure 4.10. Representation of a field quantity

In this thesis, High Frequency Structure Simulator Version 10 (HFSS) was used to calculate Radar Cross Section of simple and arbitrary shapes. The usage of simulator is given step by step as follows [19].

Drawing is the first step of every simulation packages. You can draw one, two, three dimensional objects using the Draw commands. Ansoft HFSS v.10 has its drawing tool. It also has the ability to share the models with other drawing packages. In this thesis, CATIA drawing package is used to draw arbitrary shapes and they are saved as step format [19].

After the model has been generated by using the drawing tool or by importing from drawing package, the next step is to assign physical properties of model. Ansoft HFSS provides a material library, which contains typical metals and dielectric materials. If required material is not on the list, it can be added by putting its parameters. Anisotropic material and nonlinear material can also be added [19].

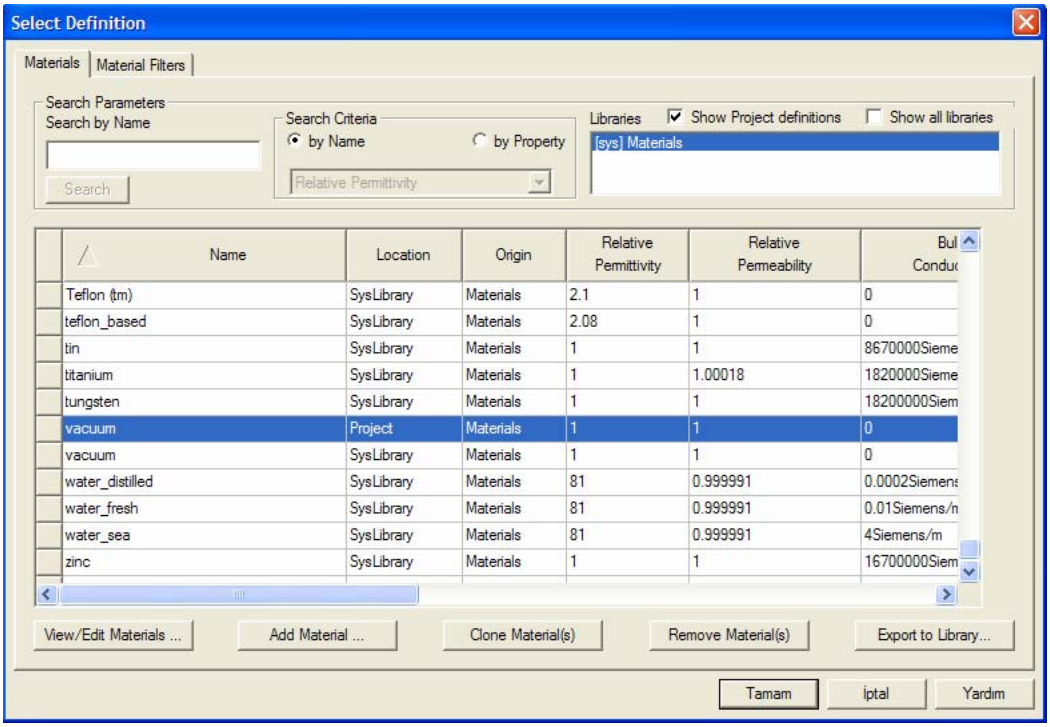

Figure 4.11. HFSS material setup window

Another step is setting radiation. Incident wave is used in a scattering problem. Incident wave is defined by its propagation vector and its magnitude. To obtain bi-static radar cross-section, the boundary of the workspace must be set to radiation boundary. Radiation boundary is used for terminating the workspace in scattering problem. The tangential component of electric and magnetic fields on the surface of the workspace will be used for computing far field by using equivalence principle. Radiation box is used for this termination. This box must have a minimum distance to the closest scattering object of one fourth of the wavelength [19].

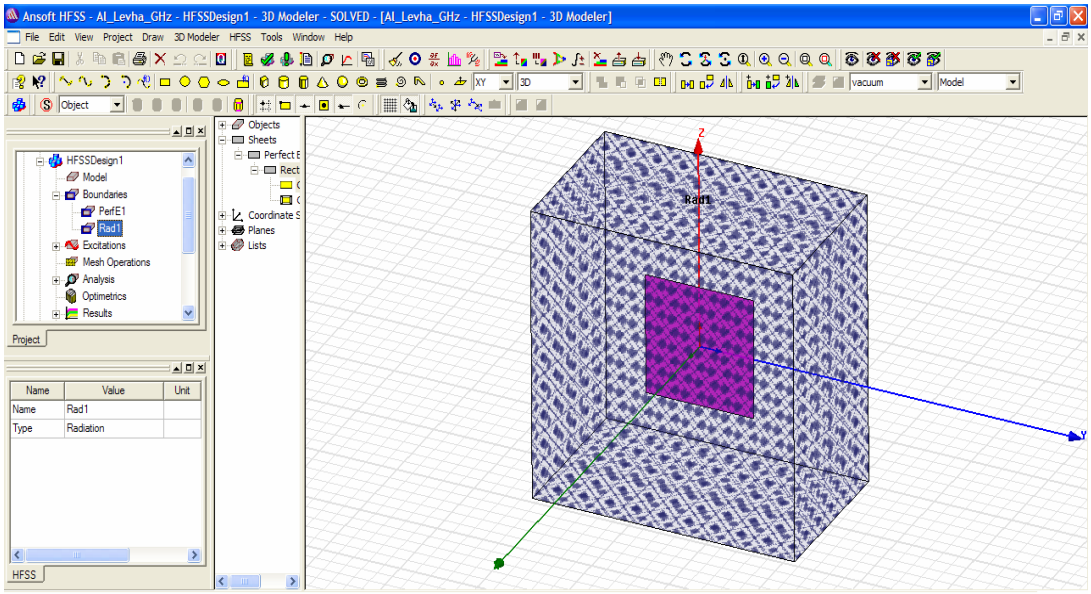

Figure 4.12. HFSS radiation boundary

HFSS has all information of the problem at this point. It is ready to solve the Maxwell's equations. HFSS will compute a solution by adding a solution setup to design. Each solution setup includes the following information, general data about the solution's generation, adaptive mesh refinement parameters, and frequency sweep parameters [19].

The interested frequency band must be given before HFSS can start solving the problem. The picture below shows HFSS Solution Setup Windows. In General tab, solution frequency is entered, and in Options tab, adaptive analysis can be performed by entering two or more passes in the Maximum number of passes box [19].

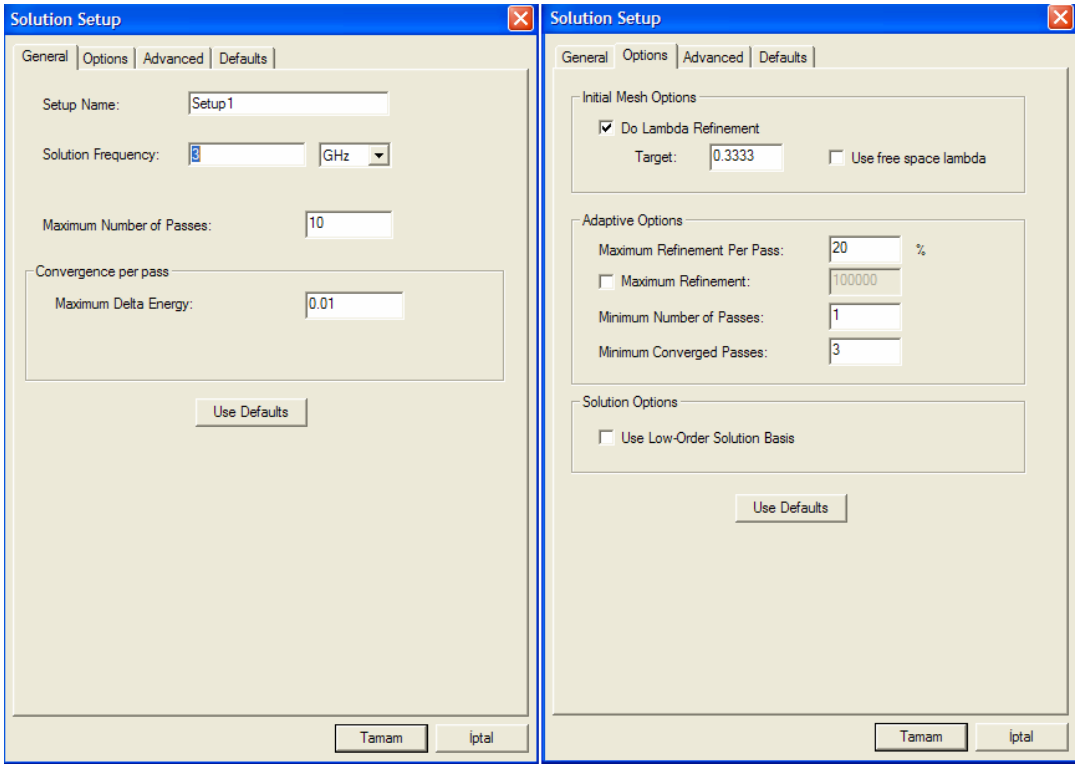

Figure 4.13. HFSS solution setup window

In literature, some examples can be found about the usage of HFSS. First example is that Wei, Li, and Zhang improved Finite element – Fast multiple method (FEM-FMM) to calculate bistatic RCS and they gained results by using HFSS to verify the performance of the improved FEM-FMM method [19]. Their scatterer is a finite three by three microstrip array mounted on a two-layer substitute. The upper layer in which the patches are embedded has the thickness of 0.03048λ, and is filled using G10 with $\varepsilon_{r1} = 3.8 - j0.01482$ and $\mu_{r1} = 1$. The lower layer on the top of the finite ground plane has the thickness of 0.015748λ, and is filled using Duroid 5880 with $\varepsilon_{r2} = 2.22 - j0.001998$ and $\mu_{r2} = 1$. The size of each patch is $0.732\lambda \times 0.52\lambda$. The size of the finite ground plane is $3.396\lambda \times 2.76\lambda$. The distance between each patch is 0.3λ. Figure 4.14 shows the bistatic RCS of this array in the y-z plane for a plane wave incident along −z-axis with the y-polarized electric field. The result using the Ansoft HFSS software is also shown in Figure 4.14 for the verification. The agreement between these three results is good [20].

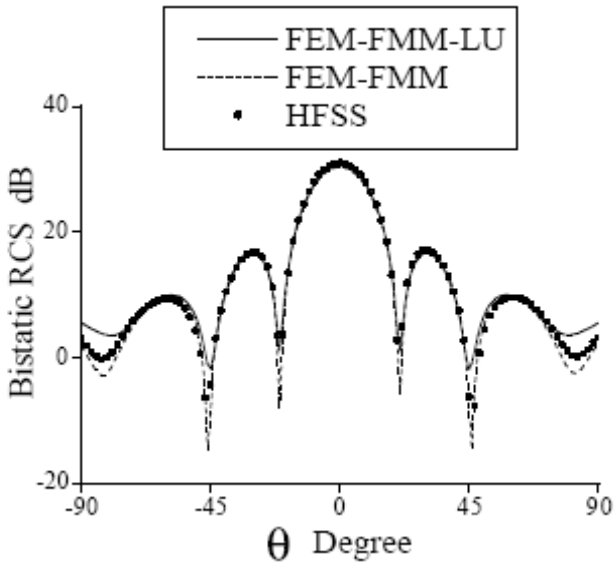

Figure 4.14. RCS of the three by three microstrip array in yz plane

Unfortunately all measurements were not completed due to laboratory problems. So, RCS of simple shapes were also gained by using simulator program (HFSS). The same models were used to calculate RCS by using HFSS and the results were again compared with theoretical results.

4.3.1. RCS of Conducting Rectangular Flat Plate

Same model given in Section 4.2.1 is used to calculate monostatic RCS with Ansoft HFSS. The target placed on coordinating system is illustrated in Figure 4.15 by showing incident wave's direction.

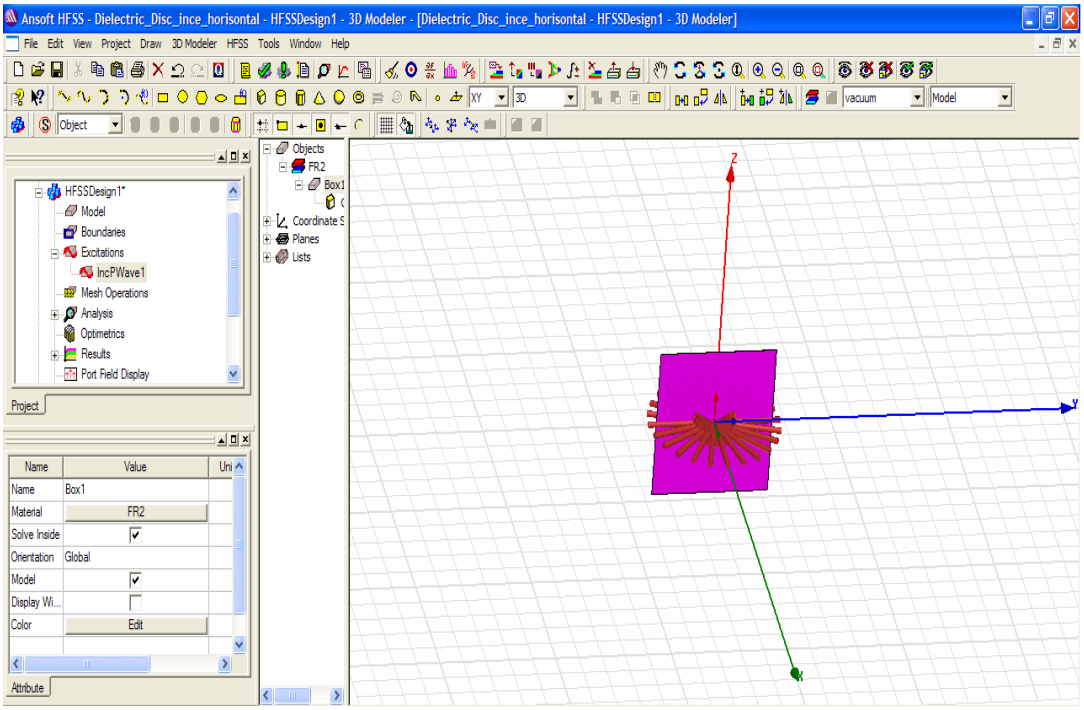

Figure 4.15. Conducting rectangular flat plate

Figure 4.16 and 4.17 show vertical and horizontal RCS of conducting flat plate, respectively. Both theoretical and simulation results were done at 3 GHz.

Figure 4.16 and Figure 4.17 illustrate a comparison between theoretical and simulation result of monostatic RCS of flat plate at 3 GHz for vertical and horizontal polarization, respectively. A perfect agreement behavior is seen between Ross solution and HFSS result.

Figure 4.16 and 4.17 show vertical and horizontal RCS of conducting flat plate, respectively. Both theoretical and simulation results were done at 3 GHz.

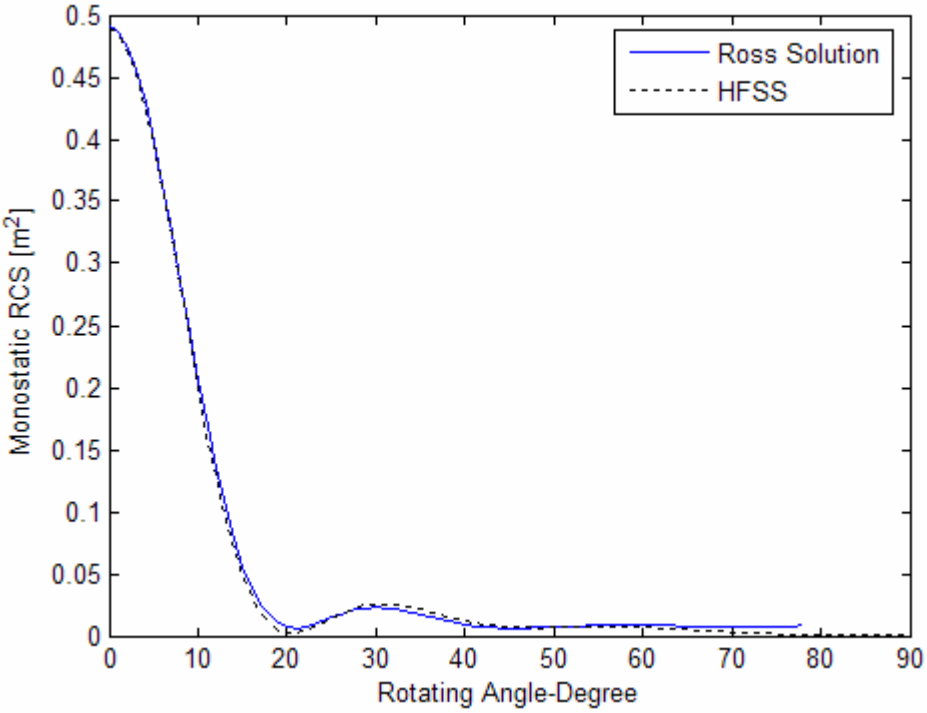

Figure 4.16. Vertical RCS of rectangular flat plate at 3 GHz

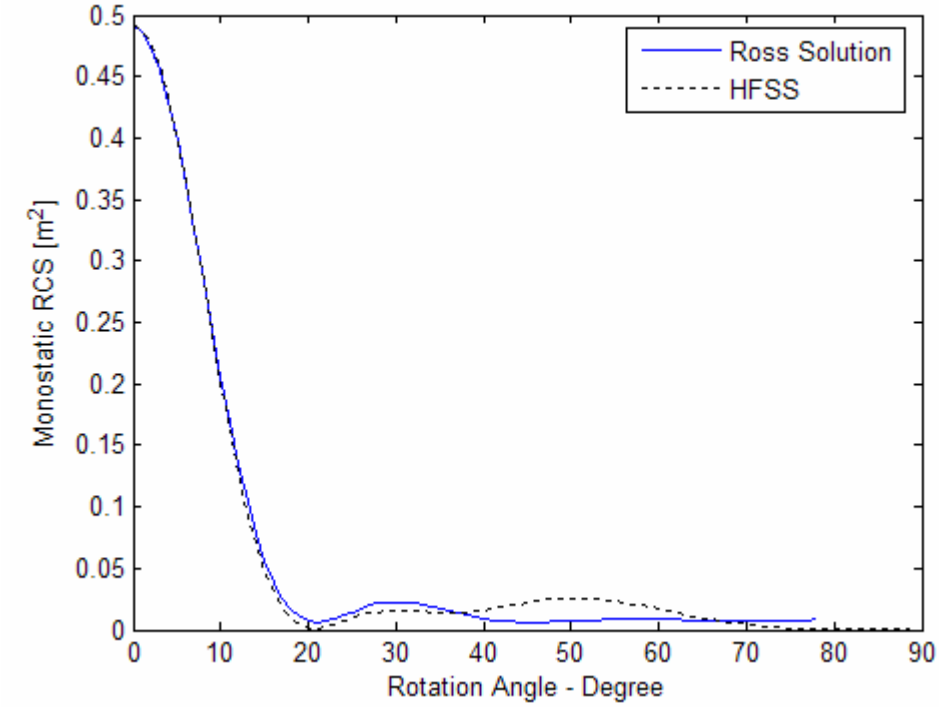

Figure 4.17. Horizontal RCS of rectangular flat plate at 3 GHz

4.3.2. RCS of Perfectly Conducting Cylinder

Conducting cylinder whose features given in Section 4.2.2 is shown in Figure 4.18. Bi-static RCS of cylinder was calculated at 3 GHz both vertical and horizontal polarizations. Figure 4.18 and Figure 4.19 show comparison between theoretical and HFSS results for vertical and horizontal polarizations, respectively.

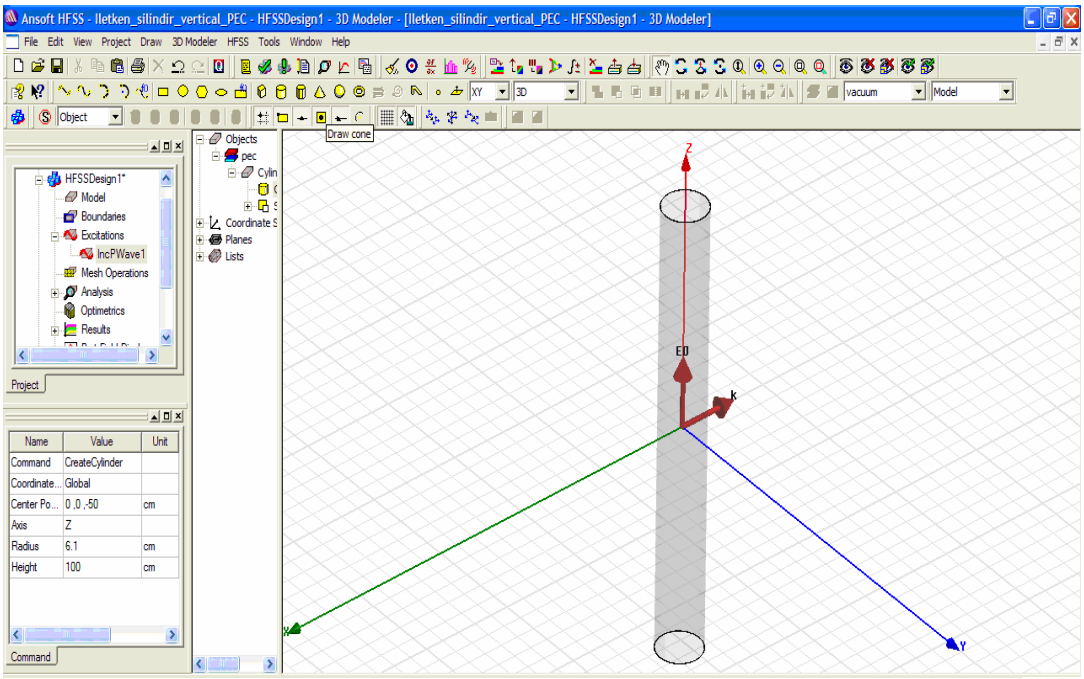

Figure 4.18. Perfectly conducting cylinder

It is seen as in Figure 4.19 and Figure 4.20, the results obtained with HFSS are compatible with Balanis's solution.

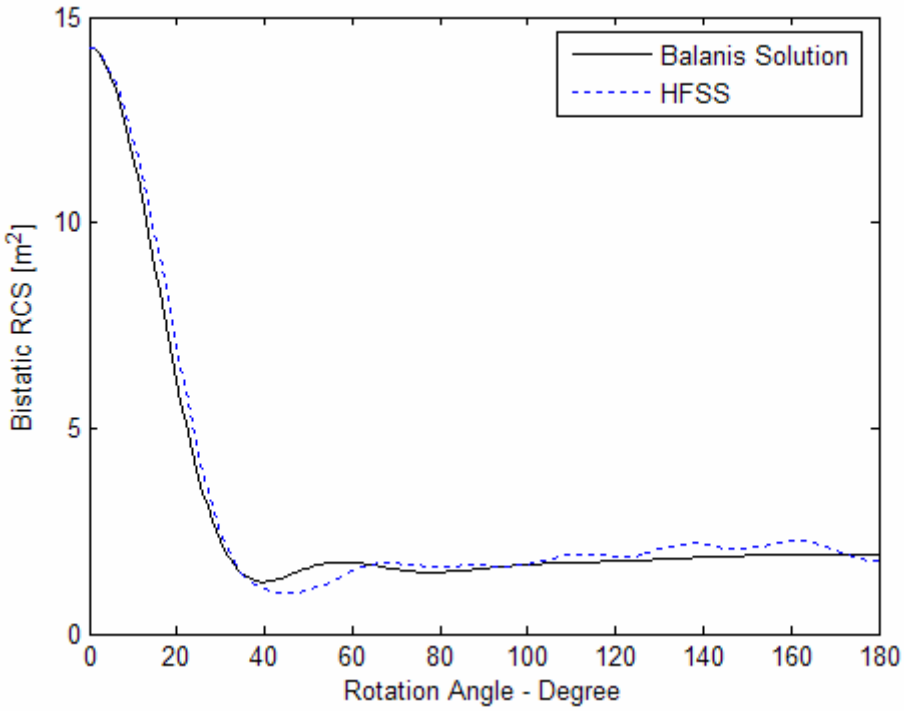

Figure 4.19. Vertical RCS of conducting cylinder at 3 GHz

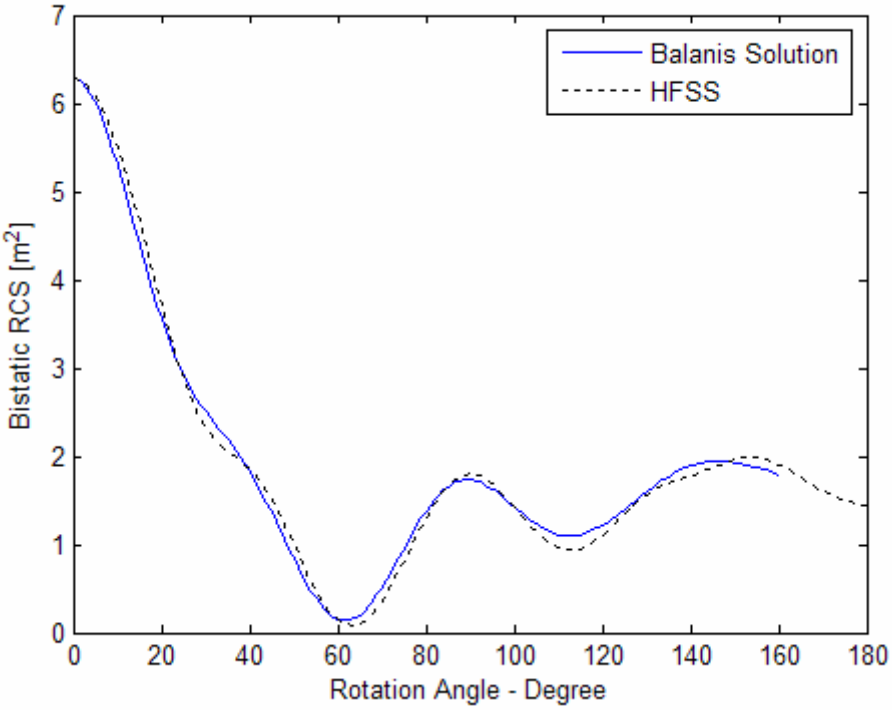

Figure 4.20. Horizontal RCS of conducting cylinder at 3 GHz

4.3.3. RCS of Dielectric Rectangular Disc

Another simple shape was chosen as dielectric disc whose material is FR2- Flame Resistant2 in order to calculate mono-static RCS. Its dimensions are 10x10 cm and thickness is 0.0106 cm. The permittivity change of FR2 is given in Table 4.2. Simulation result was compared with Le Vine's solution given in [12].

Table 4.2. Permittivity of FR2 at frequencies range from 1 MHz to 1.8 GHz

Frequency	Permittivity
1 MHZ	4.70+0.254j
10 MHz	4.40+0.156j
100 MHz	4.07+0.178j
250 MHz	3.90+0.187j
500 MHz	3.82+0.170j
1 GHz	3.70+0.160j
1.5 GHz	3.68+0.170j
1.8 GHz	3.60+0.147j

A comparison between theoretical and HFSS result of RCS of dielectric disc for vertical and horizontal polarization is illustrated in Figure 4.21 and Figure 4.22, respectively. Simulations were done at 3 GHz.

As seen in Figure 4.21 and Figure 4.22, similar results are obtained for both vertical and horizontal polarizations. It is also seen a good agreement behavior between simulation and Le Vine's solution. The differences between simulation and theory are also seen because different methods are used by simulator and Le Vine's approximation. Furthermore, simulator completed the RCS calculations with %5 error rate.

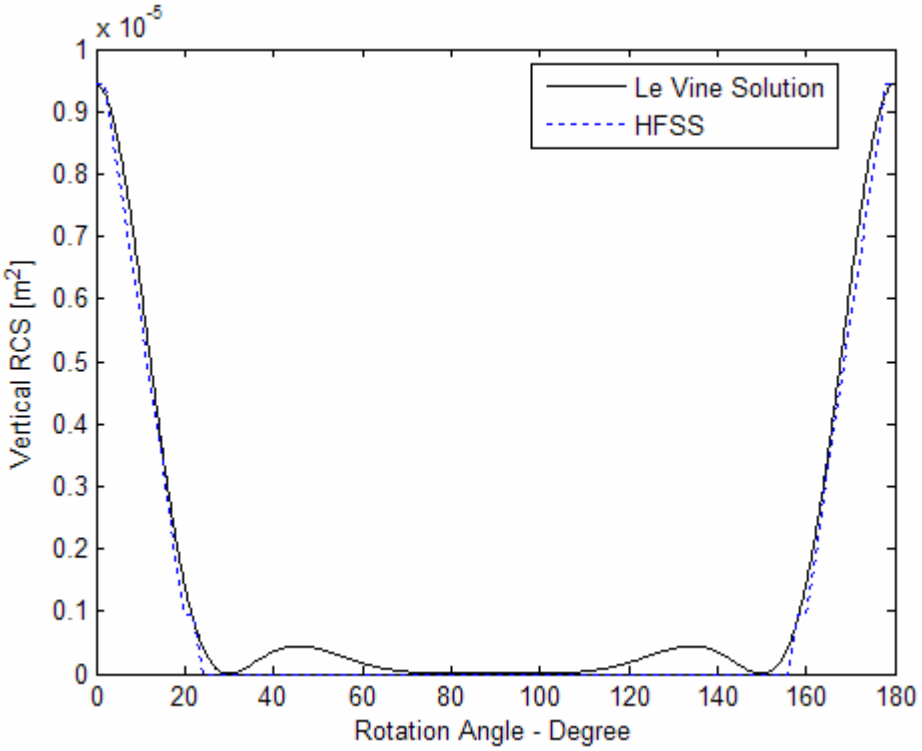

Figure 4.21. Vertical RCS of dielectric disc at 3 GHz

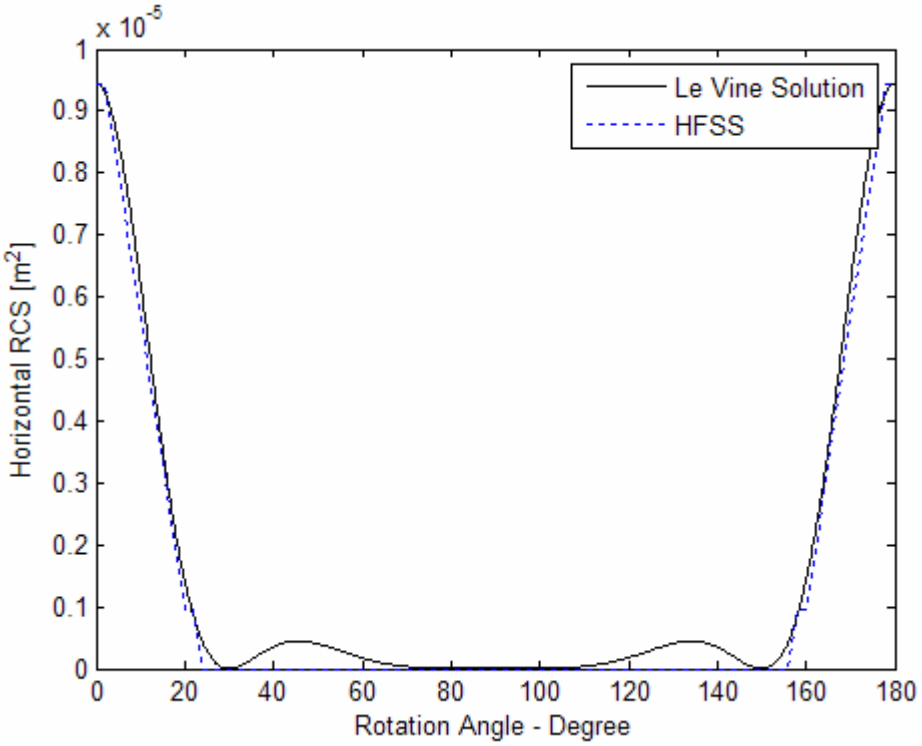

Figure 4.22. Horizontal RCS of dielectric disc at 3 GHz

4.3.4. RCS of Dielectric Cylinder

Last simple shape is dielectric cylinder whose features were given in Section 4.2.3. Figure 4.23 shows dielectric cylinder located at coordinate system for horizontal polarization.

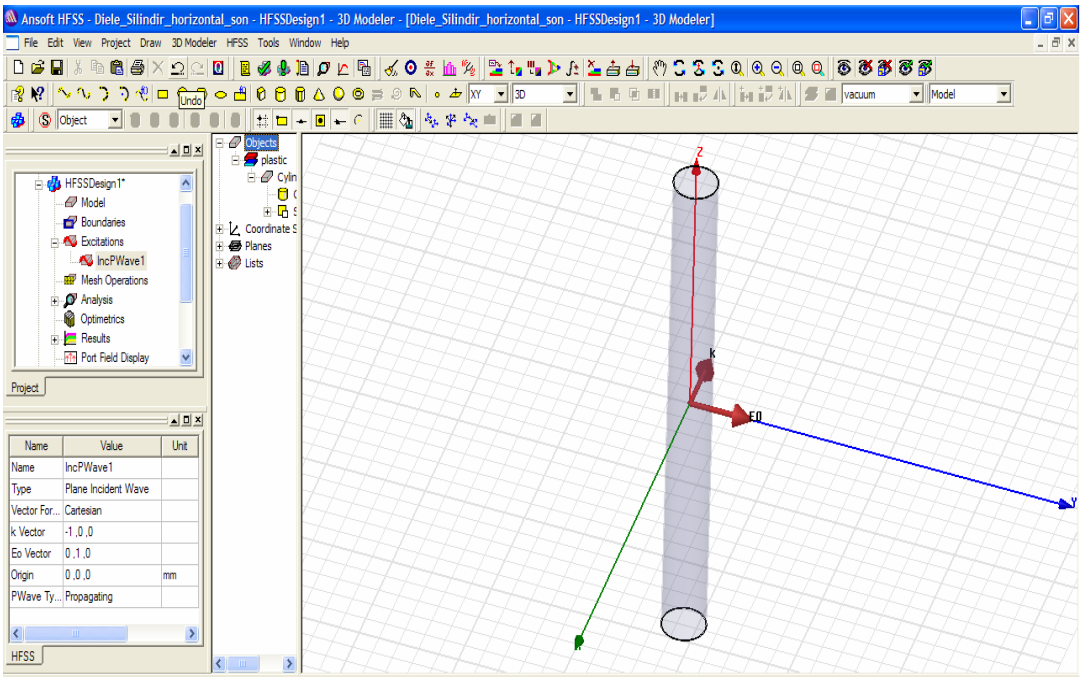

Figure 4.23. Simulation of dielectric cylinder for horizontal polarization

In Figure 4.24 and 4.25, HFSS result was compared with Richmond solution [18] and Discretization method given in [14]. As seen these figures, a good agreement is obtained between HFSS result, Discretization solution and Richmond solution.

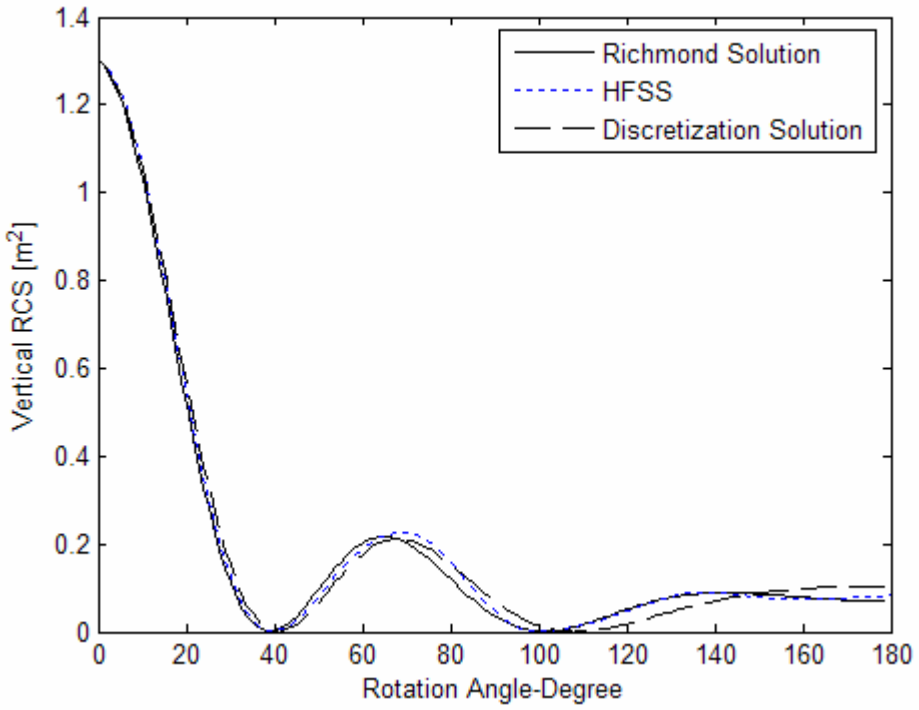

Figure 4.24. Vertical RCS of dielectric cylinder at 3 GHz

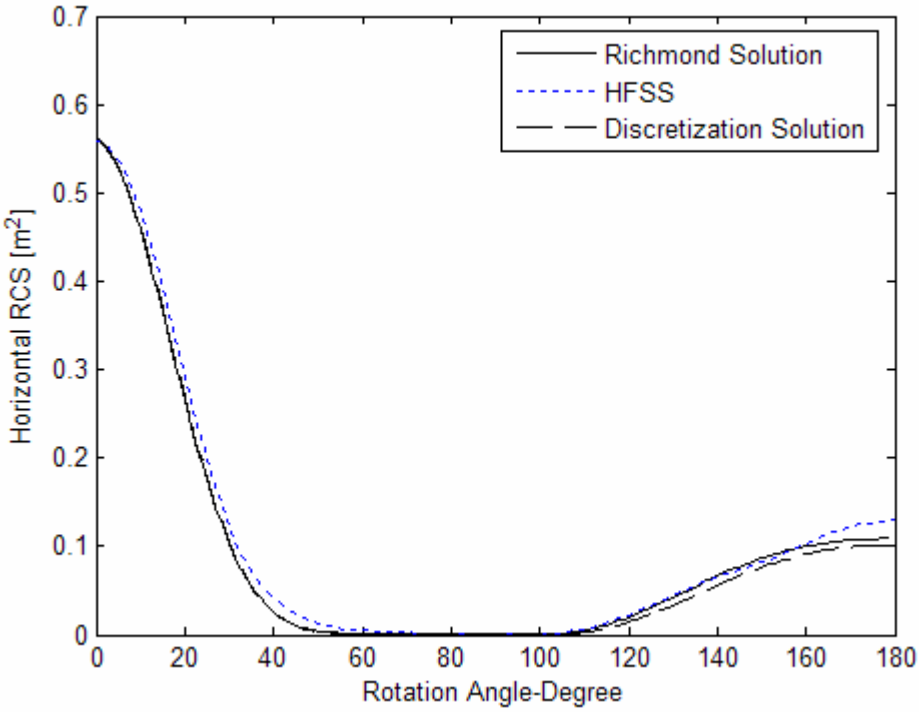

Figure 4.25. Horizontal RCS of dielectric cylinder at 3 GHz

In Discretization Method, small sized dielectric sheets, given in Figure 2.19, are added to each other one by one, and consequently a discretized shell, illustrated in Figure 4.26, is obtained. In addition, the essence of discretization method is presented in Figure 4.26. Quasi-Static approximation is used in this method [14].

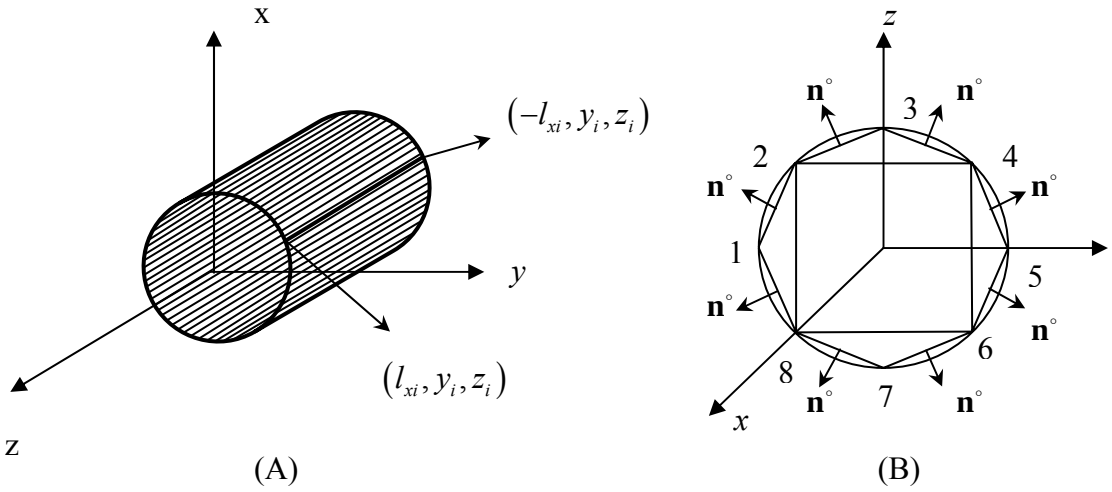

Figure 4.26. Discretized cylinder shell and Discretization Method

A hollow cylinder is assumed that three layered small dielectric sheets consisting of air-dielectric material-air are added to each other and finally, they form a three layered cylinder (air-dielectric material-air) [14].

4.3.5. RCS of Three-Layered Cylinder

Another simple shape will be selected as multilayer cylinder with three different materials instead of single layer cylinder to verify Discretization Solution. The thickness of each layer of the multilayer cylinder is chosen as 1 mm. The frequency is taken as 100 MHz. Figure 4.27 shows multilayer cylinder consisting of three different dielectric materials whose radius is 1.5 m for $k\,a = \pi$ and its length is 1 m. Figure 4.28 and Figure 4.29 show horizontal and vertical radar cross section, respectively. The permittivities of each layer are 4-0.4j, 3-0.3j, 2-0.2j from inner to outer.

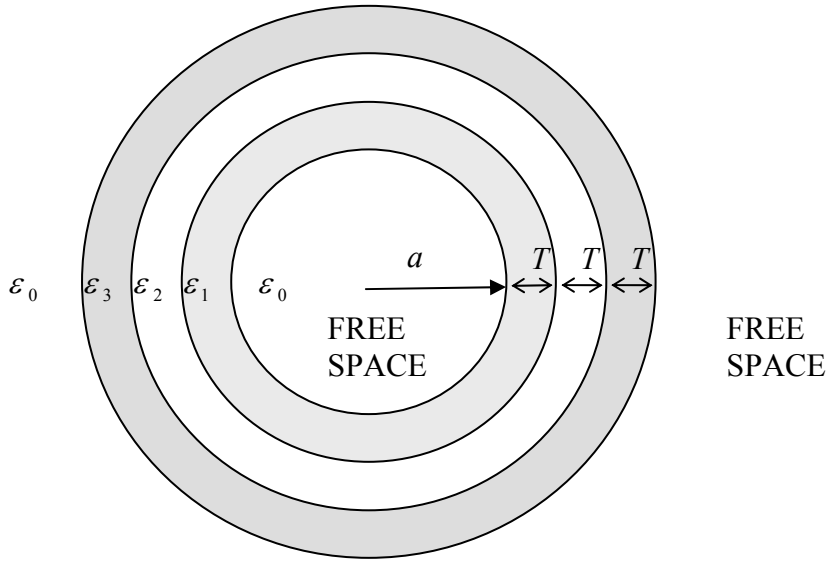

Figure 4.27. Multilayer cylinder consisting of three different dielectric materials

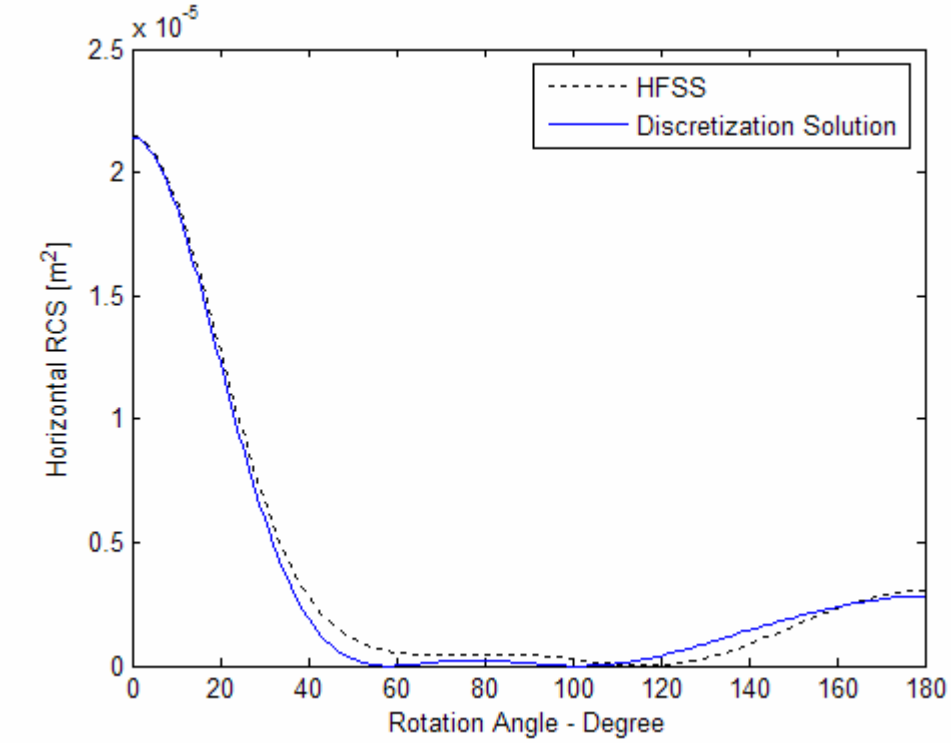

Figure 4.28. Horizontal RCS of multilayer cylinder at 100 MHz

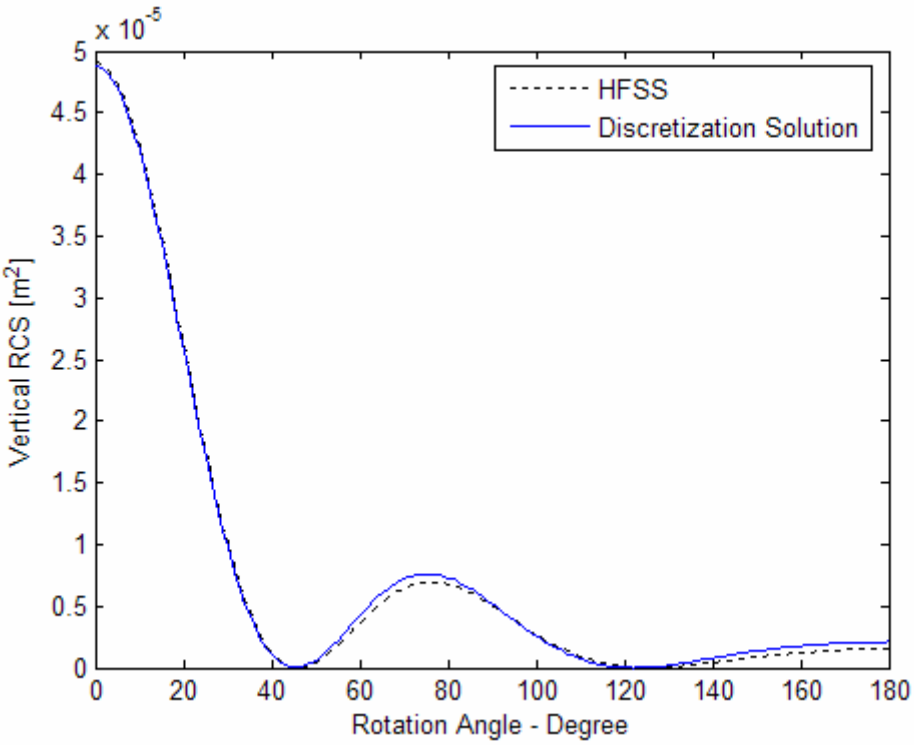

Figure 4.29. Vertical RCS of multilayer cylinder at 100 MHz

The simulation is also obtained at high frequency. For this case same parameters are used except that the frequency is increased to 1 GHz and the cylinder radius is decreased to 15 cm so that $k\,a$ remains the same. The results are shown in Figure 4.30 and 4.31 for horizontal and vertical polarizations, respectively.

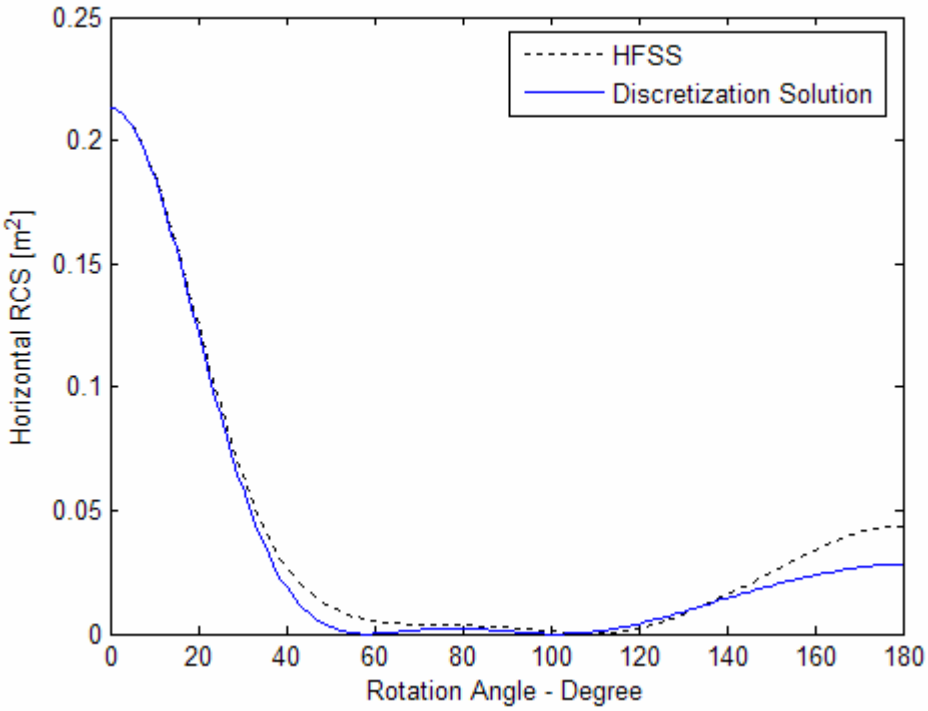

Figure 4.30. Horizontal RCS of multilayer cylinder at 1 GHz

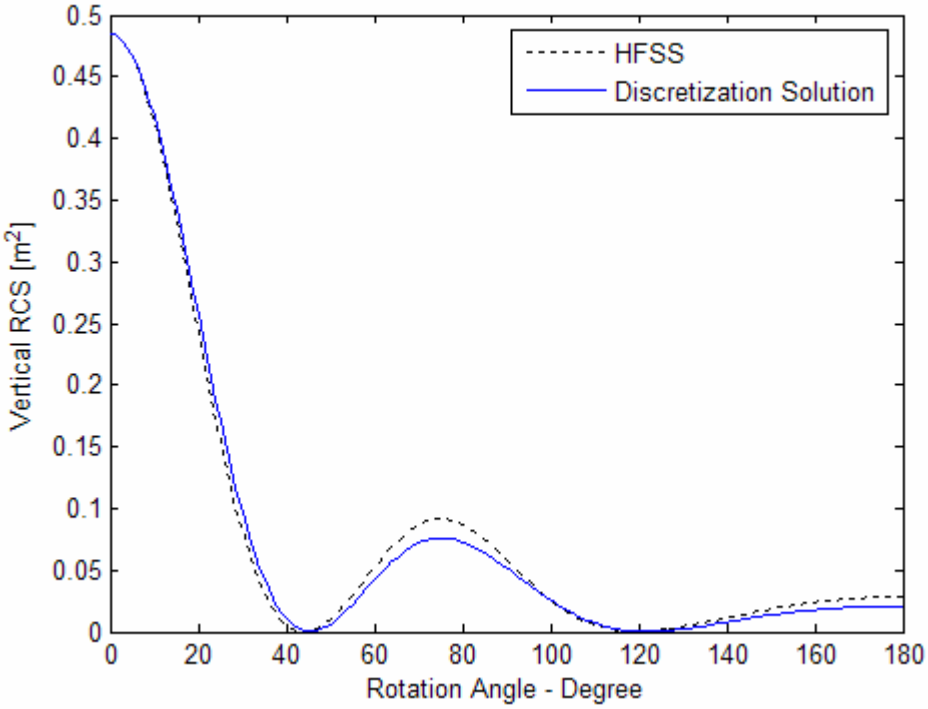

Figure 4.31. Vertical RCS of multilayer cylinder at 1 GHz

RCS of another multilayer cylinder example that was used in [14] is also calculated by HFSS to compare with Discretization Solution. This cylinder's radius is 52 cm, its length is 100 cm and its thickness of each layer is 0.1 mm. The permittivity of layers from outer to inner is 5-5j, 10-20j, and 20-10j. The results are illustrated in Figure 4.32, Figure 4.33, Figure 4.34 and Figure 4.35 at 100 MHz and 1 GHz, respectively.

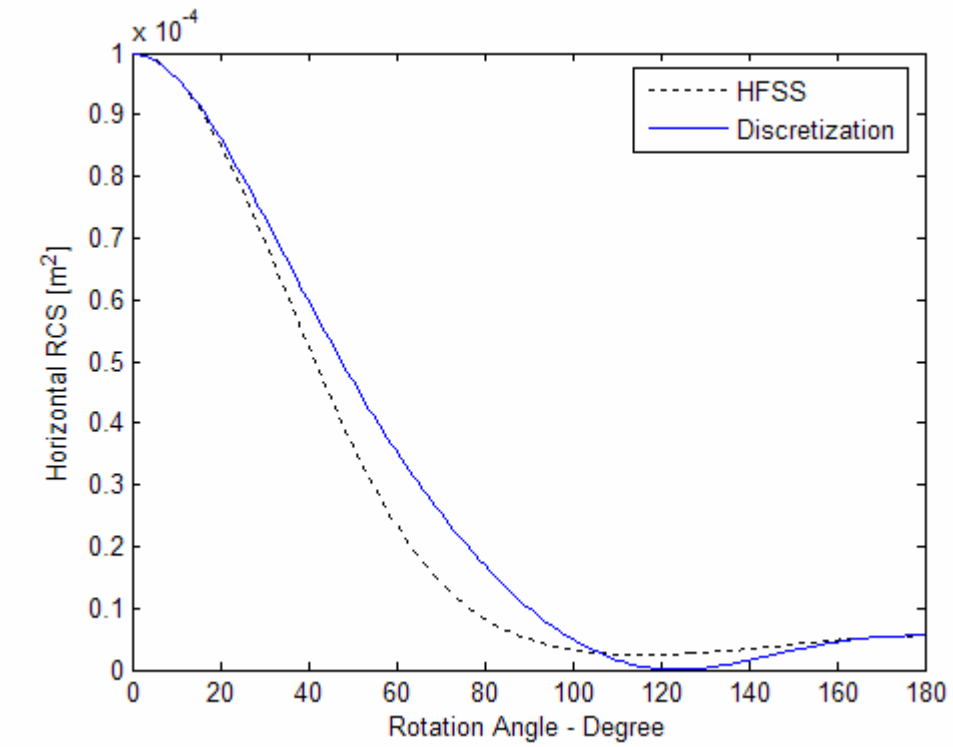

Figure 4.32. Horizontal RCS of multilayer cylinder at 100 MHz

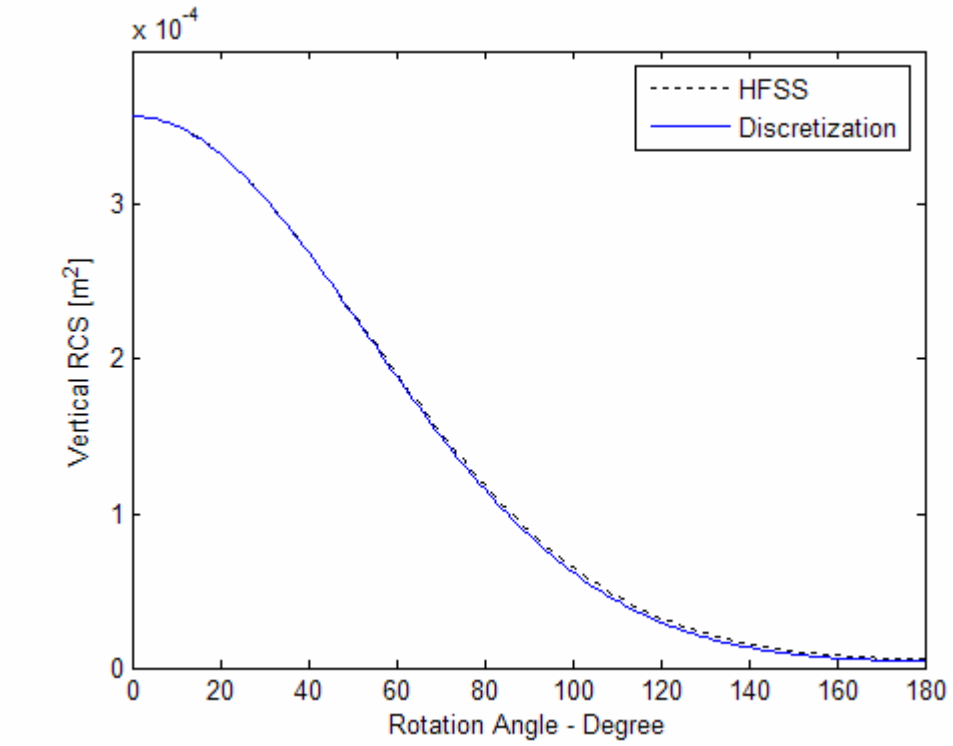

Figure 4.33. Vertical RCS of multilayer cylinder at 100 MHz

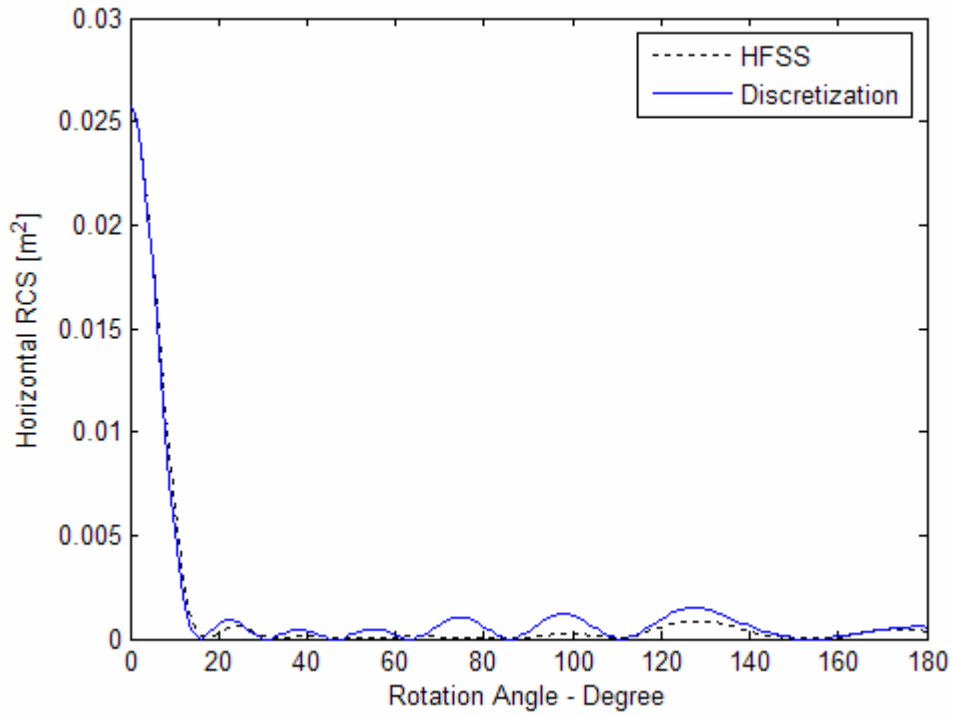

Figure 4.34. Horizontal RCS of multilayer cylinder at 1 GHz

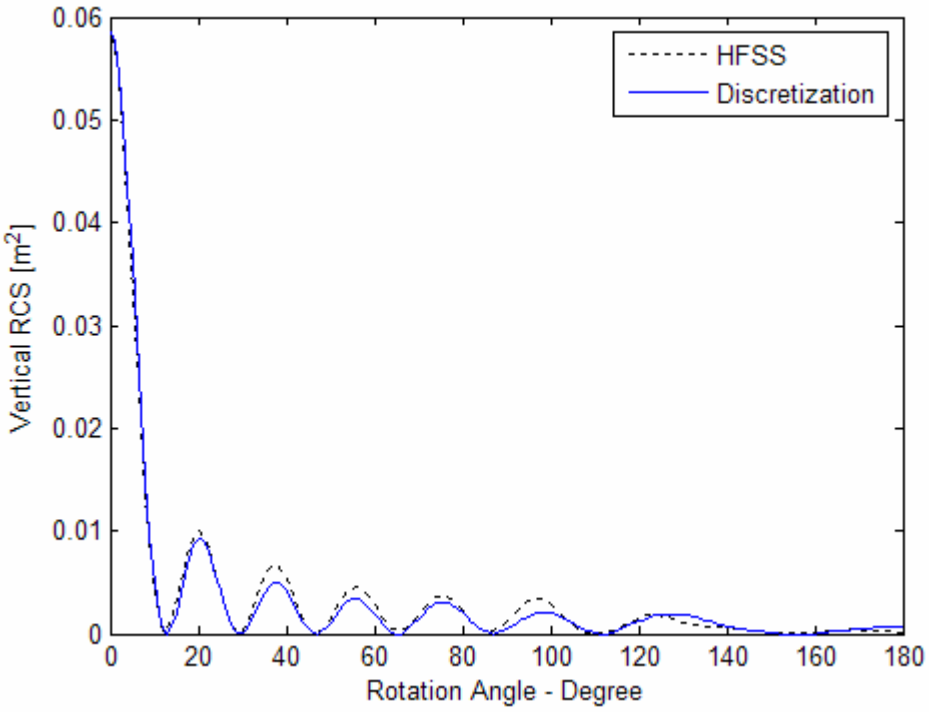

Figure 4.35. Vertical RCS of multilayer cylinder at 1 GHz

5. RADAR CROSS SECTION SIMULATIONS OF ARBITRARY SHAPES

In this part, RCS of arbitrary shapes obtained from dielectric hollow cylinder will be computed to verify Discretization Solution given in [14]. RCS of arbitrary shapes obtained from dielectric single layer hollow cylinder and from three-layered cylinder will be calculated by using HFSS.

5.1. Arbitrary Shaped Object Obtained From Dielectric Hollow Cylinder

Arbitrary shaped object was gained by cutting the cylinder whose features were given in Section 4.3.4 in the direction of length. The geometry of this shape is illustrated in Figure 5.1. The model is vertical to xy plane and it is shown in Figure 5.2. The permittivity of the model is given in Table 5.1. The permittivities are 2.84+0.0093j and 2.79+0.00486j at 100 MHz and 1 GHz, respectively.

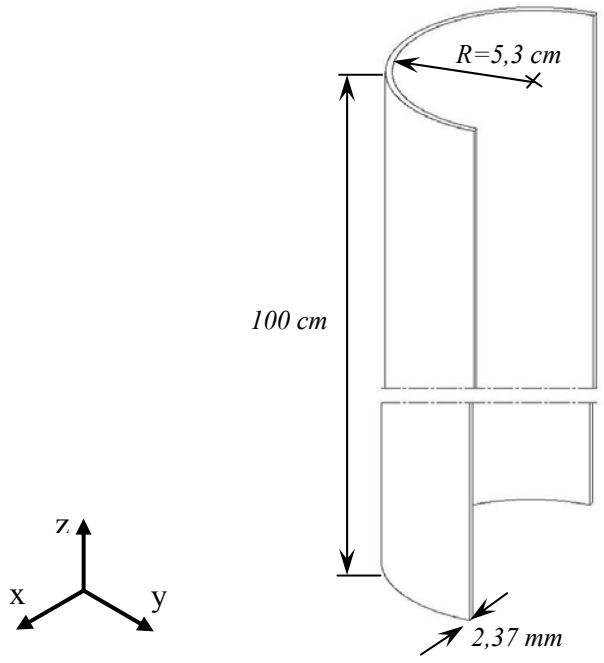

Figure 5.1. The geometry of arbitrary shaped object obtained from hollow cylinder

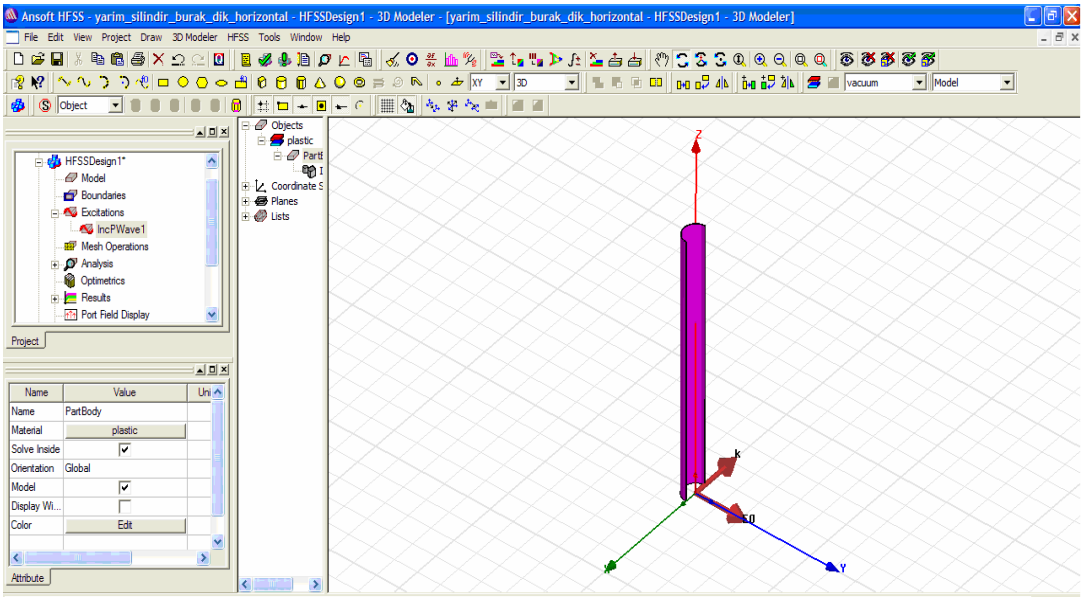

Figure 5.2. Simulation of arbitrary shape for horizontal polarization

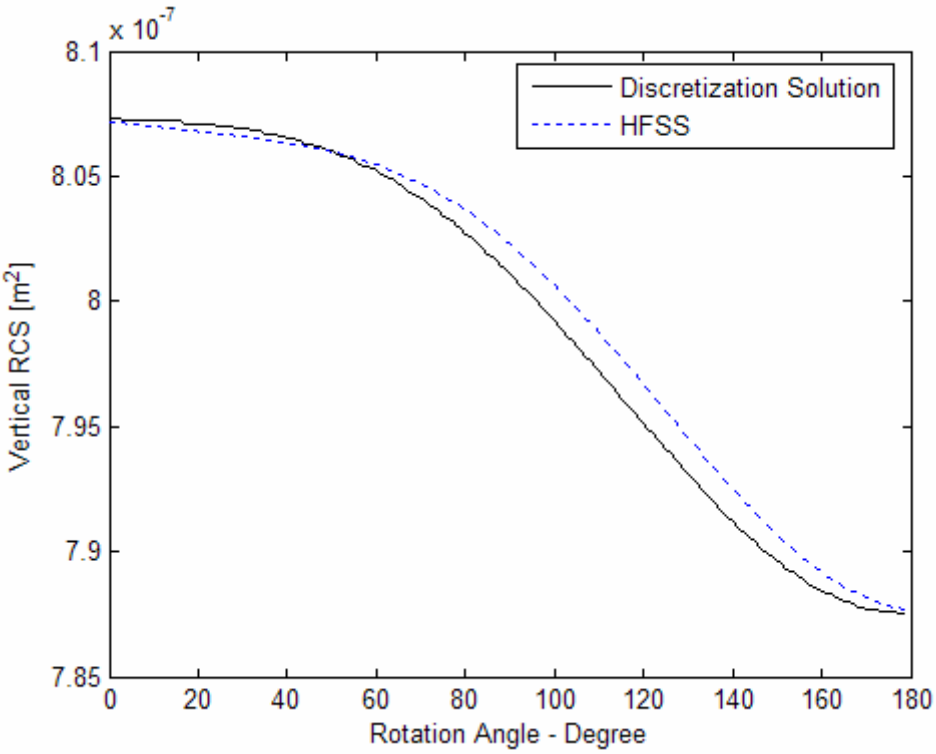

Figure 5.3. Vertical RCS of arbitrary shape at 100 MHz

As seen Figure 5.3 and Figure 5.4, a good agreement behavior is obtained between HFSS results and the Discretization Solution's results for vertical and horizontal polarization at low frequency.

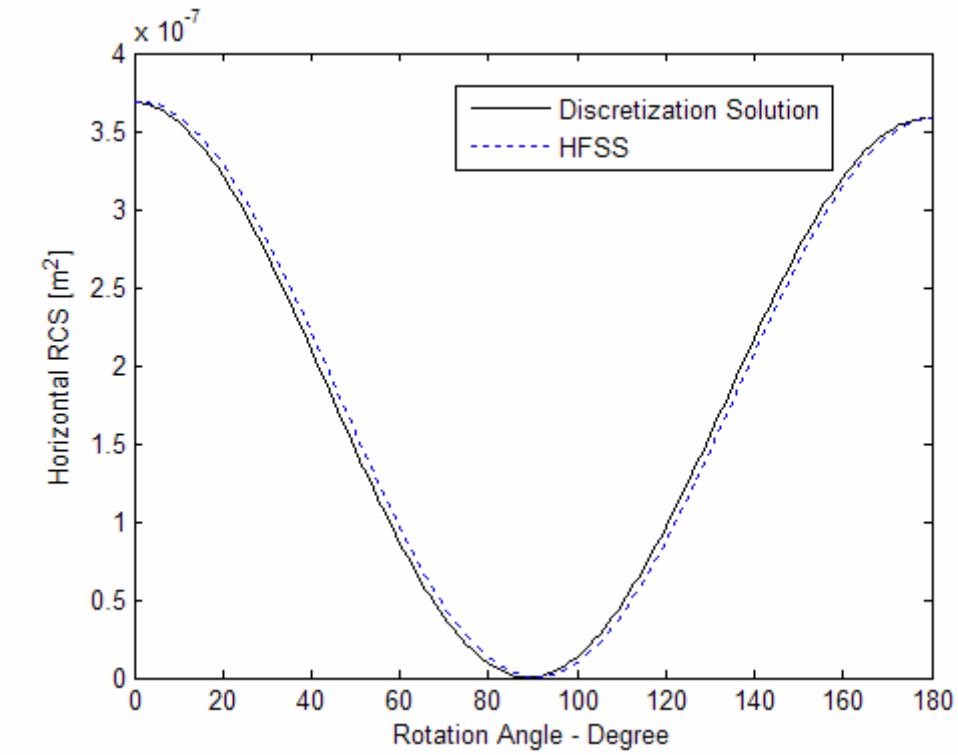

Figure 5.4. Horizontal RCS of arbitrary shape at 100MHz

Furthermore, Radar Cross Section of this object is also calculated for high frequency by using HFSS and Discretization Solution. Figure 5.5 and Figure 5.6 show bi-static RCS of arbitrary shaped object for vertical and horizontal polarization, respectively.

Figure 5.5 and Figure 5.6 illustrate that HFSS result is compatible with Discretization solution at 1 GHz for both vertical and horizontal polarization.

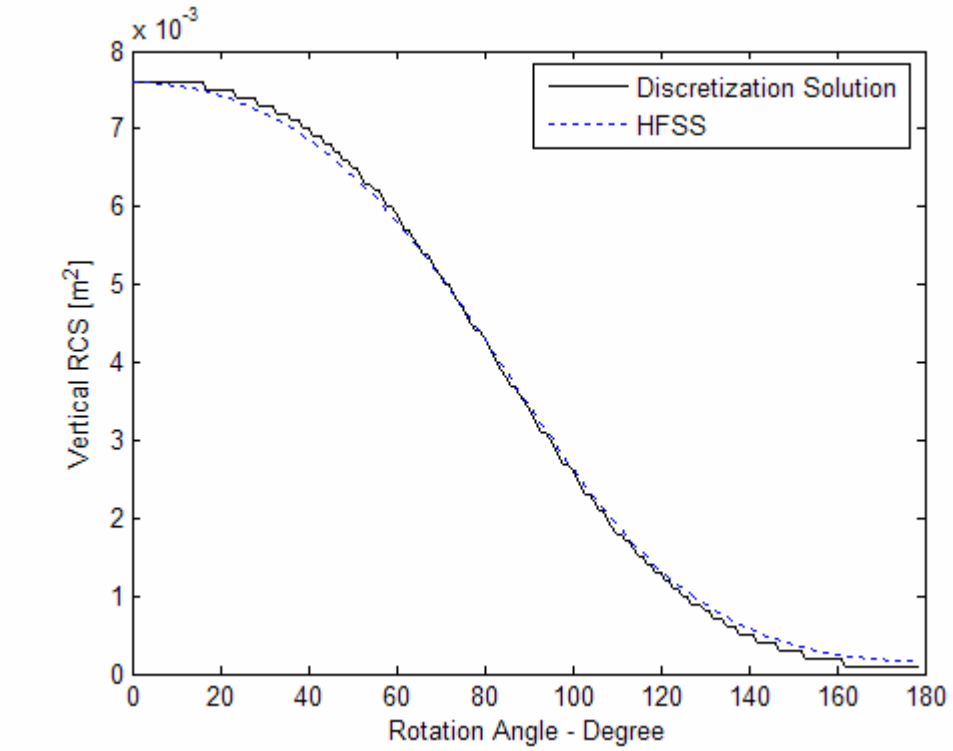

Figure 5.5. Vertical RCS of arbitrary shape at 1 GHz

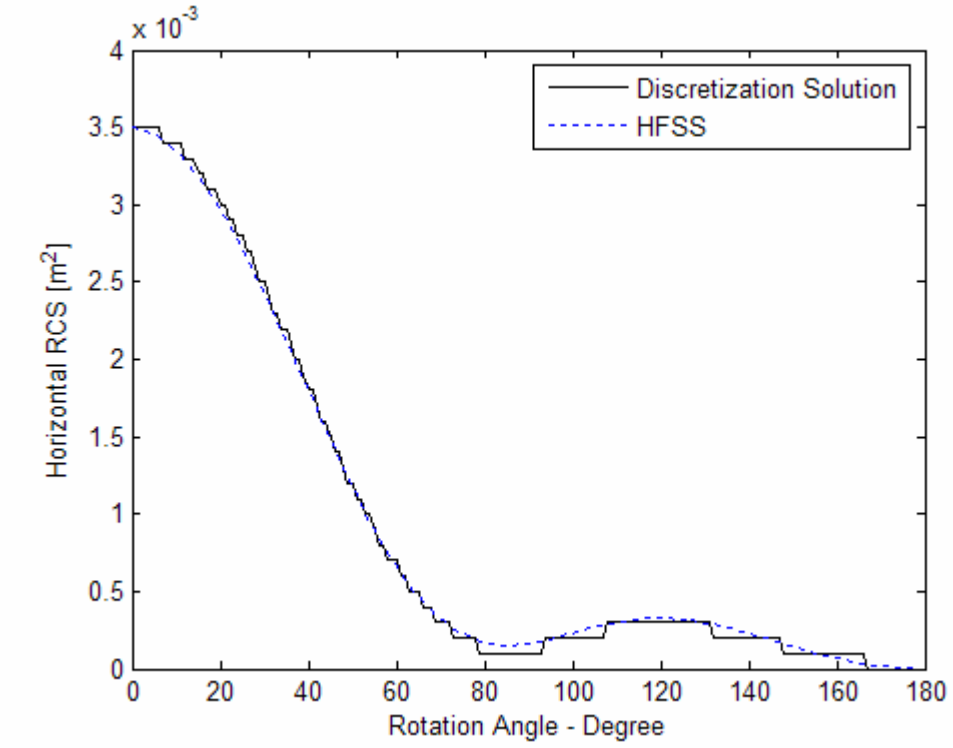

Figure 5.6. Horizontal RCS of arbitrary shape at 1 GHz

Another example given in [14] is also used to compare the results of Discretization Solution with the results of HFSS. The radius of cylinder is 52 cm, its length is 100 cm its thickness is 0.1 mm and the permittivity of it is 29.1-13.3j. The shape is obtained by cutting of this cylinder and the angle of cylinder is $3\pi/4$ instead of 2π. Figure 5.7 shows the arbitrary shaped object. Figure 5.8, Figure 5.9, Figure 5.10 and Figure 5.11 show the RCS of this arbitrary shape at 100 MHz and 1 GHz.

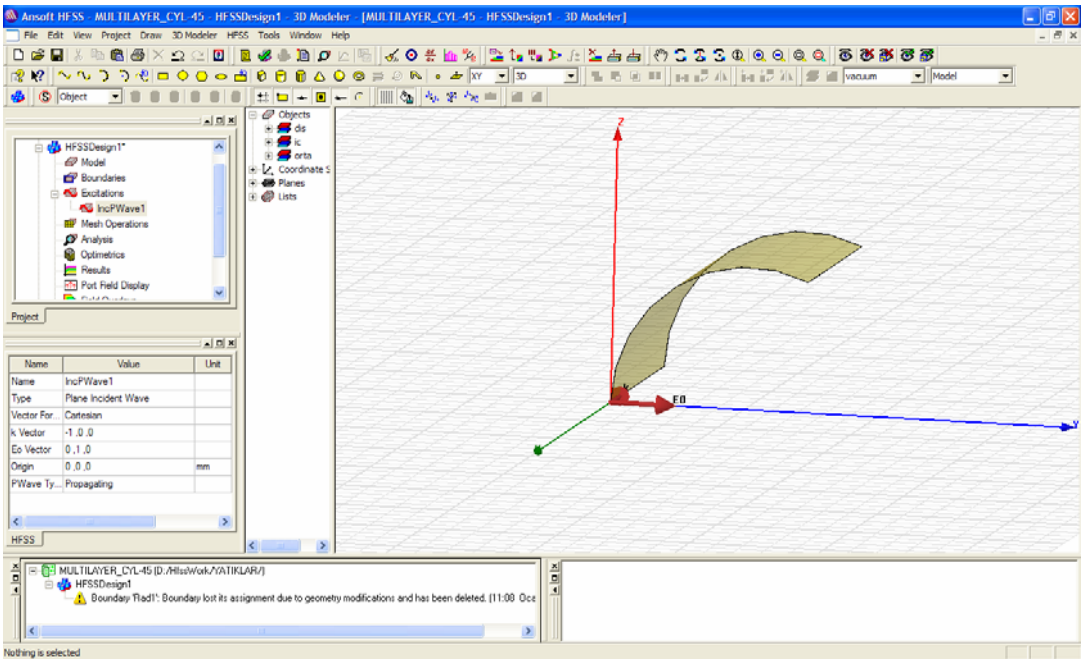

Figure 5.7. Simulation of arbitrary shape for horizontal polarization

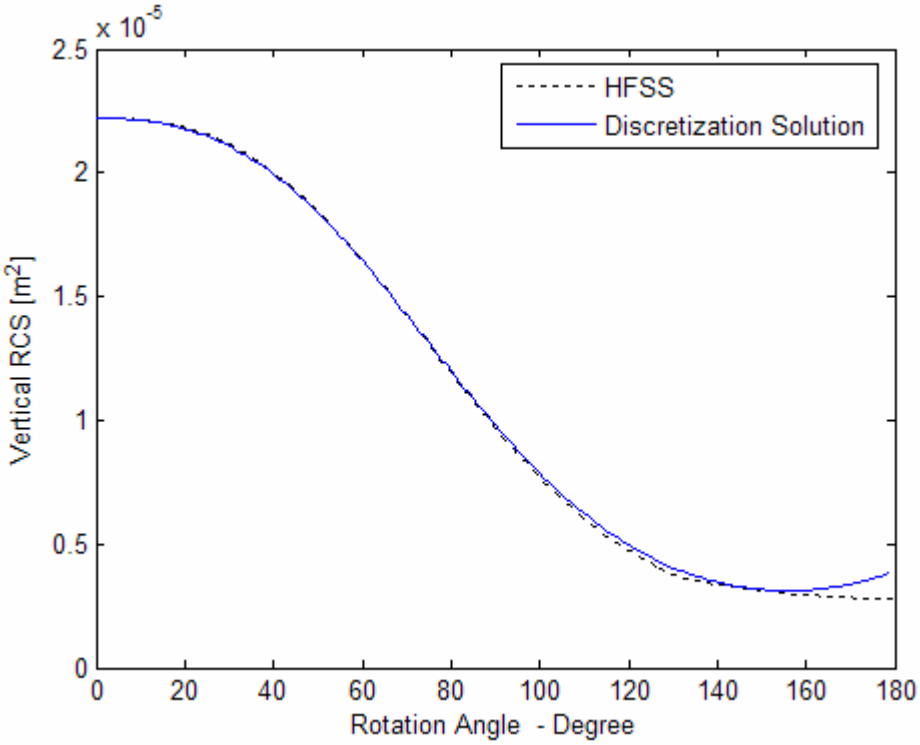

Figure 5.8. Vertical RCS of arbitrary shape at 100 MHz

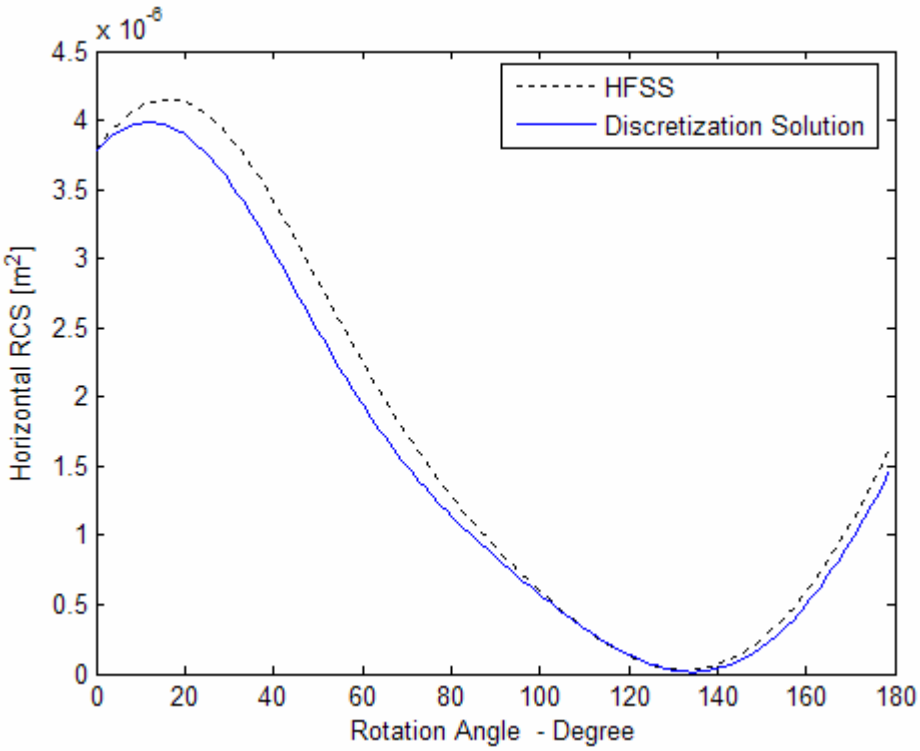

Figure 5.9. Horizontal RCS of arbitrary shape at 100 MHz

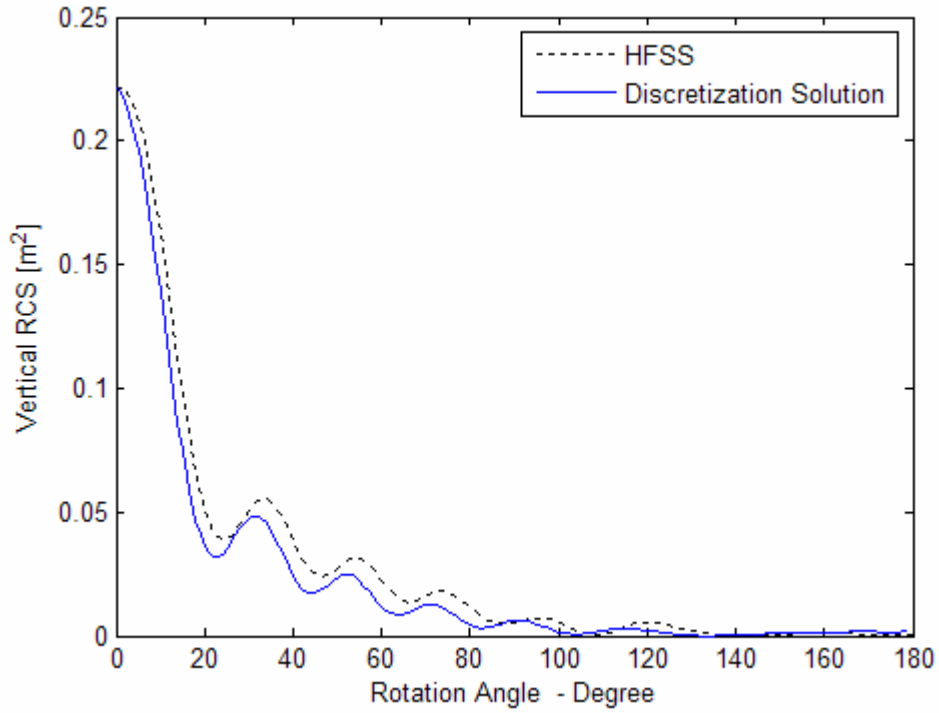

Figure 5.10. Vertical RCS of arbitrary shape at 1 GHz

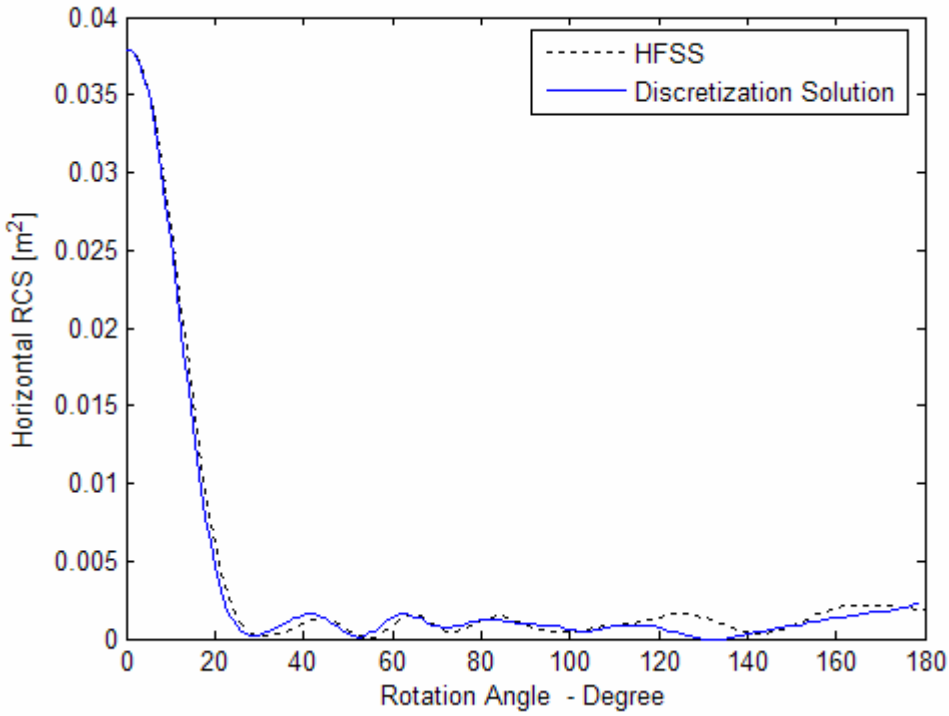

Figure 5.11. Horizontal RCS of arbitrary shape at 1 GHz

As seen Figure 5.8, Figure 5.9, Figure 5.10 and Figure 5.11, similar results are obtained for Radar Cross Section of this arbitrary shape with HFSS and Discretization Solution.

5.2. Arbitrary Shaped Object Obtained From Dielectric Hollow Cylinder with Variable Length

Another arbitrary model is obtained from hollow cylinder whose angle is π instead of 2π. The geometry of this model is shown in Figure 5.12. The length of this model is variable and it changes from 1 cm to 20 cm and 20 cm to 1 cm, respectively. Its thickness is 1 mm. The simulations are done at 100 MHz and 1 GHz, and permittivity of model is 2-0.2j at 100 MHz and 1 GHz.

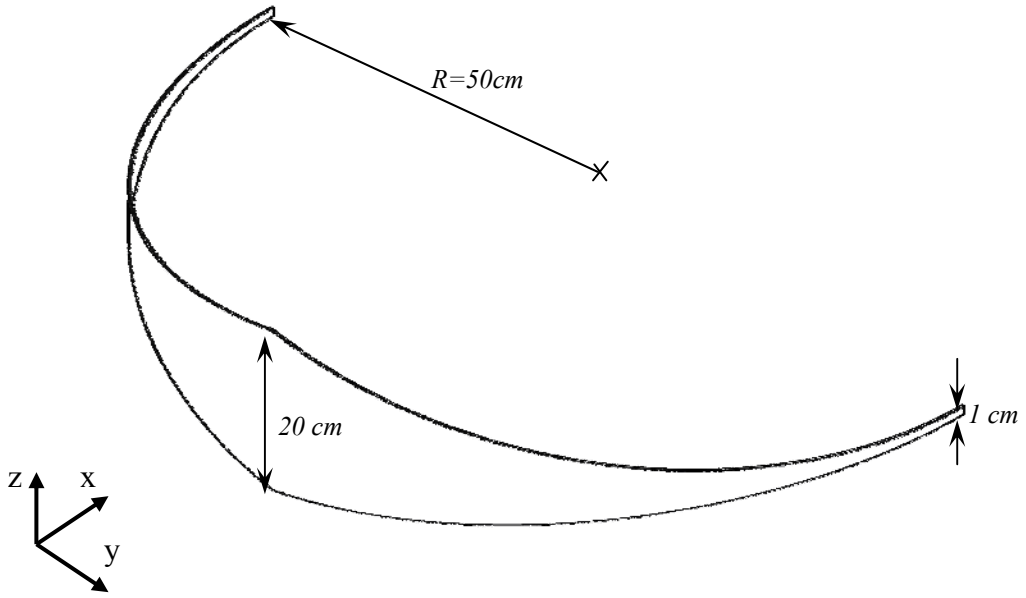

Figure 5.12. The geometry of arbitrary shaped object similar to leave obtained from dielectric hollow half cylinder

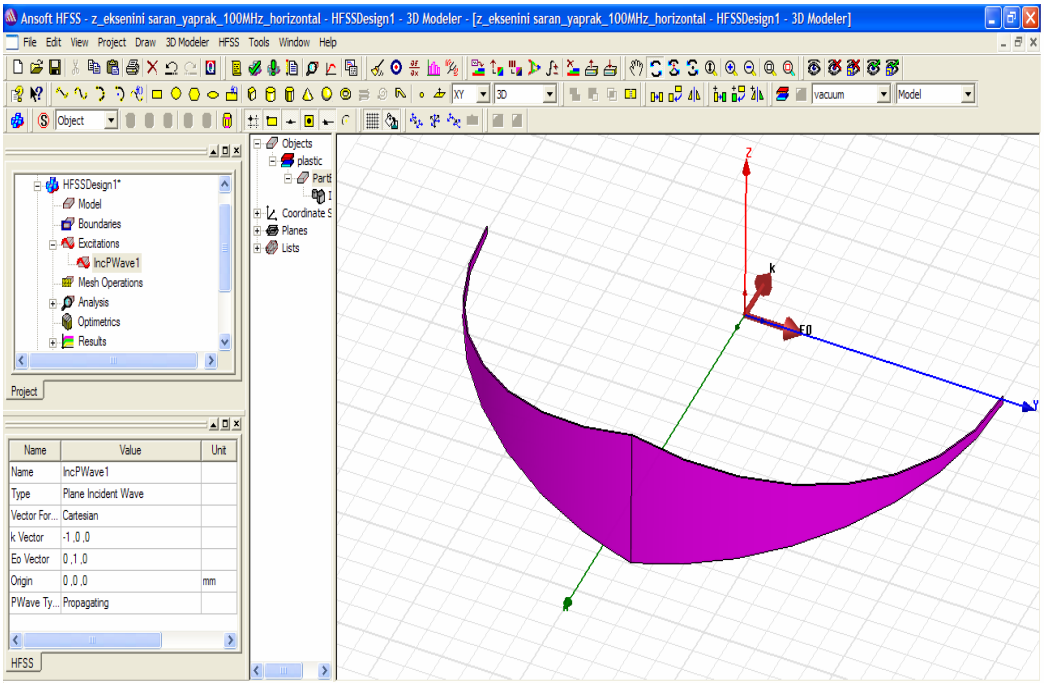

Figure 5.13. Simulation of arbitrary shaped object for horizontal polarization

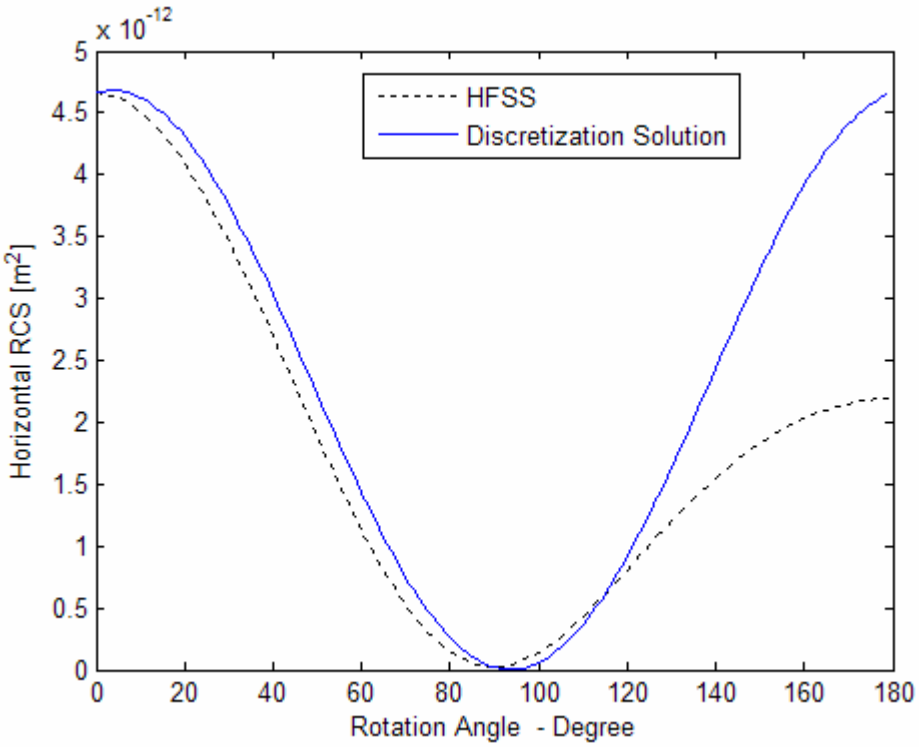

Figure 5.14. Horizontal RCS of arbitrary object at 100 MHz

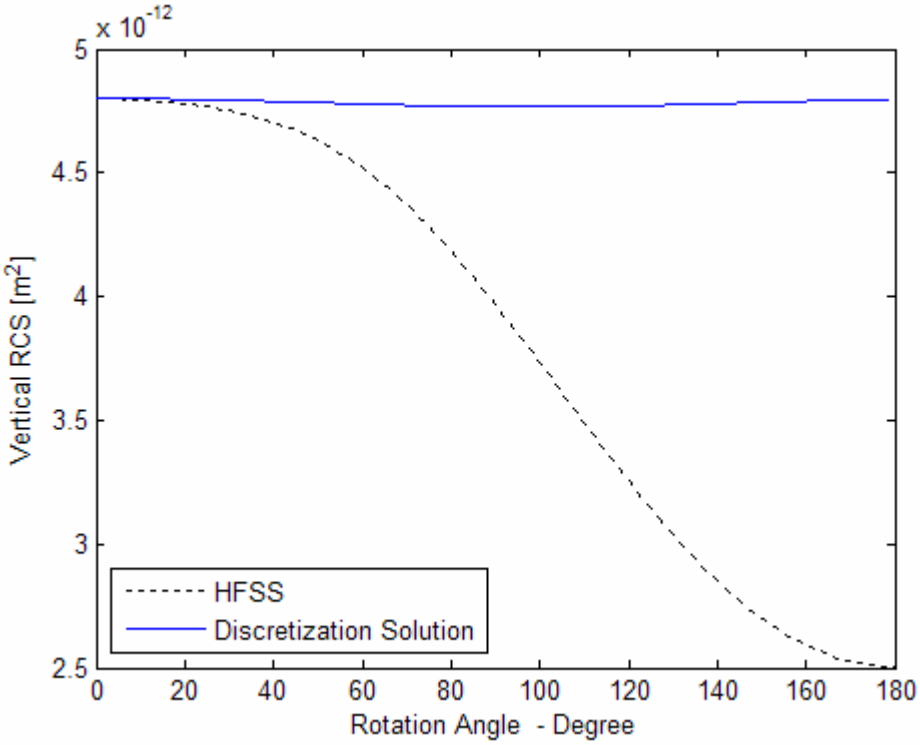

Figure 5.15. Vertical RCS of arbitrary object at 100 MHz

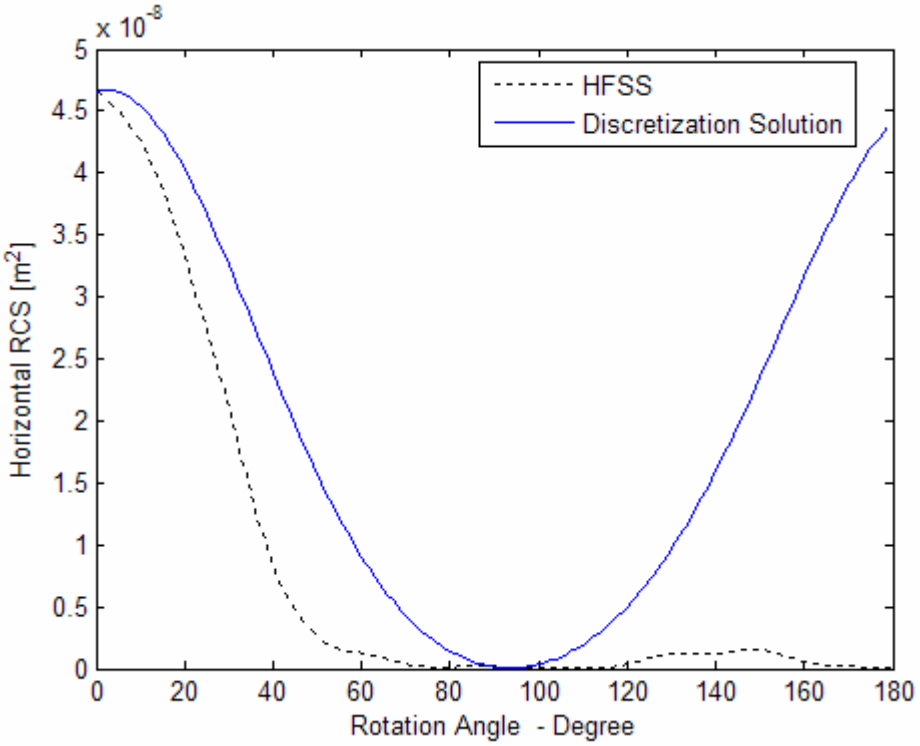

Figure 5.16. Horizontal RCS of arbitrary object at 1 GHz

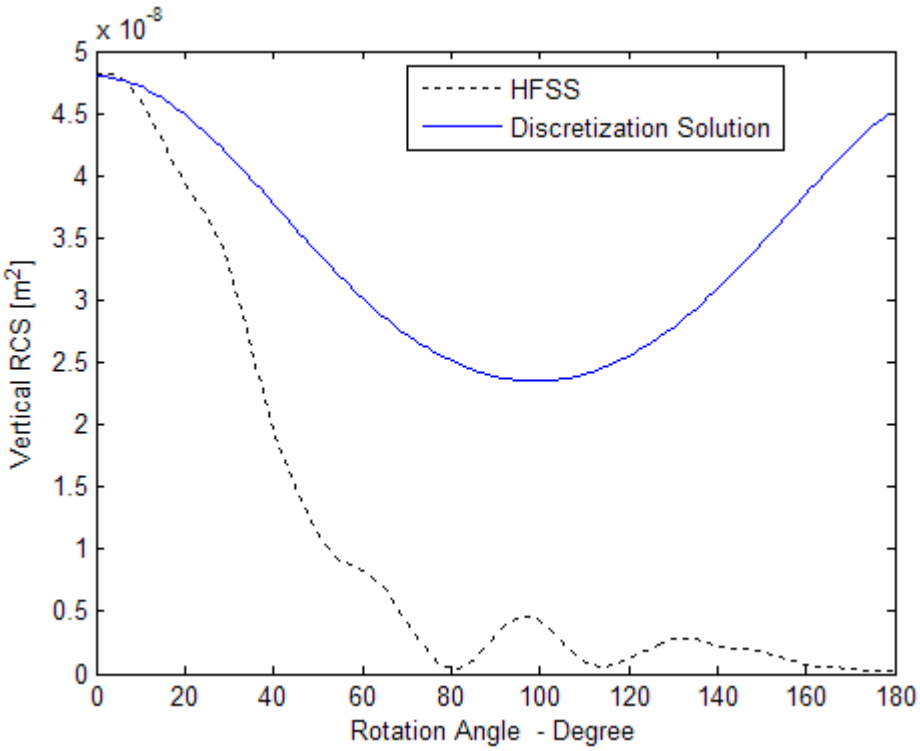

Figure 5.17. RCS of arbitrary object at 1 GHz

The result shows a good agreement behavior up to 120° between HFSS and Discretization Solution for horizontal polarization but the result is not compatible with the result of Discretization Solution for vertical polarization. The results obtained at high frequency do not show a good agreement behavior between HFSS and Discretization Solution for vertical and horizontal polarization.

The second example for this shape that was used in [14] is obtained hollow cylinder whose angle is $3\pi/4$. Its radius is 52 cm, and its permittivity is 29.1-13.3j. The length of the model is variable and it changes from 1 cm to 50 cm and 50 cm to 1 cm, respectively.

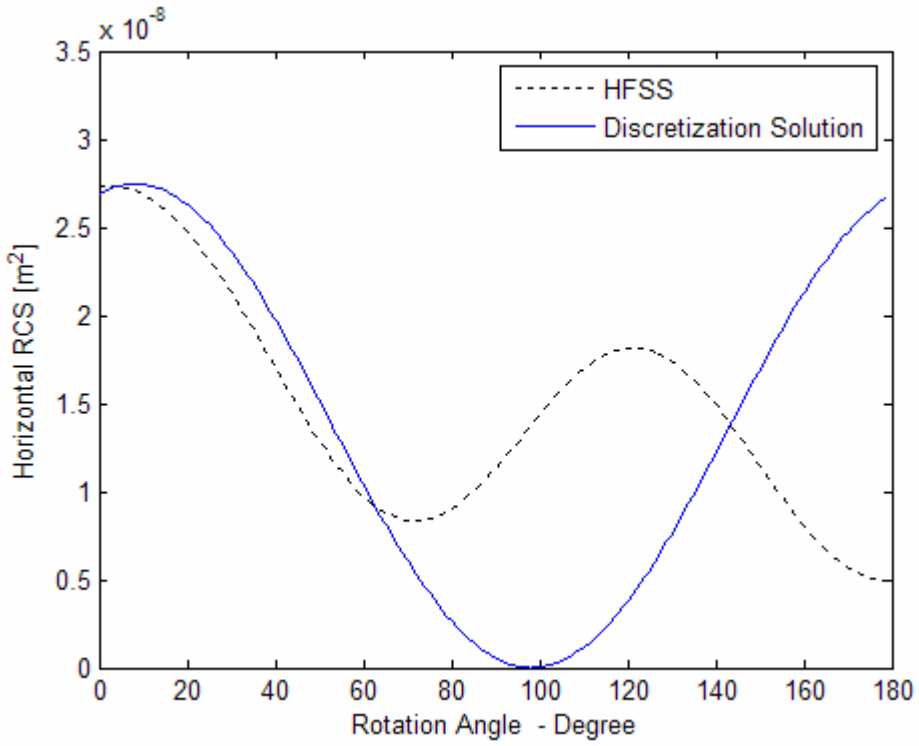

Figure 5.18. Horizontal RCS of arbitrary shape at 100 MHz

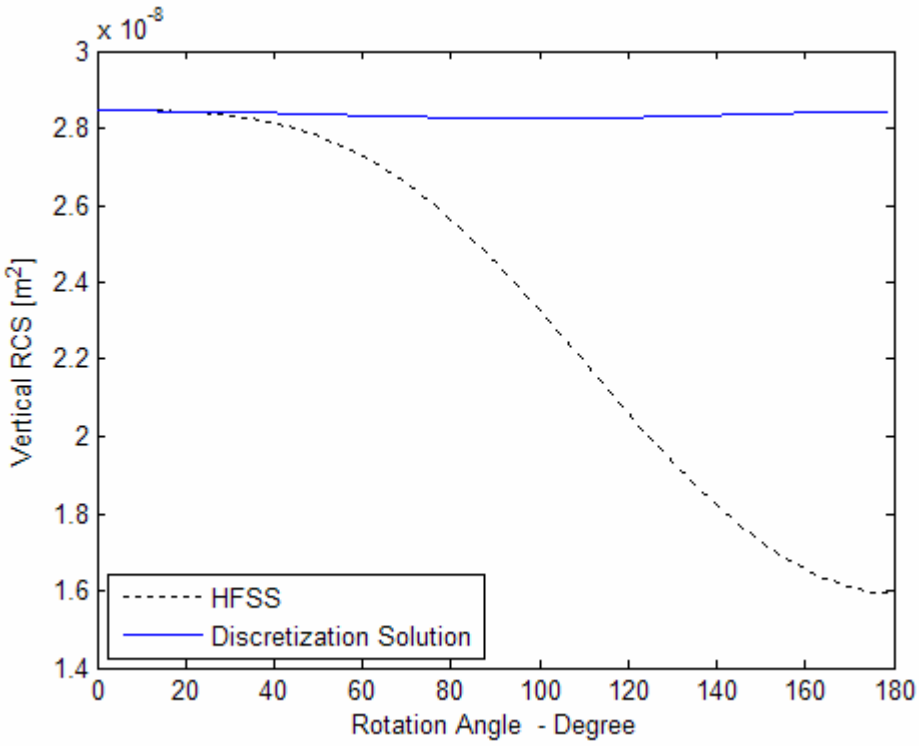

Figure 5.19. Vertical RCS of arbitrary shape at 100 MHz

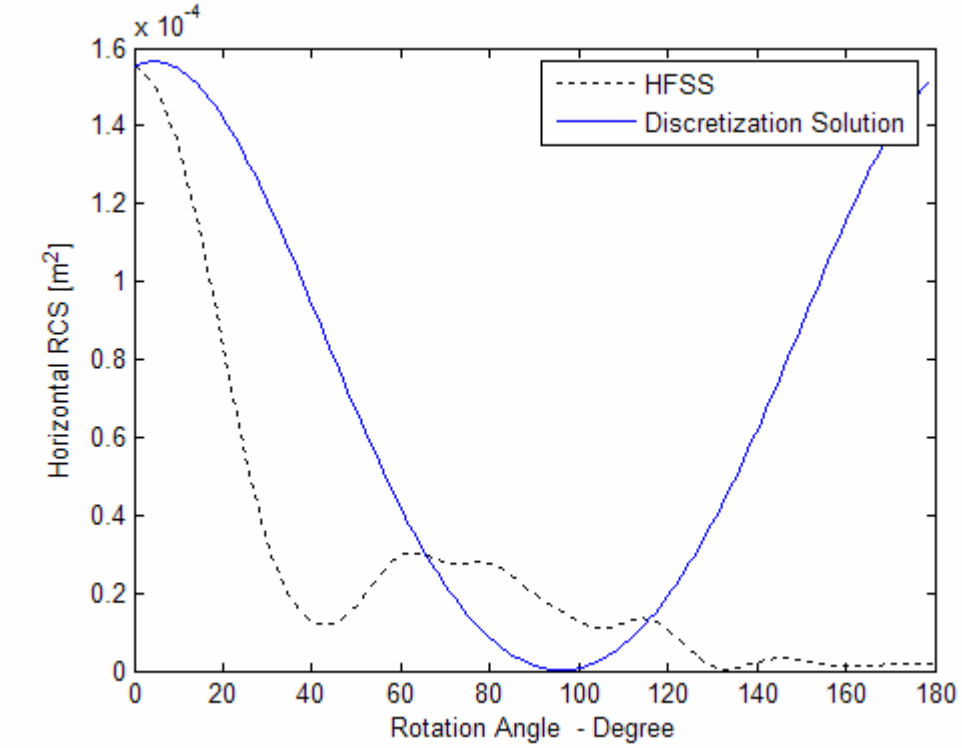

Figure 5.20. Horizontal RCS of arbitrary shape at 1 GHz

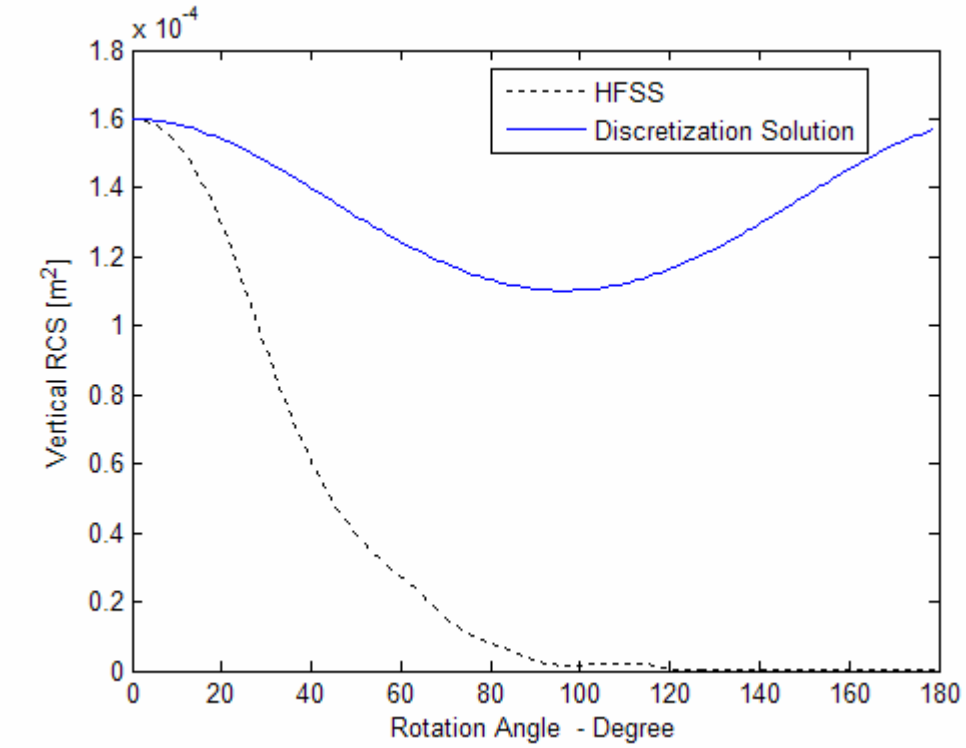

Figure 5.21. Vertical RCS of arbitrary shape at 1 GHz

As seen Figure 5.18, Figure 5.19, Figure 5.20 and Figure 5.21, the results of HFSS and the results of Discretization Solution are not compatible with each other. The first reason for this disharmony may be the permittivity. Discretization Solution is sensitive to the values of permittivities. It is considered that the thickness is the second reason. When the thickness is increased, the results of Discretization Solution deviate from the exact result.

5.3. Arbitrary Shaped Object Obtained from Three-Layered Cylinder

Arbitrary shaped multilayer objects are addressed by considering three-layered hollow cylinders with open apertures. In [14], arbitrary shape is gotten cylinder whose radius is 52 cm, its thickness is 0.1 mm and its length is 100 cm. This arbitrary object's angle is $3\pi/4$ instead of 2π. The permittivities of each layer are 5-5j, 10-20j, 20-10j from the outer to the inner.

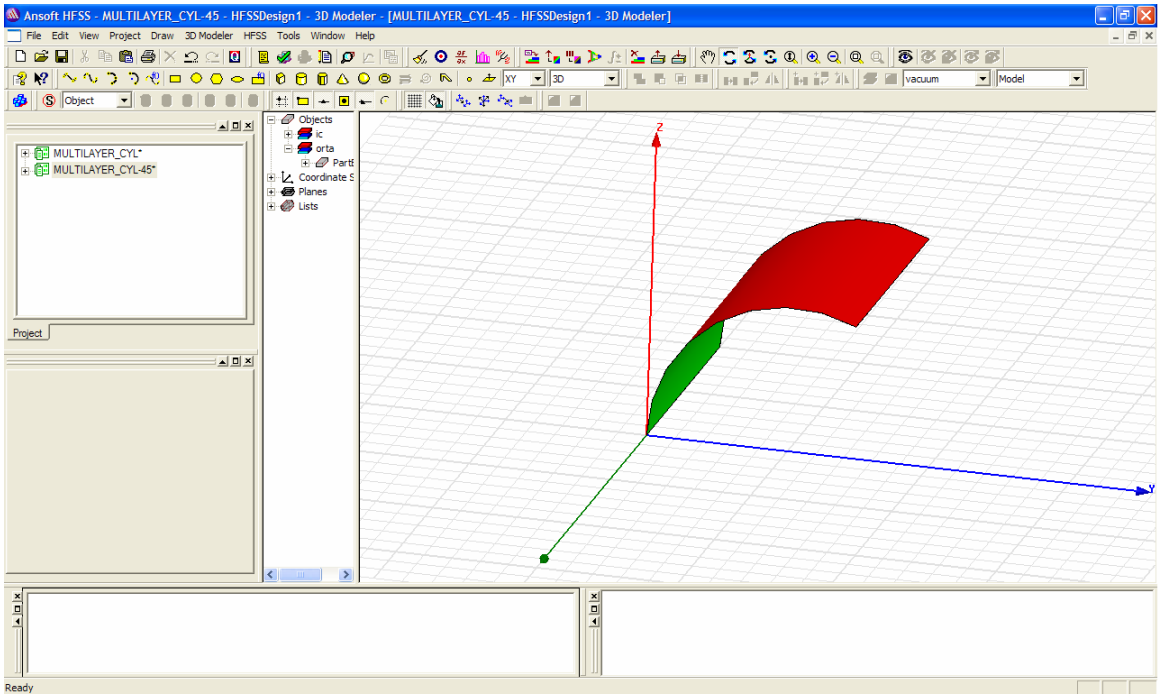

Figure 5.22. Simulation of arbitrary shaped object obtained from three-layered cylinder

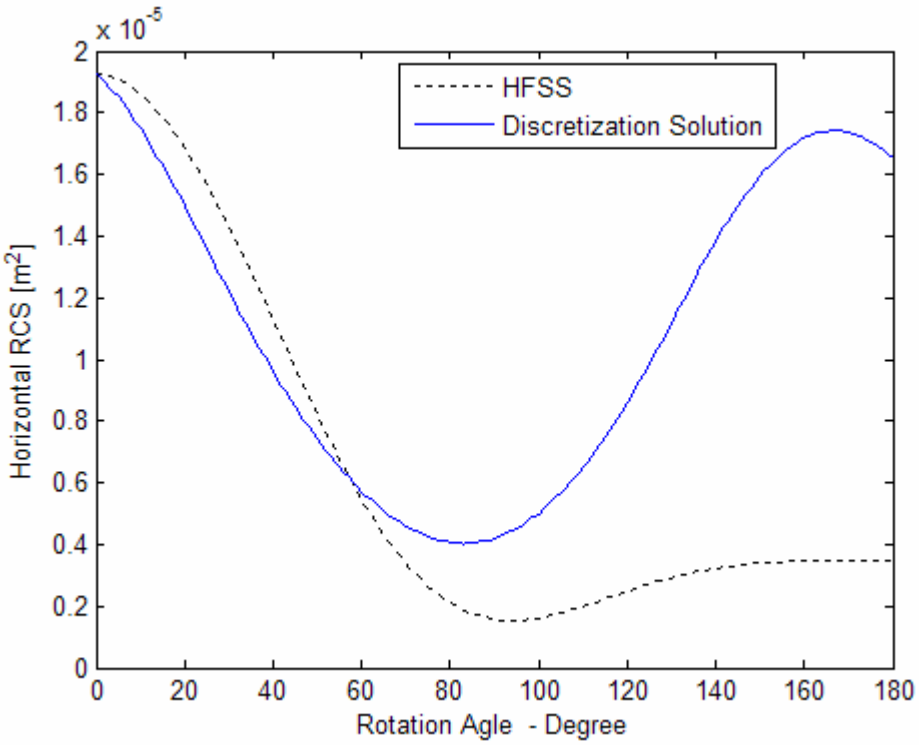

Figure 5.23. Horizontal RCS of arbitrary shape at 100 MHz

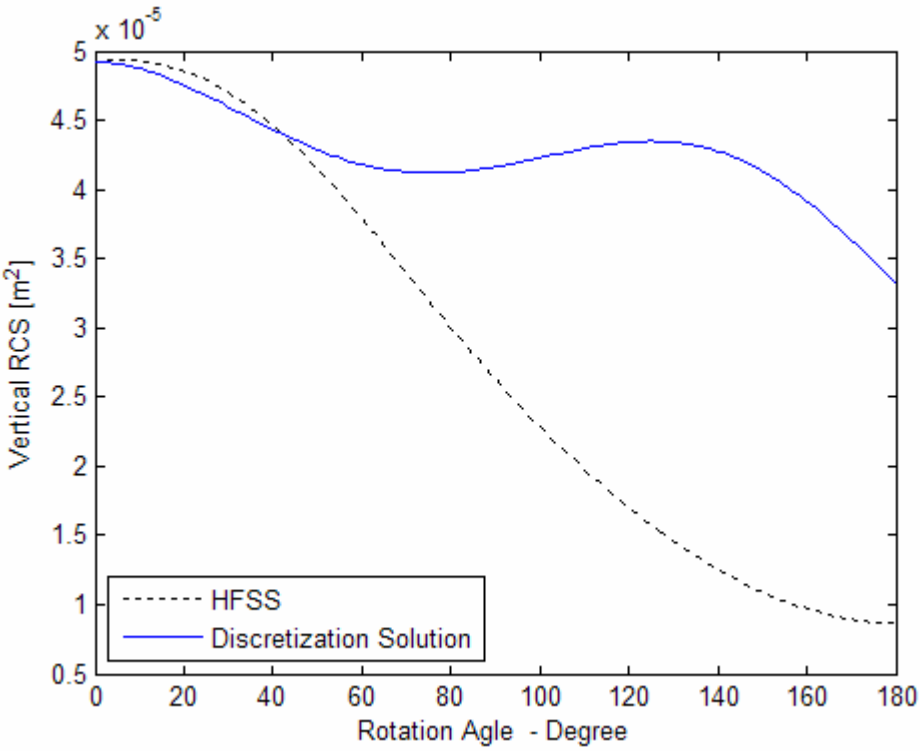

Figure 5.24. Vertical RCS of arbitrary shape at 100 MHz

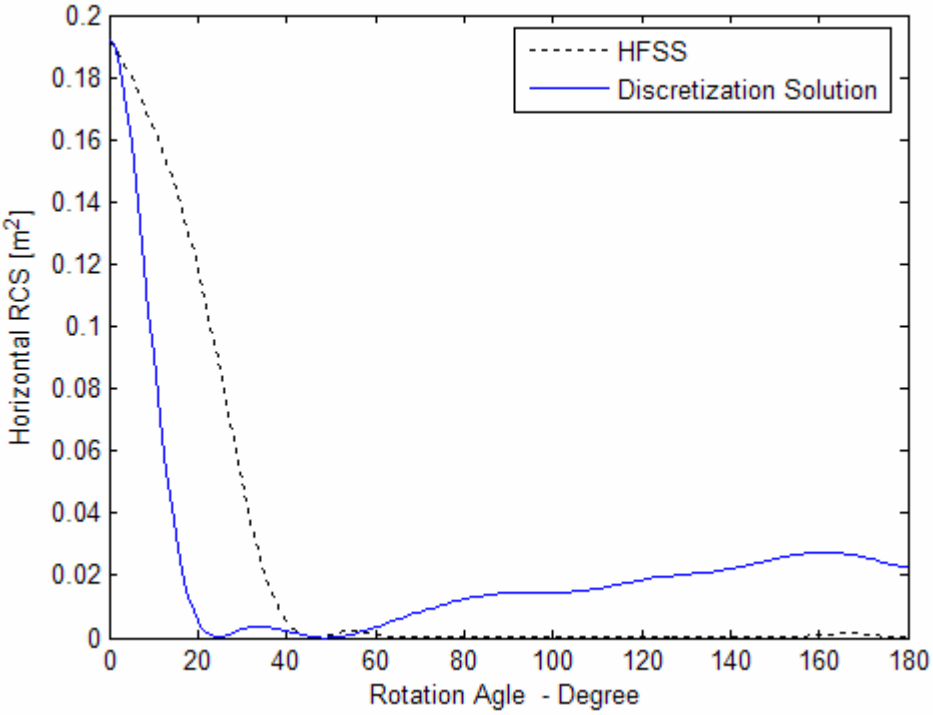

Figure 5.25. Horizontal RCS of arbitrary shape at 1 GHz

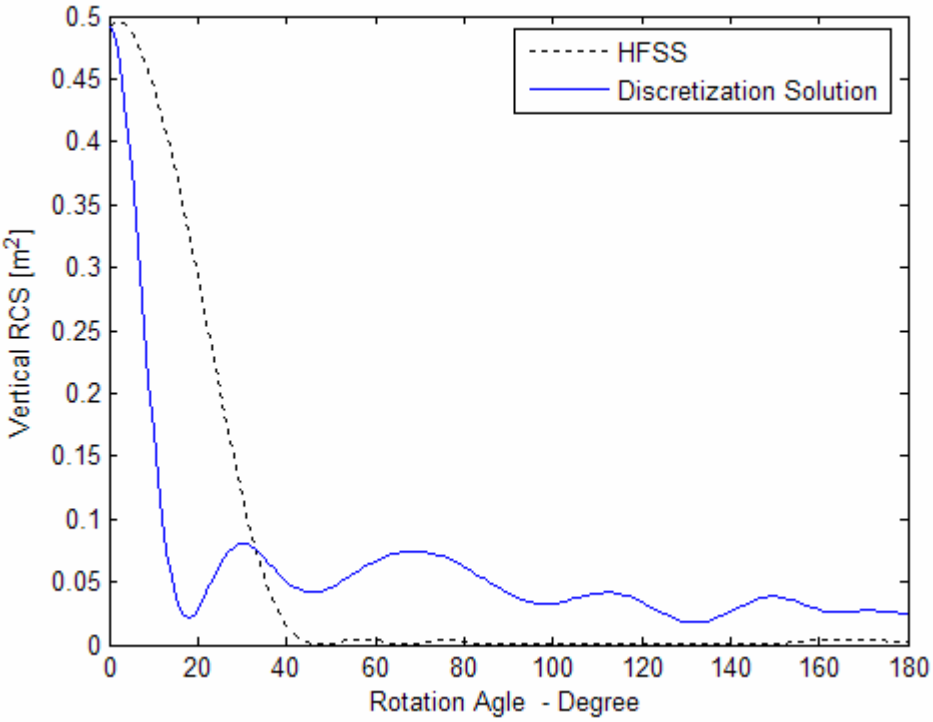

Figure 5.26. Vertical RCS of arbitrary shape at 1 GHz

The results of HFSS and the results of Discretization Solution are not close to each other. As mentioned before, the permittivity and the thickness are important factors when Discretization Solution is used. If these values are increased, the results of Discretization Solution will deviate from the results of HFSS.

5.4. Arbitrary Shaped Object Obtained from Three-Layered Cylinder with Variable Length

The length of this arbitrary object is variable. It is changed from 1 cm to 50 cm and 50 cm to 1 cm, respectively. This object is illustrated in Figure 5.27. The permittivities of layers are 5-5j, 10-20j, 20-10j from inner to outer layer and thickness is 0.1 mm for each layer. The arbitrary shape is gotten from cylinder whose angle is $3\pi/4$ instead of 2π .The results for horizontal and vertical RCS at 100 MHz and 1 GHz are shown in Figure 5.28, Figure 5.29, Figure 5.30 and Figure 5.31, respectively.

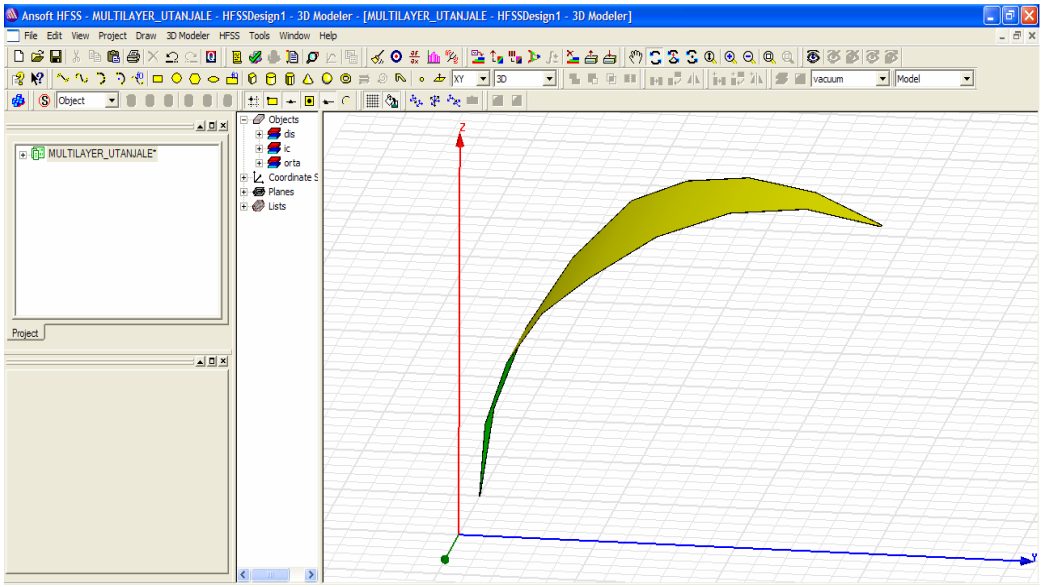

Figure 5.27. Simulation arbitrary shaped object obtained from three-layered cylinder with variable length

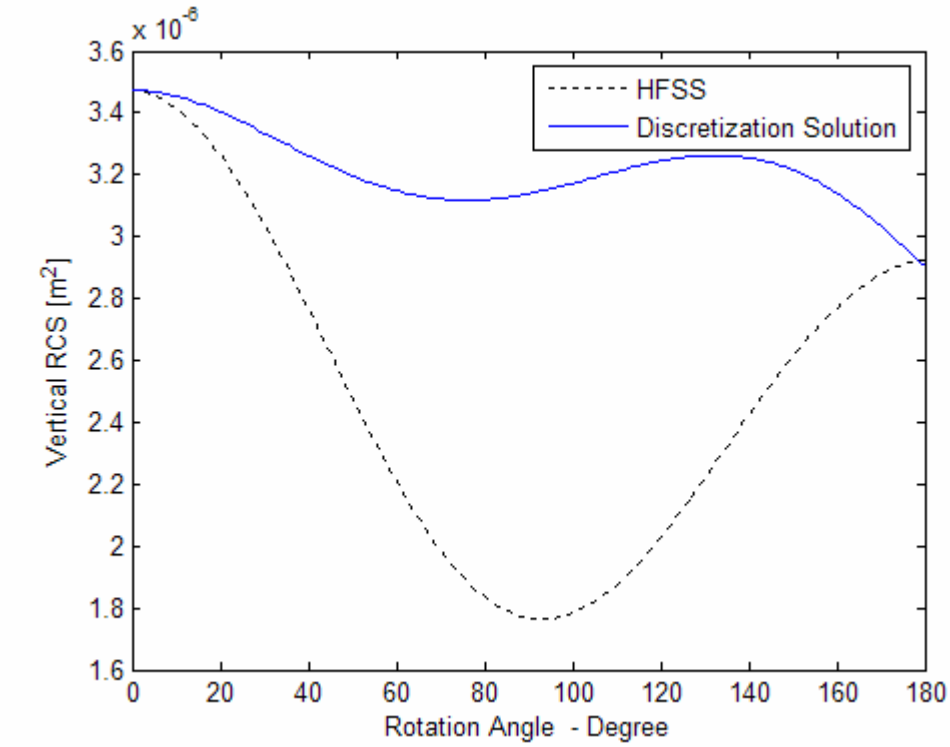

Figure 5.28. Vertical RCS of arbitrary shape at 100 MHz

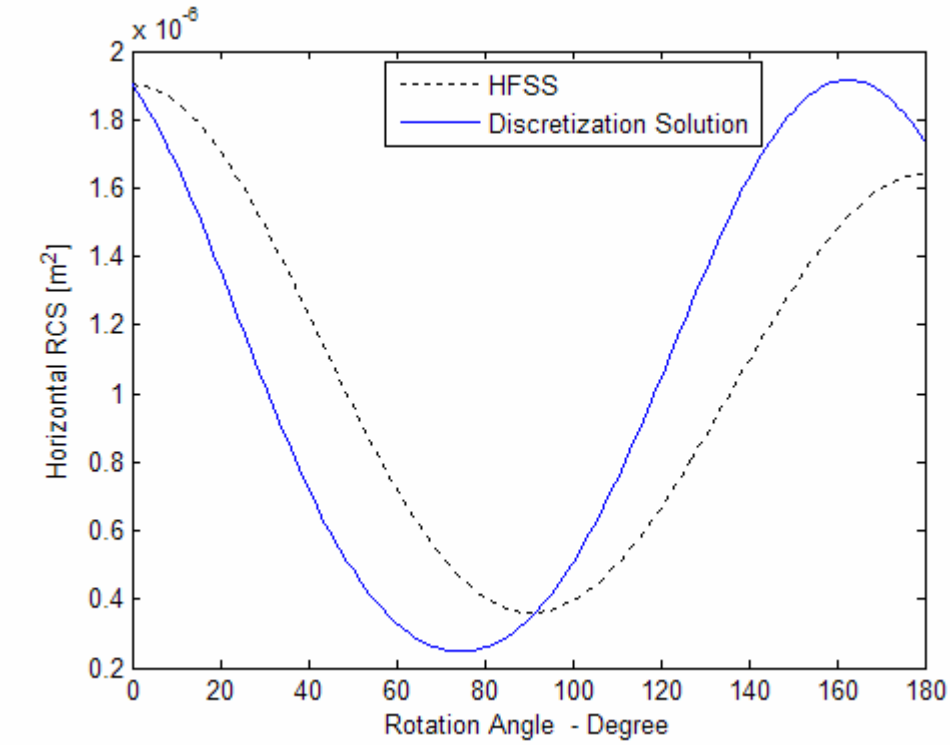

Figure 5.29. Horizontal RCS of arbitrary shape at 100 MHz

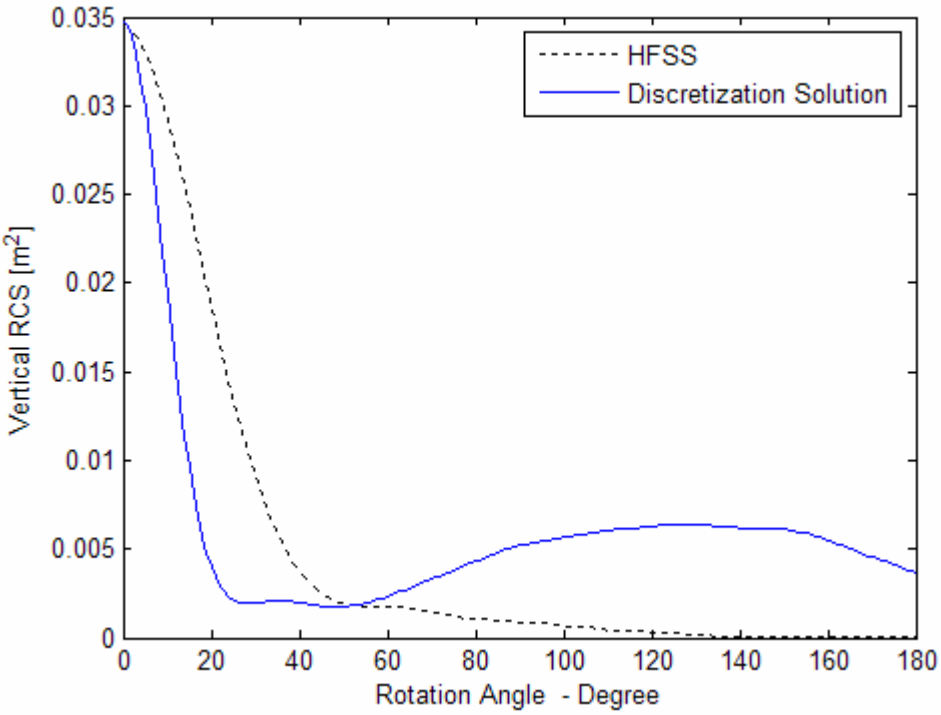

Figure 5.30. Vertical RCS of arbitrary shape at 1 GHz

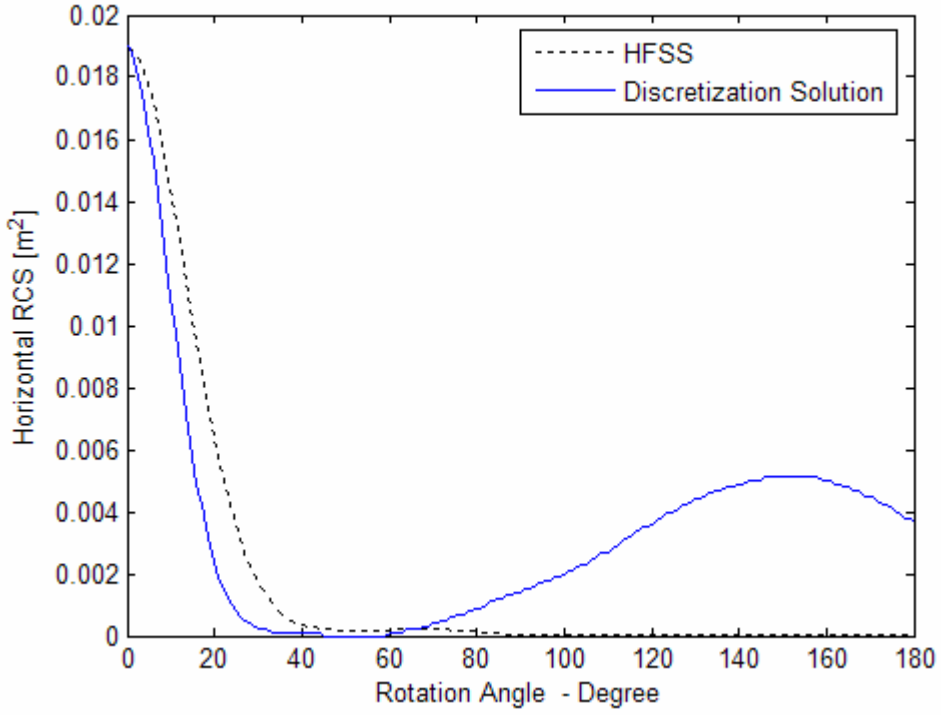

Figure 5.31. Horizontal RCS of arbitrary shape at 1 GHz

5.5. The Accuracy of Discretization Modeling

In order to find the limit of Discretization Model in terms of sizes parameters ka and kT, the relative error is defined as $\frac{\left|\sigma_{Discretization\ method} - \sigma_{Richmond}\right|}{\left|\sigma_{Richmond}\right|}$. Firstly, relative error versus ka for a cylinder consisting of a single layer is presented. The results are shown in Figure 5.32(a). Following this the results for a three layer cylinder are illustrated in Figure 5.32(b).

For single layer hollow cylinder the thickness (T) is 1 mm, radius (R) is 0.2 m, permittivity is 2-0.2j, and the length is 1 m. For the three layered cylinder each layer has a thickness of 1 mm and permittivities [4-0.4j 3-0.3j 2-0.2j] from inner to outer with the same radius and length as the single layered cylinder. It is seen from the figures that for both vertical and horizontal cases, the relative error is about 1-2 per cent for $ka \le 1$. After that vertical polarization oscillates more than the horizontal polarization. The vertical polarization is more sensitive to the values of permittivities.

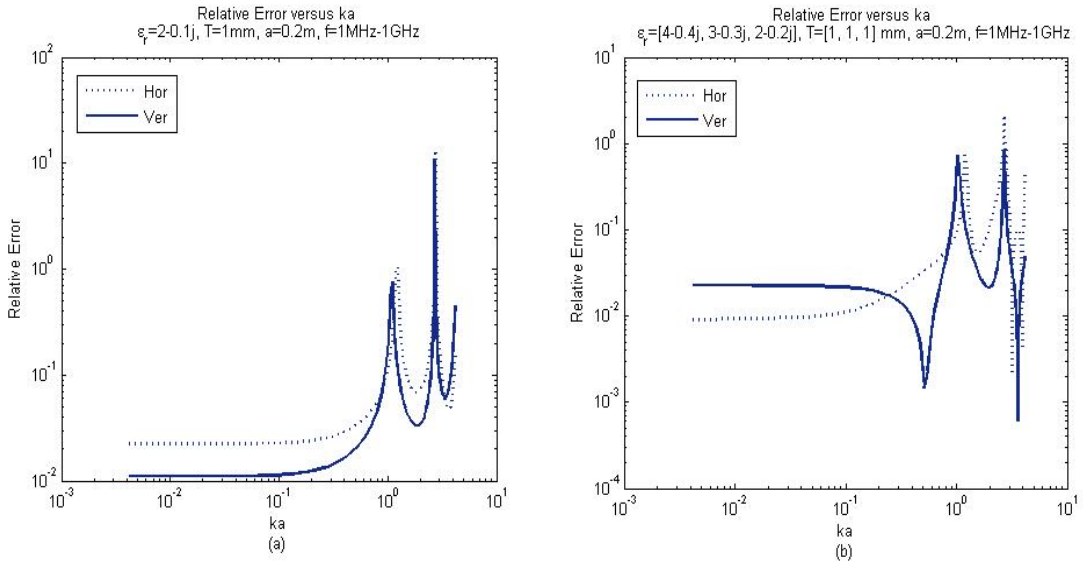

Figure 5.32. Relative error versus ka of hollow cylinder (a) single layer (b) three layer

Secondly, it is presented the relative error versus kT for the single layer and three layer cases in Figure 5.33(a) and (b). For the case of single layer hollow cylinder, the

cylinder radius, R is 0.2 m, and the cylinder wall permittivity is 2-0.2j and its length is 1 m. For the three layered cylinder the permittivities are [4-0.4j 3-0.3j 2-0.2j] from inner to outer layer respectively with the same radius and length as the single layered cylinder. It is seen from the figures that the relative errors are about 2-3 per cent for both vertical and horizontal polarization, and the fairly constant for $kT\langle 0.02$.

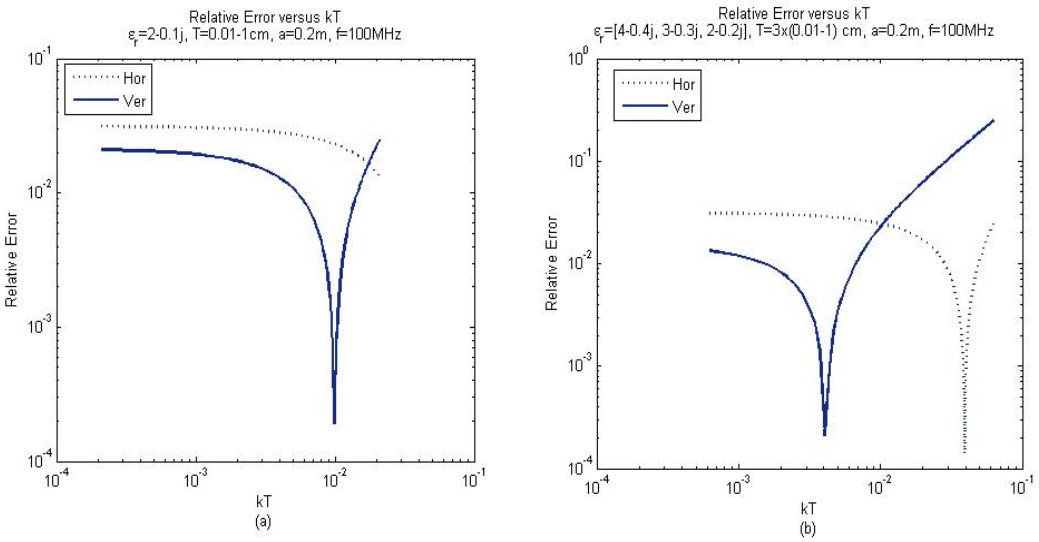

Figure 5.33. Relative error versus kT of hollow cylinder (a) single layer (b) three layer

6. RADAR CROSS SECTION SIMULATION OF EXTENDED ARBITRARY SHAPES

In this section, RCS of extended arbitrary shapes are examined. Curved circular surfaces and toroid are the examples of these extended arbitrary shapes. RCS of these extended arbitrary shapes are calculated by HFSS at low and high frequencies. This study considers the properties of corn leaves of vegetation. First surface is quarter circle and second surface is semi circle in xy-plane. The first model curved quarter circle surface used in [21] is illustrated in Figure 6.1.

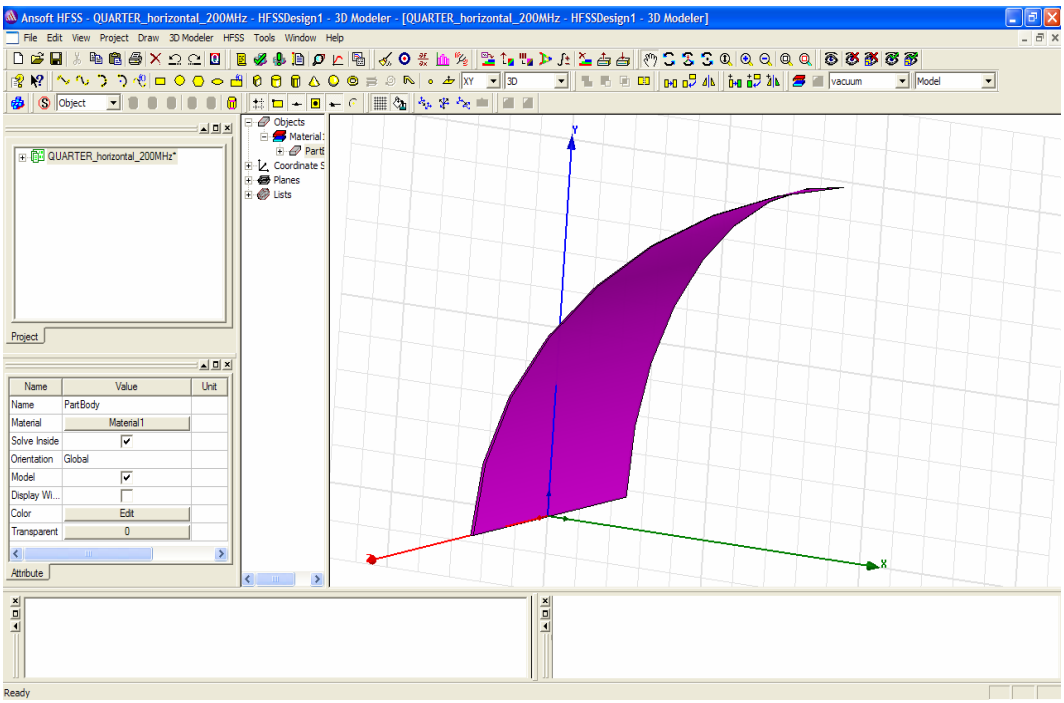

Figure 6.1. Curved quarter circle surface given in [21]

The Bi-static RCS of curved quarter circle surface is calculated by using HFSS at 200 MHz and 1 GHz. The thickness and width are varied from 0.35 mm to 0 and 5.8 cm to 0 along z-axis, respectively. The permittivity is 22.8-7.35j. The results are illustrated in Figure 6.2 and Figure 6.3 at 200 MHz and 1 GHz, respectively.

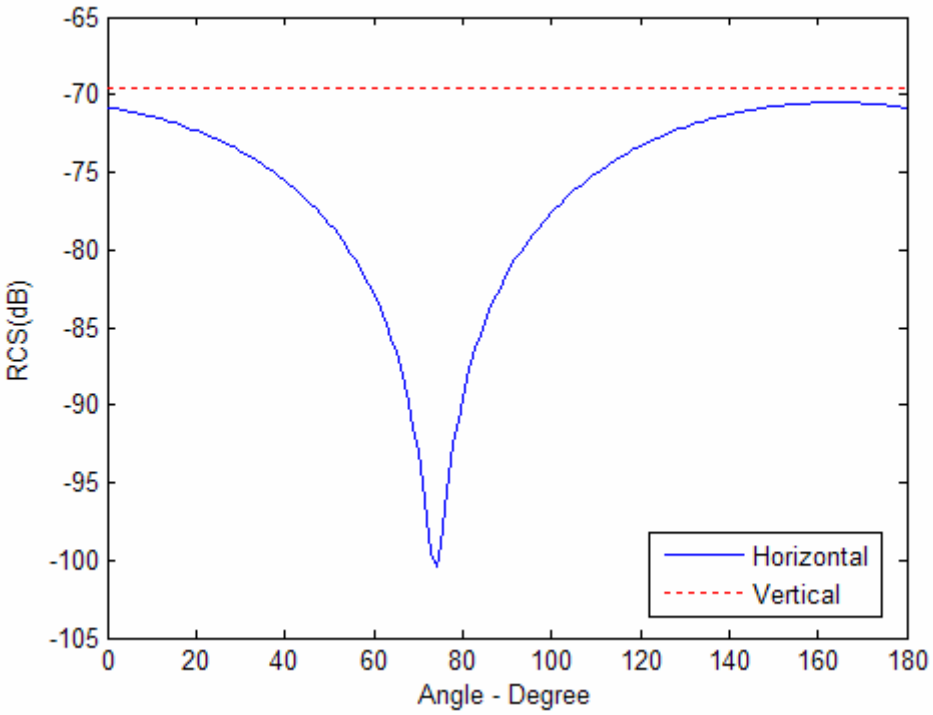

Figure 6.2. RCS of curved quarter circle surface at 200 MHz

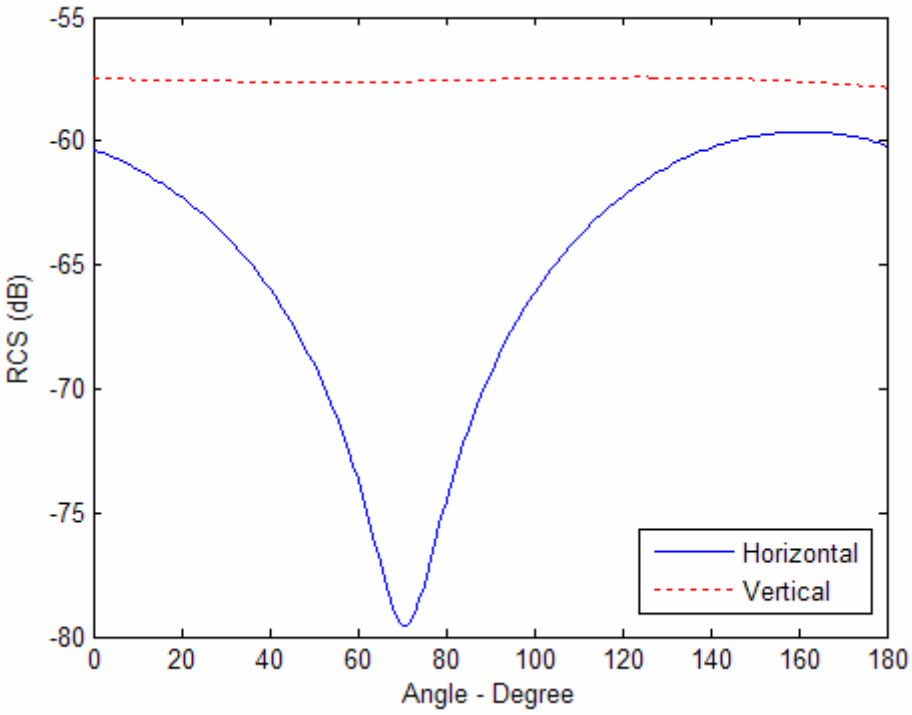

Figure 6.3. RCS of curved quarter circle surface at 1 GHz

The RCS of this curved quarter circle surface was also calculated by using quasi static approximation in [21] at 200 MHz. A good agreement behavior is observed between the result of HFSS given in Figure 6.2 and the result of Discretization Solution given in Figure 6.4.

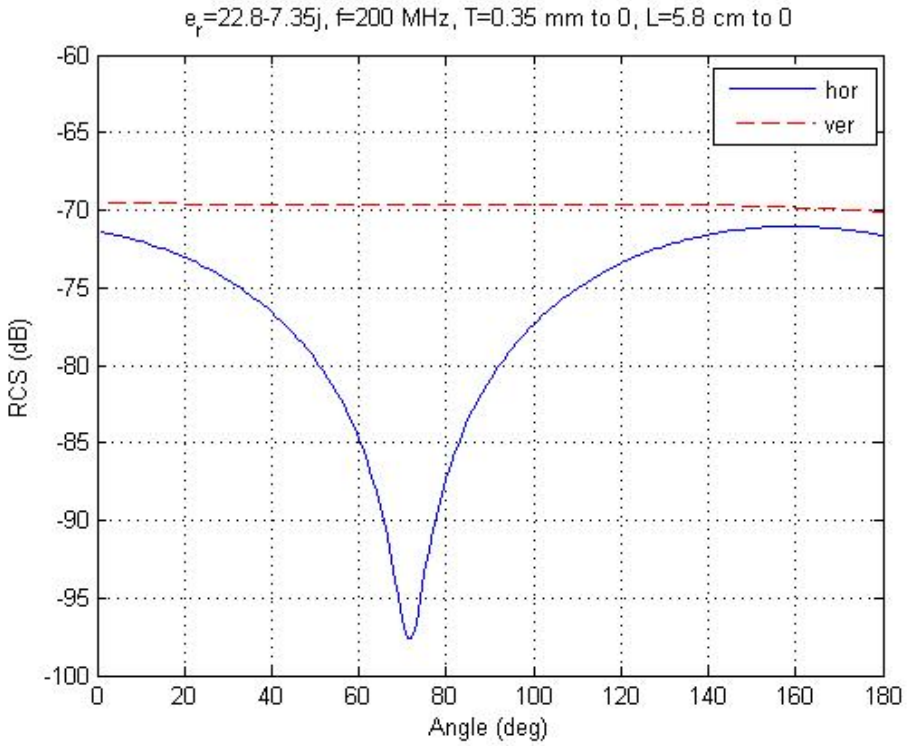

Figure 6.4. RCS for curved quarter circle surface [21]

The second example is curved semicircle surface given in [21]. The thickness and width are varied from 0.35 mm to 0 and 5.8 cm to 0 along z-axis, respectively. The permittivity is 22.8-7.35j. It is shown in Figure 6.5.

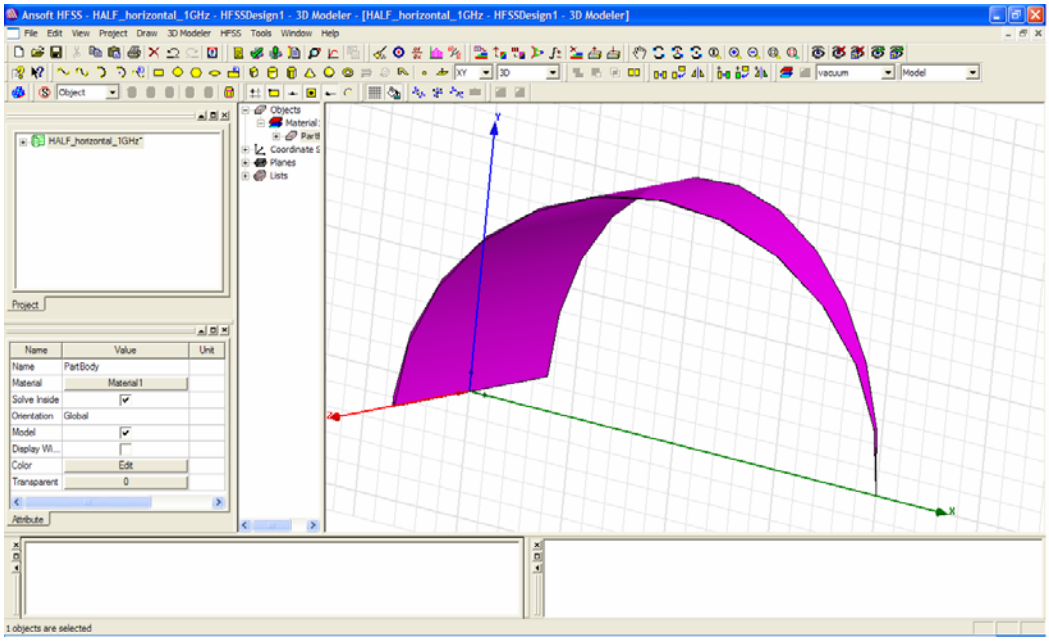

Figure 6.5. Curved semicircle surface given in [21]

The Bi-static RCS of curved semicircle surface is calculated by using HFSS at 200 MHz and 1 GHz. The results are illustrated in Figure 6.6 and Figure 6.7 at 200 MHz and 1 GHz, respectively.

The RCS of this curved quarter circle surface was also calculated in [21] by using quasi static approximation. The result of HFSS given in Figure 6.6 and the result of Discretization Solution given in Figure 6.8 are compatible with each other.

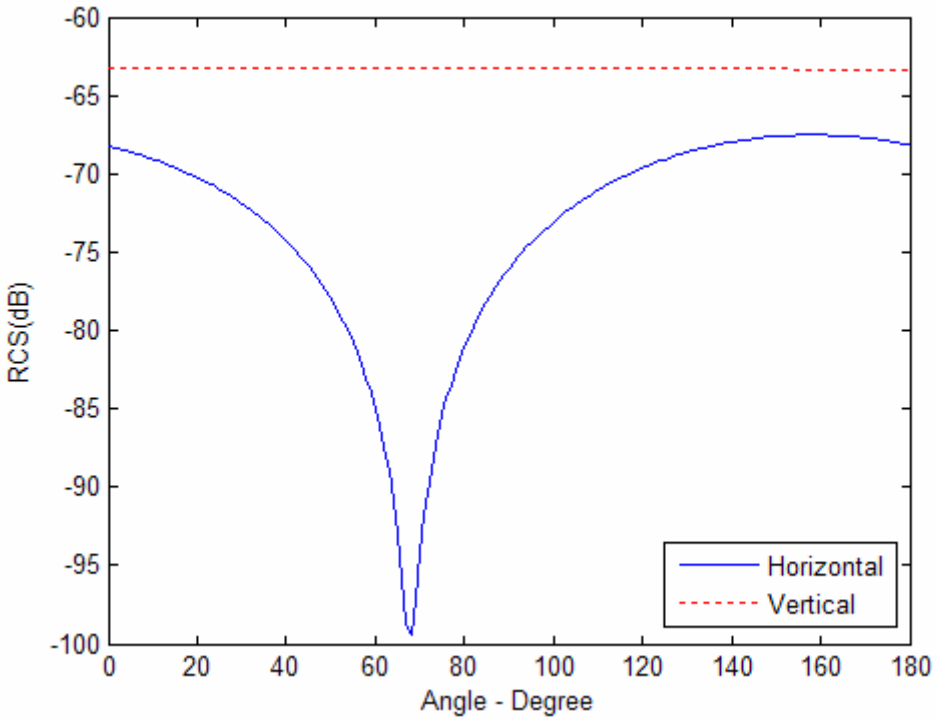

Figure 6.6. RCS of curved semicircle surface at 200 MHz

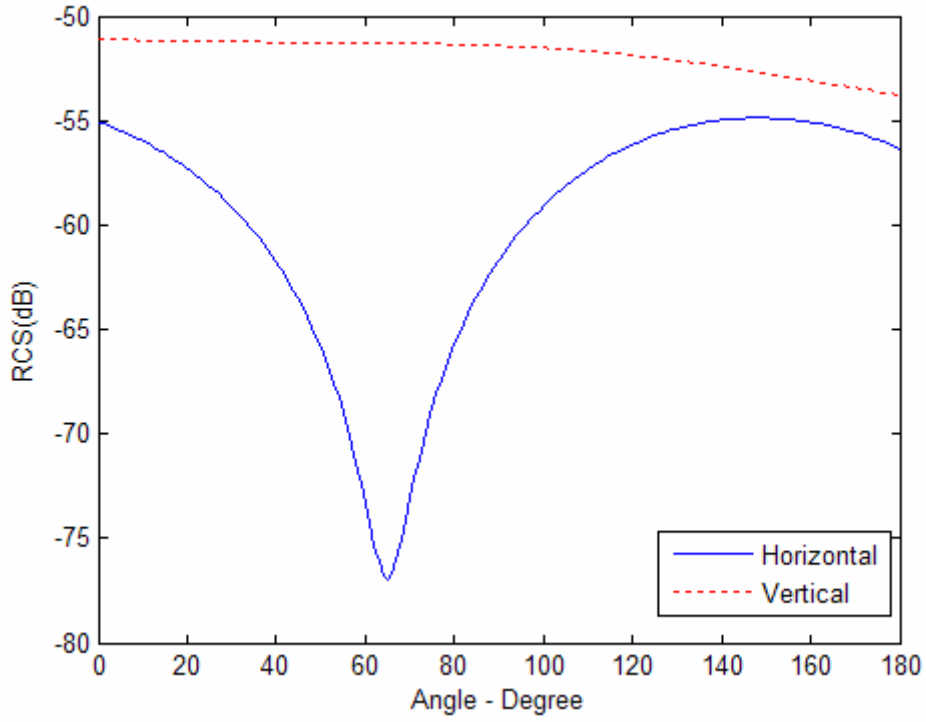

Figure 6.7. RCS of curved semicircle surface at 1 GHz

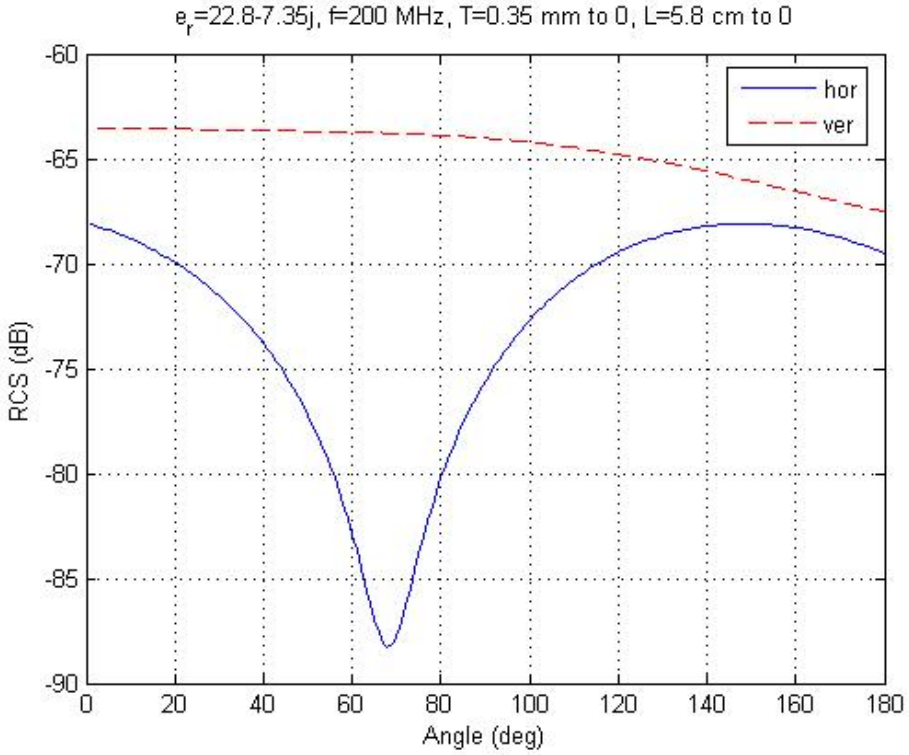

Figure 6.8. RCS for curved semicircle surface [21]

Last example is thin toroid, it is shown in Figure 6.9. Bi-static RCS of toroid is calculated at 200 MHz and 1 GHz, respectively. Results are given in Figure 6.10, Figure 6.11, Figure 6.12 and Figure 6.13.

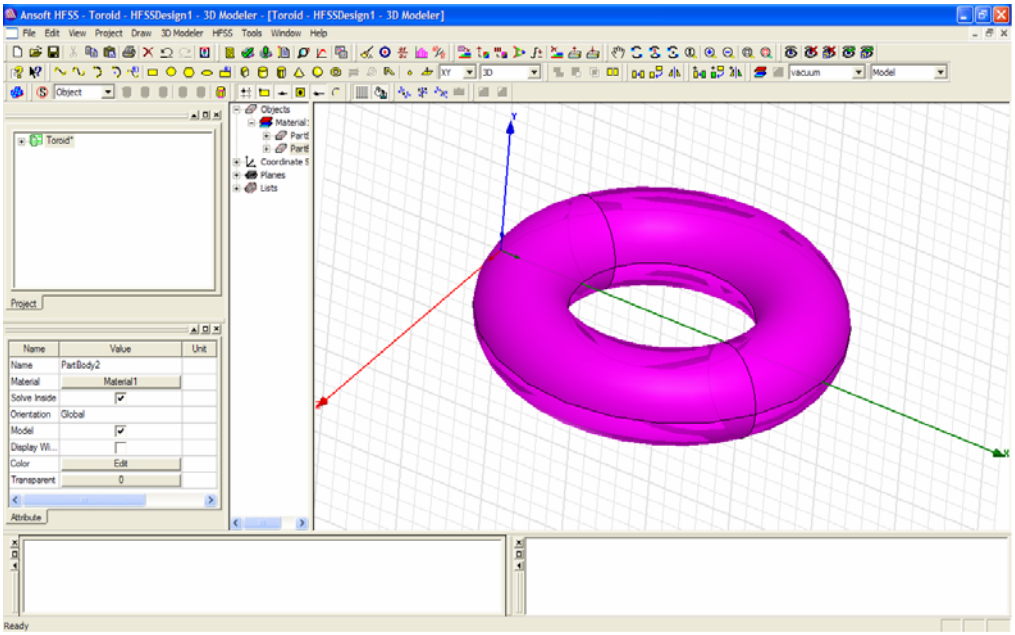

Figure 6.9. Simulation of thin toroid

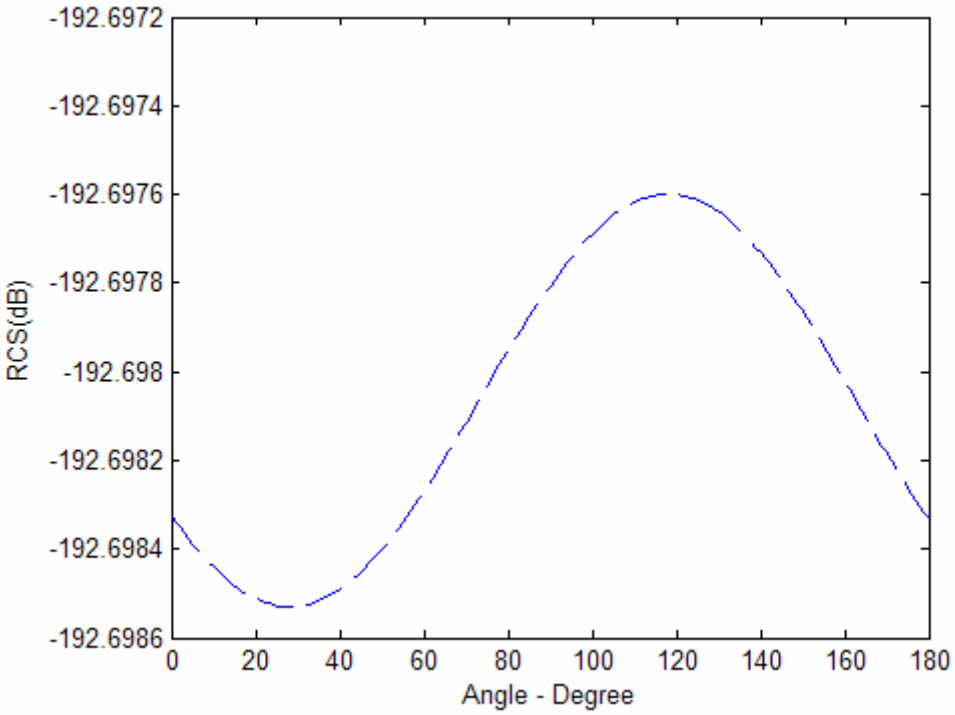

Figure 6.10. Vertical RCS of thin toroid at 200 MHz

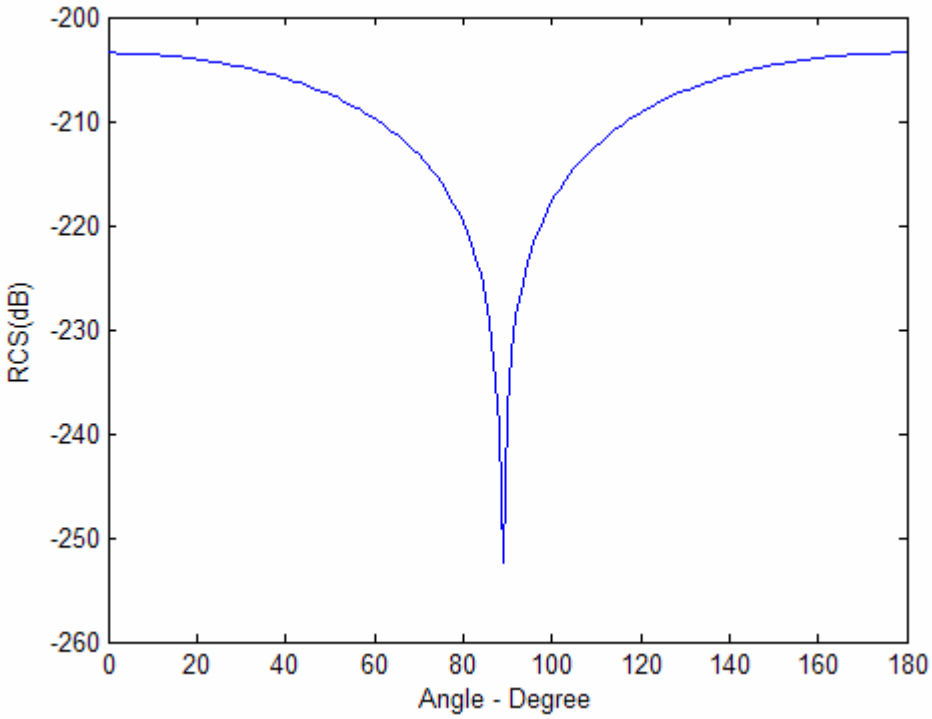

Figure 6.11. Horizontal RCS of thin toroid at 200 MHz

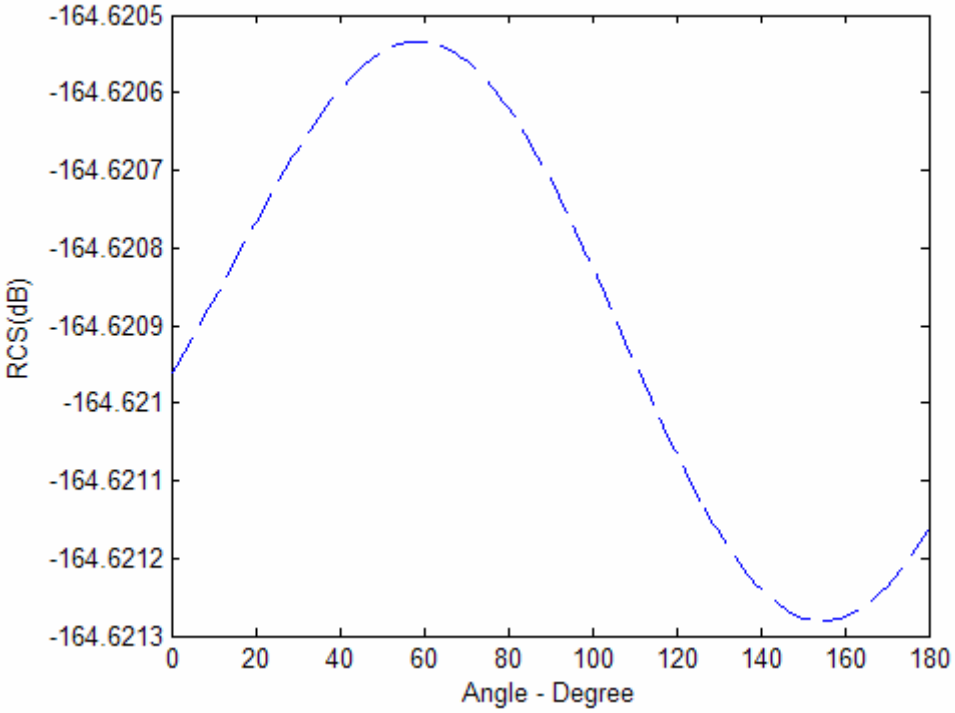

Figure 6.12. Vertical RCS of thin toroid at 1 GHz

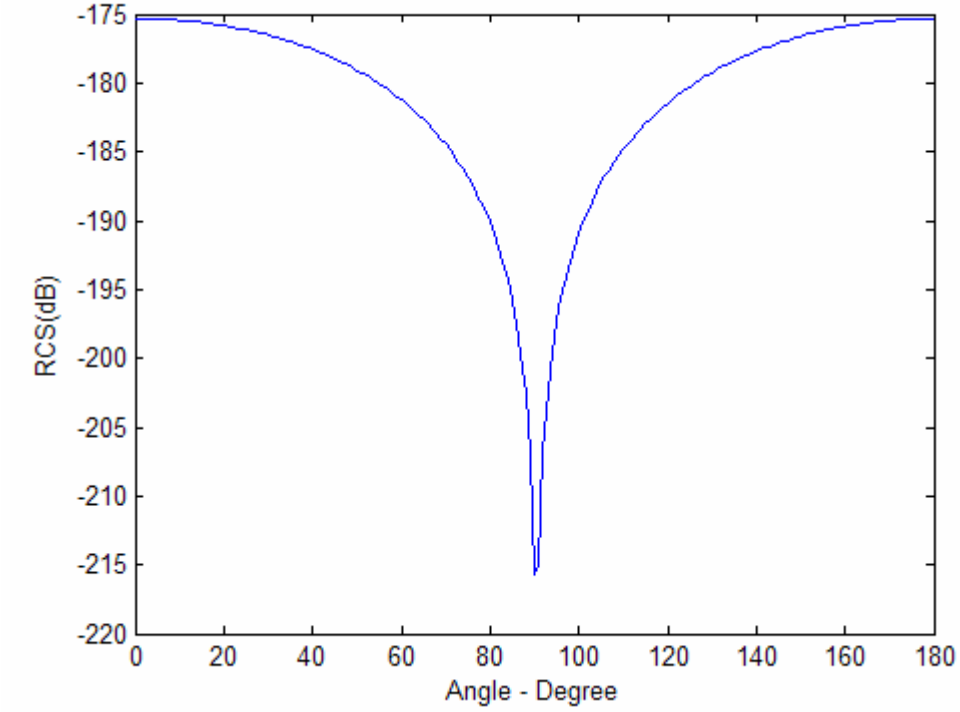

Figure 6.13. Horizontal RCS of thin toroid at 1 GHz

7. CONCLUSION

In this thesis, radar cross section measurements and simulations of dielectric arbitrary shapes have been studied. First of all, simple shapes such as, flat plate, cylinder, have been studied in order to ensure the truth of experimental and HFSS simulation results by comparing with theoretical results given in former studies. After that, arbitrary shaped object obtained from hollow cylinder and extended arbitrary shapes were studied. Measurements were done for both conducting and dielectric materials for vertical polarizations at 3 GHz, and HFSS simulation results were obtained both vertical and horizontal polarizations at 3 GHz. Furthermore, RCS results were obtained both low and high frequencies to verify Discretization Solution.

Firstly, conducting flat plate was studied. For comparison between theory and experiment, Ross's solution was used. Ross used Geometrical Theory of Diffraction method in [10] for calculation of RCS of conducting flat plate so as to account polarization. In [10], geometrical diffraction theory showed the correspondence between analytical and measured data for $0^\circ \le \theta \le 80^\circ$. Good agreement behavior was obtained for my experimental result and geometrical diffraction theory's result. With Ansoft HSSS simulation, monostatic RCS of flat plate was also obtained for vertical and horizontal polarizations. While an exact agreement was seen for vertical polarizations, the differences were observed between theory and simulation results for horizontal polarizations. Since different methods are used in theory and simulator to calculate RCS.

After that, bi-static radar cross section measurement was done for perfectly conducting cylinder. Analytical solution was obtained from Balanis's Solution given in [11] to compare with experimental result. Comparison illustrated the correspondence at angles of nadir. Asymmetries that were presented in the experimental result not in the theory were important differences. On the other hand, a perfect agreement between HFSS simulation and theory were seen for vertical and horizontal polarizations.

After conducting materials, RCS of dielectric models was measured. Monostatic RCS of dielectric disc was calculated by HFSS simulator. After that, Le Vine's results given in [12] were used to compare with simulation results. A good agreement behavior was obtained for both vertical and horizontal polarizations at 3 GHz.

Hollow cylinder was chosen as a model in next step. The measurement was conducted in the Electromagnetic and Diagnostic Laboratory of ITU in order to obtain bi-static RCS of dielectric cylinder at 3 GHz. Richmond's result given in [18] was used to compare with experimental result. The results were not close to each other because plastic was lossy dielectric. While its permittivity's was measured at 1.8 GHz, measurement was done at 3 GHz. On the other hand, simulation results showed perfect agreement behavior with theoretical results for vertical and horizontal polarizations.

After the simple shapes, RCS of arbitrary shapes was calculated. First of all, arbitrary shaped objects were obtained from dielectric hollow cylinder to compare with the results obtained from Discretization Method [14]. The first arbitrary model was formed by cutting the hollow cylinder in the direction of length. As shown in Figures, a good agreement behavior was obtained between HFSS simulation results and Discretization method's results at both low and high frequencies. Another model was formed from semi circle hollow cylinder. Its length was variable and it changed from 1 cm to 20 cm and 20 cm to 1 cm, respectively. The result showed similarity up to 120° between HFSS and Discretization Solution for horizontal polarization, but the results deviated from each other for vertical polarization. The results of HFSS were not close to the result of Discretization Solution for vertical and horizontal polarization at 1 GHz.

In addition to the simulation of arbitrary shapes obtained from hollow cylinder, simulation of arbitrary shapes obtained from three-layered cylinder was also calculated. The first model was obtained by cutting three-layered cylinder whose angle was $3\pi/4$ instead of 2π. The results of HFSS were not compatible with the results of Discretization Solution's results for both vertical and horizontal polarizations at 100 MHz and 1 GHz. Furthermore, bi-static RCS of arbitrary shape with variable length was also calculated. At

low frequency, the result of Discretiztion soution was close to the result of HFSS, but at high frequency, the results deviated from each other.

Lastly, bi-static RCS of extended arbitrary shapes was calculated by using HFSS. This study considered the properties of corn leaves of vegatation. Bi-static RCS of these models was similar with the results given in [21] at 200 MHz. Moreover, a thin toroid was also calculated by HFSS at 200 MHZ and 1 GHz, respectively.

In conclusion, the exact results were obtained for monostatic and bistatic RCS at both low and high frequencies. Moreover, the results of HFSS were close to the results of Discretization Solution for both single and multilayer cylinders at low and high frequencies. On the other hand, similar results were observed between HFSS and Discretization Solution only for single layered arbitrary shapes. For multilayered arbitrary shaped objects, it was not obtained compatible results between HFSS and Discretization Solution. The first reason is the permittivity. Lossy dielectric materials were used for RCS calculations. When the permittivity of material is increased, the result of Discretization Solution deviated from the results of HFSS. Another reason was thickness. Discretization Solution gave compatible results with the results of HFSS when the thickness was very thin.

The advantage of using Discretization Solution is that it takes less calculation time than HFSS. For instance, the annual CPU time for Discretization solution is four minutes, however, the annual CPU time for HFSS is more than one hour, even for more complex shapes, or at high frequencies, this CPU time becomes a couple of hours. In addition, minimum 2 GB of RAM is necessary for HFSS simulations. In contrast, the same simulations with appropriate conditions can be run with Discretization solution with a basic PC.

REFERENCES

1. Nicolaescu, I. and T. Oroian, "Radar Cross Section", *IEEE CNF TELSIKS 2001, 5th International Conference*, vol.1, pp.65-68, 2001.

2. Ufimtsev, P.Y., "Comment on diffraction principles and limitations of RCS reduction techniques", *Proc. IEEE*, vol.84, no.12, pp.1830-1851, December 1996.

3. Knott, E.F. and J.F. Shaeffer, M.T. Tuley, *Radar Cross Section*, Artech House: Boston-London, 1993.

4. Mahafza, B.R., A.Z. Elsherbeni, *MATLAB Simulations for Radar Systems Design*, Chapman&Hall/CRC , Florida, 2004.

5. Knott, E.F., *Radar Cross Section Measurements*, Van Nostrand Reinhold, New York, 1993.

6. Jenn, D.C., *Radar and Laser Cross Section Engineering*, AIAA Education Series, Washington, 1995.

7. Ruck, G. T., D.E. Barrick, W.D. Sturat and C.K. Kirchbaum, *Radar Cross Section Handbook*, Vol.1-2, New York: Plenum, 1970.

8. Ishimaru A., "Wave Propagation and Scattering in Random Media", Vol.1, Academic Press, 1978.

9. Harre I., *RCS in Radar Range Calculations for Maritime Targets*, http:// www.mar-it.de/Radar/RCS/RCS_xx.pdf.

10. Ross R. A., "Radar Cross Section of Rectangular Flat Plates as a Function of Aspect Angle", *IEEE Transactions on Antennas and Propagation*, Vol. Ap-14, No.8, May, 1966.

11. Balanis C.A., *Advanced Engineering Electromagnetic*, John Wiley & Sons, Inc., New York, 1989.

12. Le Vine D., A. Schneider, H.R. Lang and G.H. Carter, "Scattering from Thin Dielectric Disks", *IEEE Transactions on Antennas and Propagation,* Vol. AP-33, No.12, December 1985.

13. Sarabandi K. and F.T. Ulaby, "Millimeter wave scattering model for a leaf", *Radio Science*, Vol. 25, No.1, pp. 9-18, January-February, 1990.

14. Küstür S., *Radar Cross Section of Arbitrary Shaped Multilayered Objects*, M.S. Thesis, Boğaziçi University, 2006.

15. Paris D.T. and F.K. Hurd, *Basic Electromagnetic Theory*, McGraw-Hill Book Company, Ch.7-8, 1969.

16. Bussey H.E. and J.H. Richmond, "Scattering by a Lossy Dielectric Circular Cylindrical Multilayer, Numerical Values", *IEEE AP-23*, no. 9, pp.723-725, 1975.

17. Tang C.C.H., "Backscattering from Dielectric-coated Infinite Cylindrical Obstacles", *J. Appl. Phys.*, vol.28, pp.628-633, May 1957.

18. Richmond J.H., "Efficient Recursive Solutions for Plane and Cylindrical Multilayers", *The Antenna Laboratory*, Ohaio State Univ., Columbus, Rep. 1968-1, 1965.

19. HFSS Online Help, *Ansoft HFSS,* Version 10.0.

20. Wei X.C., Li E.P., and Zhang Y.J. “Application of the Improved Finite Element-Fast Multipole Method to Large Scattering Problems”, *Progress In Electromagnetics Research,* PIER 47,49-60, 2004.

21. Seker S., Apaydın G., “Electromagnetic Scattering Properties of Thin Curved Dielectric Surface and Cylinder”.